Microstructurele aspecten van het corrosiegedrag van zuiver koper

Microstructural Characteristics of the Corrosion Behavior of Pure Copper

Linsey Lapeire

Promotoren: prof. dr. ir. L. Kestens, prof. dr. ir. K. Verbeken
Proefschrift ingediend tot het behalen van de graad van
Doctor in de Ingenieurswetenschappen: Materiaalkunde

Vakgroep Toegepaste Materiaalwetenschappen
Voorzitter: prof. dr. ir. J. Degrieck
Faculteit Ingenieurswetenschappen en Architectuur
Academiejaar 2014 - 2015

UNIVERSITEIT
GENT

ISBN 978-90-8578-800-3
NUR 971
Wettelijk depot: D/2015/10.500/44

Dankwoord

Hoewel sommige mensen nog altijd het idee hebben dat een doctorandus een eenzame onderzoeker is in een ivoren toren, is niets minder waar. Eenzaam is wel het laatste woord dat bij me opkomt wanneer ik terugdenk aan de bijna zes jaar die ik heb doorgebracht op het Technologiepark in Zwijnaarde. Ik heb tijdens mijn doctoraat de kans gekregen om heel wat schitterende mensen te ontmoeten en met hen samen te werken. Graag zou ik hen nu bedanken, niet enkel vanwege hun wetenschappelijke bijdrage, maar vooral omdat ze zijn blijven geloven in mij ondanks alle ups en downs die mezelf en mijn doctoraat gekenmerkt hebben.

Allereerst wil ik mijn twee promotoren, prof. Kestens en prof. Verbeken, in de bloemetjes zetten. Leo en Kim, zonder jullie was er geen sprake van dit doctoraat. Jullie hebben mij de kans gegeven uit mijn chemische comfortzone te treden en de wereld van de materialen te ontdekken. Gedurende mijn hele doctoraat bleven jullie mij met raad en daad bijstaan, ook op momenten dat ik het het minst verwachtte, maar toch het meest nodig had. Het vertrouwen dat jullie in mij hadden heeft enorm veel voor mij betekend.

Ook zou ik graag prof. Joris Degrieck bedanken, vakgroepvoorzitter van de vakgroep Toegepaste Materiaalwetenschappen, om mij de kans te geven in zijn vakgroep aan de slag te gaan. Bedankt ook aan alle proffen van de vakgroep Toegepaste Materiaalwetenschappen voor de goeie samenwerking de afgelopen jaren.

I wish to express my gratitude to all the members of the jury for reading this manuscript and for the fruitful discussions.

Esther Martinez Lombardia, or should I say Dr. Esther Martinez Lombardia, my partner in crime during my PhD. Esther, it was great not to work alone during this Phd, it was even better to have a partner to share thoughts and ideas with during this PhD, but the best of all, I had the opportunity to work with you! Thank you for all the discussions we had about how to handle our precious copper samples and how to interpret our (sometimes strange) experimental results. There is however a possibility I forget all these discussions. What I will never forget is what a wonderful person you are! Te deseo todo lo mejor. Bij deze ook bedankt aan prof. Herman Terryn en prof. Iris De Graeve voor alle steun en advies vanuit het VUB front.

Mijn eerste dag in de ‘assistentenzaal’ zal ik nooit vergeten. Stephanie en Sarah maakten me wegwijs in het gebouw, stelden me voor aan iedereen en ik ontdekte al heel snel dat ik het naar mijn zin zou hebben de komende jaren. Bij deze, bedankt Stephanie en Sarah, niet enkel voor de warme welkom de eerste dag, maar voor de vele toffe momenten die erop volgden, zowel op als buiten het werk. Iwein, spijtig genoeg was je maar een klein jaar mijn bureaumaatje, ik

begon net je enorm droge gevoel voor humor te snappen. Diana, Nuria, Edgar, Fernando, Ivonne, Katelijne, Jan, Aleksandar, Jurij, and Victor, you all were there the first day I arrived at the department and I saw all of you leaving for a new adventure. Thank you for being such good colleagues. I wish you all the best. A special thank you to Jurij. Jurij, you were always there for me when I was lost in texture world. Thank you for all the time, good advice and of course modeling work you put into the cryogenic paper. Koen, ook jou leerde ik kennen op mijn eerste werkdag. Bedankt voor de vele leuke en af en toe absurde momenten! Op congres gaan zonder jou is toch niet hetzelfde. En wees gerust, dat etentje ben ik nog niet vergeten!

Ik heb echter niet enkel mensen zien vertrekken uit de vakgroep, er kwamen ook heel wat nieuwe collega's bij, waarvan er sommigen echt vrienden werden. Sepideh, Tuan, Filipe, Soroosh and Elisabete thank you for being such nice colleagues. Evelien en Athina zonder jullie was het absoluut niet hetzelfde geweest. Bedankt voor de vele babbels, de zalige lunchmomenten, de nieuwste beauty tips, kledingadvies (of zelfs gewoon een nieuwe garderobe ☺). Inge, altijd klaar om iedereen met raad en daad bij te staan. Onze leuke babbels hebben mij deugd gedaan. Tom, chapeau, je weet je goed staande te houden tussen al het vrouwelijke geweld. We hebben misschien niet het meest diepgaande contact of de innigste gesprekken, maar sommige momenten zal ik toch niet snel vergeten. An, doordat jouw bureau op het einde van de gang ligt, kwam ik af en toe mijn hart bij jou luchten voor ik naar huis vertrok, bedankt voor het luisterende oor. En natuurlijk ook bedankt voor de vele leuke momenten in en buiten het departement. Emilie, onze nieuwste aanwinst, heel veel succes de komende jaren! Prijs jezelf gelukkig, je bent in een ongelooflijke groep terecht gekomen!!

Dorien, Hadi and Joachim, we were writing and will defend our thesis at almost the same time. Thank you for answering all my questions regarding layout or how to send a polite email to the jury members! Good luck with your defenses and of course with all the rest that comes along.

Dennis, Peter, Alex, Marnix, Christa en Vitaliy! Jullie waren onmisbaar voor het aan de praat krijgen en houden van alle mogelijke toestellen, het versnijden van mijn samples en alle andere technische dingen die ik op mijn eentje niet geregeld kreeg. Bedankt Roger om mijn computerproblemen (en dan vooral printproblemen) op te lossen. En dan nog een heel erg belangrijk iemand, Ilse, ik vond het altijd leuk om langs te komen op je bureau. Niet alleen omdat je altijd direct een antwoord had op al mijn vragen, maar ook voor de gezellige babbel. Bedankt om alle praktische zaken te regelen die samenhangen met een doctoraat!

En dan... ons bureau!! Ongetwijfeld het luidruchtigste bureau van heel de gang, altijd in voor een praatje met de toevallige voorbijganger! (sorry Klaas dat je af en toe je deur moest dicht doen om aan ons gelach te onsnappen). Onze vierde 'man' is af en toe gewisseld, maar de harde kern is toch zo'n 4 jaar ongewijzigd gebleven. Elien, je was al een ongelooflijk goeie vriendin na de eerste week aan de grote boze universiteit en ik was in de wolken toen je ook mijn collega

werd! Ik was nog blijer toen bleek dat ik ook een bureau met jou mocht delen. Ik kan zonder te liegen of te overdrijven zeggen dat jij de warmste en liefste persoon bent die ik ken. Ik ben zo blij dat ik je vriendin mag zijn. Babs, mysterieuze Babs, je zou denken dat ik je door en door zou moeten kennen na bijna vier jaar een bureau met jou gedeeld te hebben, maar niets is minder waar. Toch heb ik het gevoel dat ik altijd bij je terecht kan, bedankt daarvoor. Elien en Babs, ik ben me ervan bewust dat ik het jullie niet altijd even makkelijk heb gemaakt, maar bedankt om altijd naar me te blijven luisteren en me te blijven steunen. Bedankt voor alles!! Roberto, the one and only man in our office. Always cold, but a heart of gold ☺. Lisa, je hebt een korte, maar memorabele, tussenstop gemaakt in onze bureau. Je enorme drive blijft een inspiratiebron. En dan, Aurélie! Je moest gewoon in onze bureau terechtkomen, we hadden eindelijk ons ontbrekende puzzelstukje gevonden ☺. Vanaf dag 1 leek het alsof ik je al jaren kende. Ik bewonder je ongelooflijk en ben zo blij dat ik je heb leren kennen. Ongelooflijk veel succes in alles wat je doet, je verdient het! En dan, maar vier plaatsen op ons bureau, maar toch is er nog iemand onlosmakelijk mee verbonden, Line! Voor heel veel mensen de onmisbare secretaresse die voor iedereen klaarstaat, voor mij nog veel meer dan dat. Line, jouw aanwezigheid op de vakgroep was een wereld van verschil voor mij! We hebben samen heel wat afgelachen, gezeverd en geklaagd. (Nog eens sorry voor je botten!) Maar ik ga nooit vergeten wat je voor mij hebt betekend op momenten dat ik het heel moeilijk had. En niet te vergeten, door jouw weetjes en tips betreffende het moederschap ben ik ongetwijfeld een betere (of toch in elk geval een beter geïnformeerde) mama geworden! Arigato (of domo?)!! Er is gelachen en geweend geweest in onze bureau, als de muren konden praten...

Ondanks alle steun van iedereen in de vakgroep, dit doctoraat zou er niet geweest zijn zonder de steun van mijn familie en enkele wel heel bijzondere vriendinnen. Shan en Fien, bedankt om al zo lang mijn vriendin te willen zijn. Bedankt voor het luisterende oor, de toffe reisjes (als we ons vliegtuig niet missen natuurlijk), de gezellige zondagochtenden en gewoon om er op elk mogelijk moment te zijn. We hebben, denk ik, elk ons deel tegenslag wel gehad, maar hé, zie waar we staan! Al onze dromen die we hadden als tiener over ons perfecte leven zijn misschien (nog) niet uitgekomen, maar we zijn absoluut op de goeie weg! Onze drie aanpalende kamers in het rusthuis zijn in elk geval al gereserveerd ☺.

Mama en papa, ik weet dat ik jullie met mij heel wat hebben meegemaakt de laatste jaren. Hoewel Tristan vroeger verantwoordelijk was voor jullie (figuurlijk natuurlijk ☺) eerste grijze haren, heb ik toch voor wat extra exemplaren gezorgd tijdens mijn doctoraat. Dank je wel voor alles wat jullie voor mij gedaan hebben. Ik bewonder jullie enorm en ik kan me geen betere ouders en moetje en pepe wensen!! Oma en pepe (ondertussen beter gekend als oma oma en pietje) jullie betekenen zo veel voor mij! Godi en Vincent jullie zijn heel erg belangrijk geworden voor mij, bedankt voor alle steun tijdens de laatste jaren. Tristan, mijn kleine broertje, tijdens mijn doctoraat toch opeens een beetje volwassen geworden. En dan natuurlijk bedankt aan alle

Dankwoord

Lapeirtjes, Gammetjes, Marécauxtjes en Devosjes! Zonder de steun van jullie allen was het allemaal niet gelukt.

En dan de twee laatsten, maar absoluut de allerbelangrijksten!! Filip en Flo, mijn twee grootste schatten, mijn gezinnetje! Filip, bedankt om altijd zo positief te blijven! Met al mijn gezaag, geklaag en zenuwachtig gedoe die vooraf ging aan dit doctoraat heb ik je het zeker niet gemakkelijk gemaakt. Bedankt om er altijd, maar dan ook altijd voor mij te zijn! We hebben heel wat goede dagen gehad de laatste jaren, maar bedankt om me ook in de kwade dagen te blijven steunen. Ik kan me geen betere levenspartner dan jij voorstellen. Flo, je was er nog niet in het begin van mijn doctoraat, maar daar is snel verandering in gekomen. Door jou leerde ik alles weer in perspectief te plaatsen. Jouw schaterlach geeft me vleugels! De laatste jaren was het werken aan mijn doctoraat heel belangrijk, maar jullie zijn voor mij het allerbelangrijkste in mijn leven!

The Agency for Innovation by Science and Technology in Flanders (IWT) and the fund for Scientific Research in Flanders (FWO) are acknowledged for financial support (FWO10/PRJ/336). Aurubis (Belgium) is acknowledged for the ETP-Cu.

Bedankt allemaal!

Linsey

Summary

In our society, metals are used in a wide variety of applications, ranging from large building constructions and aerospace applications, to very small units in electronic devices. The choice for a specific metal or alloy can often be related to its mechanical properties, whereas in other cases, functional properties determine which metal is best suited. Regardless of the application, these metals always have one common feature, namely that their durability is affected by their interaction with the environment in which they are used. Often, this interaction has indeed a detrimental influence on the mechanical, physical and esthetical properties, as such decreasing the life span of the material. The degradation of the material properties, due to the fact that it is electrochemically active in contact with an aqueous environment, is often quoted as corrosion. Corrosion not only has a technological meaning as it indeed decreases the life span of metals; it also has important economic consequences, related to the need of having to replace metals or loss of production during maintenance, and might even be responsible for accidents, sometimes even with fatal outcome. In the pursuit of increasing the sustainable use of metals, a thorough knowledge of their electrochemical behavior is crucial.

In current literature, corrosion is often considered to be a purely chemical interaction with nearly exclusive dependence on compositional effects, whilst ignoring the microstructural and crystallographic properties of the metal surface. Recent literature, however, suggest an important correlation between the electrochemical activity of metals and alloys and microstructural features such as the grain orientation, the grain size and the grain boundary character. All these studies demonstrate that the local, microscopic features influence the electrochemical behavior, but a thorough understanding of the local corrosion phenomena is still lacking.

The aim of this doctoral thesis is to get more insight in the relation between the electrochemical behavior of a polycrystalline metal and its microstructural features. Not only the role of the grain boundaries is investigated, but also the role of the grain orientation is taken into account. For this, a systematic approach is needed. This consists, on the one hand, of a controlled variation and thorough characterization of the microstructure of a carefully selected metal and, on the other hand, meticulous quantification of the resulting electrochemical behavior. In literature, studies related to this topic are often focused on metals such as stainless steel, aluminum and titanium which are covered by a native oxide film. This film implies one studies rather the behavior of the oxide than the behavior of the material itself. To circumvent this problem, in this work, high-purity copper will be used as the model system.

At first, a controlled variation and quantification of the copper microstructure is performed. Microstructural features such as grain orientation and grain boundaries are controlled via

thermomechanical processing (TMP). Different TMP routes and the resulting microstructures are described in this doctoral thesis including the standard TMP routes including hot rolling, room temperature (RT) rolling and subsequent recrystallization annealing. Also the unconventional cryogenic rolling technique is discussed in detail. As the latter technique is less documented in literature a detailed analysis of the microstructural and texture evolution of these materials is made and was compared to the conventionally processed material. It is found that the RT rolled copper produces a pure metal texture whereas the cryogenically rolled copper exhibits a Brass type texture. In the cryogenically rolled material, deformation twins and shear bands are observed, as opposed to the RT rolled material. The cube component is observed in both RT and cryogenic rolled copper as part of the deformation texture. After annealing, the RT rolled material gives rise to a strong cube texture, in contrast to the cryogenically rolled copper, which exhibits a very weak texture. This weak texture can be attributed to the presence of shear bands in the cryogenically rolled material. The recrystallization texture inside the shear bands is experimentally determined and is in good agreement with the modeled deformed shear band texture. The cryogenic rolling also has a refining effect on the grain size, although the nanocrystalline range is not reached in the present experiment.

The resulting variations in microstructure and crystallographic texture are needed, not only to make it possible to study the effects of these variations on the electrochemical behavior, but also because each electrochemical technique has certain specific requirements depending for example on the size of the surface area under investigation. Consequently, different properties, such as grain size, but also other properties such as the presence of specific types of grain boundaries have to be adapted accordingly. All this can be done by making use of the most suitable thermomechanical processing steps.

Secondly, the resulting electrochemical behavior of copper is studied in order to better understand how the different grain orientations and grain boundary orientations will affect the electrochemical behavior. The relationship between the grain orientation and the electrochemical activity is studied with atomic force microscopy (AFM), the in-house developed gold-nanoplating technique, a technique which is described below, and with in-situ scanning electrochemical microscopy (SECM). To reveal the relationship between the grain boundaries and the electrochemical activity electrochemical scanning tunneling microscopy (EC-STM) combined with the gold-nanoplating technique is used.

The AFM, SECM and gold-nanoplating results suggest for the first time that the electrochemical activity of a grain not only depends on its specific crystallographic orientation, but is also affected by the orientation of its neighboring grains. Below we discuss briefly the results that are obtained with the different techniques.

With AFM in combination with EBSD the dissolution behavior of the polycrystalline copper is linked with some specific crystallographic orientations. The largest dissolution gradient, evaluated by surface elevation differences, is observed between adjacent grains with near <001>// ND and near <111>// ND orientations, respectively. No significant height differences are observed between adjacent grains of different other orientations, nor when the <001>// ND and <111>// ND grains are separately evaluated.

The grain dependent electrochemical activity of copper is also investigated by means of gold-nanoplating. This in-house developed technique is based on the electrochemical displacement of gold, where the gold is deposited from an aqueous solution, onto the copper surface. After gold deposition, the complementary use of EBSD and FE-SEM was particularly well suited to detect differences in the electrochemical activity of the differently oriented grains during the Au-Cu redox process occurring at the Cu surface. The focus is on three low-indexed orientations, namely <001>// ND, <110>// ND and <111>// ND. The results suggests that <111>// ND and <100>// ND oriented grains have a higher electrochemical activity compared to the <110>// ND grains. However, a large variation in the electrochemical activity is observed between similarly oriented grains. Consistent with the results obtained with AFM, also with the gold-nanoplating technique, deviating electrochemical behavior is observed when <111>// ND oriented grains are adjacent to <100>// ND grains. This could explain the large variations in electrochemical activity between similarly oriented grains, as the orientation of the neighboring grains are observed to play a decisive role in the electrochemical behavior of that specific grain.

Finally, the grain dependent electrochemical activity of pure copper in the active state is investigated by means of a local electrochemical technique, namely in-situ SECM. It is found that for copper in the active state the highest current is observed for the <111>// ND orientation. It is also concluded that the <100>// ND oriented grain is less active when located between <111>// ND oriented grains. Also with SECM it is shown that besides the grain orientation, the orientation relations between the neighboring grains play a decisive role in the corrosion kinetics of polycrystalline copper.

To visualize differences in energy and corrosion behavior for the different types of grain boundaries in polycrystalline copper two different techniques are used in this doctoral thesis.

With the gold-nanoplating technique it becomes possible to separate the so-called special or CSL (coincident site lattice)-type boundaries from random boundaries in an efficient way. Using energy dispersive X-ray spectroscopy (EDX) differences in the amount of deposited gold can be quantified. It is shown that the coherent twin boundaries have an extremely low amount of deposited gold and, as a consequence, these grain boundaries should be very resistant to corrosion. The observed results for the quantified gold deposition of various types of grain boundaries in polycrystalline copper are consistent with both calculated as experimental

literature predictions on grain boundary energies. Since the difference in gold concentration seems to be related to the grain boundary energy, gold-nanoplating offers an experimental confirmation of the differences in grain boundary energy that are considered to be present in a polycrystalline material in a statistical manner as this technique allows measuring significant amounts of grain boundaries.

Secondly, for the first time to our knowledge EC-STM is used to study the corrosion behavior of a polycrystalline metal. With the combined use of EBSD and EC-STM, it is possible to link grain boundary type with susceptibility to intergranular corrosion in microcrystalline copper. The data provide direct evidence that the coherent twin grain boundaries are resistant to corrosion, these results nicely complement the experimental results found with the gold-nanoplating technique.

Samenvatting

In onze maatschappij worden metalen gebruikt in een breed gamma aan toepassingen, variërend van grote constructies in de bouw en de ruimtevaart tot zeer kleine componenten in elektronische apparaten. De toepassing van een bepaald metaal of legering wordt vaak bepaald door de mechanische of functionele eigenschappen van dit metaal. Alle metalen hebben echter één gemeenschappelijk kenmerk, namelijk dat hun levensduur beïnvloed wordt door hun interactie met de omgeving. Vaak heeft deze interactie immers een negatieve invloed op de mechanische, fysische en/of esthetische eigenschappen van het metaal. De degradatie van de materiaaleigenschappen, vanwege het feit dat het metaal elektrochemisch actief is in contact met een waterig milieu, wordt vaak gecatalogeerd onder de brede noemer van corrosie. Corrosie heeft niet alleen een technologische betekenis, het leidt ook tot belangrijke economische verliezen door de noodzaak tot het vervangen van metalen in bijvoorbeeld industriële installaties en stilstand bij onderhoud. Verschillende ongevallen, soms zelfs met dodelijke afloop, zijn reeds het gevolg geweest van het optreden van corrosiefenomenen. In het streven naar het verhogen van de duurzaamheid van metalen en het verlengen van de levensduur van een metaal is een grondige kennis van corrosie en dus van het elektrochemische gedrag van een metaal in een specifieke omgeving cruciaal.

In de huidige literatuur wordt corrosie vaak beschouwd als een interactie met bijna exclusieve afhankelijkheid van samenstellingseffecten, terwijl de microstructurele en kristallografische eigenschappen van het metaaloppervlak buiten beschouwing worden gelaten. Recente literatuur suggereert echter een belangrijke correlatie tussen de lokale elektrochemische activiteit van metalen en microstructurele kenmerken zoals de korreloriëntatie, de korrelgrootte en de korrelgrenzen en hun karakteristieken. Al deze studies tonen aan dat deze lokale microscopische kenmerken het elektrochemische gedrag beïnvloeden, maar evenzeer dat de kennis voorhanden momenteel nog ontoereikend is.

Het doel van dit proefschrift is om meer inzicht te verwerven in de relatie tussen het elektrochemisch gedrag van een polykristallijn metaal en de microstructuur ervan. Niet alleen de rol van de korrelgrenzen wordt onderzocht, maar ook de rol van de korreloriëntatie in het corrosieproces wordt uitvoerig belicht. Hiervoor is een systematische aanpak nodig. Deze bestaat enerzijds uit een gecontroleerde variatie en grondige karakterisering van de microstructuur van een zorgvuldig geselecteerd metaal en anderzijds uit een gedetailleerde kwantificering van het resulterend elektrochemisch gedrag. De bestaande publicaties omtrent dit onderwerp hebben meestal echter betrekking op metalen zoals roestvast staal, aluminium en titanium waarvan het elektrochemische gedrag grotendeels gedomineerd wordt door de natuurlijk gevormde oppervlakte-oxidelaag hetgeen de interpretatie en de koppeling met de

onderliggende metaalmicrostructuur heel wat complexer maakt. Om dit te vermijden is in dit werk gekozen om met hoogzuiver koper te werken.

Allereerst wordt een gecontroleerde variatie van de microstructurele aspecten van het koper samen met een kwantificatie van de resulterende microstructuur uitgevoerd. Microstructurele eigenschappen zoals korreloriëntatie en korrelgrensoriëntatie worden aangestuurd via thermomechanische processing (TMP). Verschillende TMP routes en de daaruitvolgende microstructuren worden beschreven in dit proefschrift waaronder de standaard TMP routes zoals warmwalsen en walsen op kamertemperatuur gecombineerd met een rekristalliserend gloeiproces. Ook de eerder onconventionele techniek van het cryogeen walsen wordt toegepast en in detail geanalyseerd. Het is gebleken dat het kamertemperatuur gewalste koper de verwachte textuur produceert, terwijl het cryogeen gewalste koper een Brass textuur vertoont. In het cryogeen gewalste materiaal, zijn vervormingstweelingen en shear bands of afschuifbanden waargenomen, dit in tegenstelling tot het op kamertemperatuur gewalste koper. De kubische component wordt zowel waargenomen in het op kamertemperatuur als in het cryogeen gewalste koper als deel van de vervormingstextuur. Na gloeien ontstaat in het materiaal op kamertemperatuur gewalst een sterke kubische textuur, dit in tegenstelling tot het cryogeen gewalst metaal, dat een zeer zwakke textuur vertoont. Deze zwakke textuur kan worden toegeschreven aan de aanwezigheid van de hierboven aangehaalde shear bands in de microstructuur van het cryogeen gewalste koper. De rekristallisatietextuur in de shear bands wordt experimenteel geanalyseerd en blijkt in goede overeenstemming te zijn met de gemodelleerde vervormde shear band textuur. Het cryogene walsen is ook verantwoordelijk voor het vormen van kleinere korrels na rekristallisatie.

De resulterende variaties in microstructuur en kristallografische textuur zijn nodig, niet alleen om toe te laten de effecten van deze variaties op het elektrochemisch gedrag te bestuderen, maar ook omdat elke elektrochemische techniek bepaalde specifieke vereisten hieromtrent stelt. Immers, lokale elektrochemische technieken analyseren afhankelijk van hun resolutie en andere specifieke eigenschappen een bepaald oppervlakte van het sample. Bijgevolg moeten de verschillende eigenschappen zoals korrelgrootte, maar ook andere eigenschappen zoals de aanwezigheid van bijvoorbeeld specifieke types korrelgrenzen hierop aangepast worden. Dit alles kan gebeuren door gebruik te maken van de meest geschikte manier van thermomechanisch processen.

Vervolgens wordt het resulterende elektrochemisch gedrag van de verschillende microstructuren bestudeerd zodat een beter begrip ontstaat over hoe de verschillende korreloriëntaties en korrelgrensoriëntaties het elektrochemische gedrag kunnen beïnvloeden. De relatie tussen de korreloriëntatie en de elektrochemische activiteit wordt bestudeerd met atomic force microscopie (AFM), met de zelf ontwikkelde goud-nanoplating techniek, die

hieronder kort wordt toegelicht, en met in-situ electrochemical scanning microscoop (SECM). Om de relatie tussen de korrelgrensoriëntatie en de elektrochemische activiteit in beeld te brengen wordt gebruik gemaakt van scanning tunneling microscopie (EC-STM) en wordt deze opnieuw gecombineerd met de goud-nanoplating techniek.

De AFM, SECM en goud-nanoplating resultaten toonden voor het eerst duidelijk aan dat de elektrochemische activiteit van een korrel niet alleen afhankelijk is van de specifieke kristallografische oriëntatie van de korrel zelf, maar dat ook van de oriëntatie van de naburige korrels een cruciale rol speelt hierin. Hieronder wordt kort ingegaan op de resultaten die met de verschillende technieken bekomen worden.

Met behulp van AFM in combinatie met EBSD wordt het corrosiegedrag van het polykristallijn koper gelinkt met een aantal specifieke kristallografische oriëntaties. Het verschil in aantasting van de verschillende oriëntaties wordt zichtbaar gemaakt door hoogteverschillen bij de AFM meting. De grootste corrosie gradiënt wordt waargenomen tussen aangrenzende korrels met een <001>// ND en een <111>// ND oriëntatie. Er worden geen significante hoogteverschillen geconstateerd tussen aangrenzende korrels met random oriëntaties, zelfs niet indien de <001>// ND en de <111>// ND korrels afzonderlijk aanwezig waren in de bestudeerde zone.

De relatie tussen de korreloriëntatie en de elektrochemische activiteit van koper wordt ook onderzocht door middel van goud-nanoplating. Deze zelf ontwikkelde techniek is gebaseerd op de elektrochemische reactie van goudkationen met het koperoppervlak. Na de goudafzetting is de combinatie van EBSD en veld emissie rasterelektronen microscopie (FE-SEM) bijzonder geschikt om de verschillen in de elektrochemische activiteit van de verschillend georiënteerde korrels tijdens de Au-Cu redoxreactie te detecteren. De focus ligt op drie oriëntaties, namelijk de <001>// ND, de <110>// ND en de <111>// ND oriëntatie. De resultaten suggereren dat de <111>// ND en <100>// ND georiënteerde korrels een grotere elektrochemische activiteit hebben vergeleken met de <110>// ND georiënteerde korrels. Er is echter een grote spreiding in de elektrochemische activiteit waargenomen voor vergelijkbaar georiënteerde korrels. Consistent met de resultaten verkregen met AFM wordt ook met de goud-nanoplating techniek afwijkende resultaten waargenomen bij <111>// ND georiënteerde korrels die grenzen aan <100>// ND georiënteerde korrels. Dit zou de grote variaties in elektrochemische activiteit kunnen verklaren tussen soortgelijke georiënteerde korrels. Bijgevolg blijkt dus opnieuw de oriëntatie van de naburige korrels een doorslaggevende rol te spelen bij het elektrochemische gedrag van een specifieke korreloriëntatie.

Als laatste wordt het korreloriëntatie afhankelijk elektrochemische activiteit van zuiver koper in actieve staat onderzocht door middel van een lokale elektrochemische techniek, namelijk in-situ SECM. Voor koper in een actieve toestand wordt de hoogste stroom waargenomen voor de <111>// ND oriëntatie. Er wordt ook vastgesteld dat de <100>// ND georiënteerde korrels

minder actief zijn wanneer zich tussen <111>// ND georiënteerde korrels bevinden. Ook SECM bevestigt bijgevolg dat, naast de korreloriëntatie, de oriëntatie van de naburige korrels een beslissende rol kan spelen in de elektrochemische activiteit van het polykristallijne koper.

Om de verschillen in energie en elektrochemische activiteit van de verschillende types korrelgrenzen in polykristallijn koper te visualizeren werden twee verschillende technieken aangewend in dit proefschrift.

Met de goud-nanoplating techniek wordt het mogelijk om de zogenaamde bijzondere of CSL (coincidence site lattice) type korrelgrenzen van random korrelgrenzen op een efficiënte manier te onderscheiden. Met behulp van energie dispersieve X-stralen spectroscopie (EDX) worden verschillen in de hoeveelheid afgezet goud gekwantificeerd. Op de coherente tweelingkorrelgrenzen wordt een extreem lage hoeveelheid goud afgezet, wat aantoont dat deze korrelgrenzen zeer corrosiebestendig zijn. De gevonden resultaten voor de gekwantificeerde hoeveelheid goudafzetting op de andere korrelgrenzen in het polykristallijne koper zijn gelijkaardig aan zowel berekende als experimentele literatuurvoorspellingen betreffende de korrelgrensenergieën. Aangezien het verschil in goudconcentratie gerelateerd lijkt te zijn aan de korrelgrensenergie, zorgt goud-nanoplating voor een experimentele bevestiging van de verschillen in korrelgrensenergie die in een polykristallijn materiaal geacht worden aanwezig te zijn.

Ook de EC-STM techniek wordt gebruikt om het corrosiegedrag van het koperoppervlak te bestuderen. Voor zover we weten is dit de eerste keer dat de EC-STM techniek wordt gebruikt voor het in beeld brengen van het corrosiegedrag van een polykristallijn materiaal. Door de combinatie van EBSD en EC-STM wordt het mogelijk de gevoeligheid aan intergranulare corrosie van verschillende types korrelgrenzen te visualiseren. De resulaten bevestigen dat de coherente tweeling korrelgrenzen bestand zijn tegen corrosie, wat volledig in lijn ligt met de experimentele resultaten van het goud-nanoplaten.

List of publications

Publications in international peer-reviewed journals

1. L. Lapeire, J. Sidor, P. Verleysen, K. Verbeken, I. De Graeve, H. Terryn, L. Kestens, Texture comparison between room temperature rolled and cryogenically rolled pure copper, Acta Materialia, *submitted*.

2. E. Martinez Lombardia, L. Lapeire, I. De Graeve, K. Verbeken, L. Kestens, H. Terryn, Study of the relation between macroelectrochemical behavior and the different microstructural parameters, *in preparation*.

3. L. Lapeire, E. Martinez Lombardia, K. Verbeken, I. De Graeve, H. Terryn, L.A.I. Kestens, Grain orientation dependent gold deposition by nanoplating of polycrystalline copper, *In preparation*.

4. H. Chen, V. Maurice, L. Klein, L. Lapeire, K. Verbeken, H. Terryn, P. Marcus, Grain boundary passivation studied by in situ scanning tunneling microscopy on microcrystalline copper, Journal of Solid State Electrochemistry (2015) 1-9 .

5. E. Martinez Lombardia, V. Maurice, L. Lapeire, I. De Graeve, K. Verbeken, L. Kestens, P. Marcus, H. Terryn, In Situ Scanning Tunneling Microscopy Study of Grain-Dependent Corrosion on Microcrystalline Copper, The Journal of Physical Chemistry C 118 (2014) 25421-25428.

6. L. Lapeire, E. Martinez Lombardia, K. Verbeken, I. De Graeve, H. Terryn, L.A.I. Kestens, Structural dependence of gold deposition by nanoplating in polycrystalline copper, Journal of Materials Science 49 (2014) 3909-3916.

7. E. Martinez Lombardia, L. Lapeire, V. Maurice, I. De Graeve, K. Verbeken, L.H. Klein, L.A.I. Kestens, P. Marcus, H. Terryn, In situ scanning tunneling microscopy study of the intergranular corrosion of copper, Electrochemistry Communications 41 (2014) 1-4.

8. E. Martinez Lombardia, Y. Gonzalez-Garcia, L. Lapeire, I. De Graeve, K. Verbeken, L. Kestens, J.M.C. Mol, H. Terryn, Scanning electrochemical microscopy to study the effect of crystallographic orientation on the electrochemical activity of pure copper, Electrochimica Acta 116 (2014) 89-96.

9. L. Lapeire, E. Martinez Lombardia, K. Verbeken, I. De Graeve, L.A.I. Kestens, H. Terryn, Effect of neighboring grains on the microscopic corrosion behavior of a grain in polycrystalline copper, Corrosion Science 67 (2013) 179-183.

10. R. Gaggiano, E. Martinez Lombardia, I. De Graeve, L. Lapeire, K. Verbeken, L.A.I. Kestens, H. Terryn, Gold nanoplating as a new method for the quantification of the electrochemical activity of grain boundaries in polycrystalline metals, Electrochemistry Communications 24 (2012) 97-99.

11. E. De Canck, L. Lapeire, J. De Clercq, F. Verpoort, P. Van Der Voort, New Ultrastable Mesoporous Adsorbent for the Removal of Mercury Ions, Langmuir 26 (2010) 10076-10083.

Publications in proceedings of international conferences

1. V. Maurice, H. Chen, L. H. Klein, L. Lapeire, K. Verbeken, H. Terryn, P. Marcus, Metal grain passivation studied by in situ scanning tunneling microscopy on microcrystalline copper, in: Eurocorr, Proceedings (2015*), submitted*.

2. L. Lapeire, J. Sidor, E. Martinez Lombardia, K. Verbeken, I. De Graeve, H. Terryn, L. Kestens, Texture comparison of cold rolled and cryogenically rolled pure copper, Materials science and engineering, 82 (2015) 012-016.

3. E. Martinez Lombardia, L. Lapeire, V. Maurice, I. De Graeve, L. H. Klein, P. Marcus, K. Verbeken, L; Kestens, Y. Gonzalez-Garcia, A. Mol, H. Terryn, Use of local electrochemical methods (SECM, EC-STM) and AFM to differentiate microstructural effects (EBSD) on very pure copper, in: 19th international corrosion congress, Proceedings (2014).

4. L. Lapeire, E. Martinez Lombardia, K. Verbeken, I. De Graeve, L. Kestens, H. Terryn, On the role of the crystallographic grain characteristics in the corrosion behavior of polycrystalline copper, in: Materials science forum, 783 (2013) 1158-1663.

5. L. Lapeire, E. Martinez Lombardia, K. Verbeken, I. De Graeve, L.A.I. Kestens, H. Terryn, Combined EBSD and AFM study of the corrosion behaviour of ETP-Cu. In: Materials science forum, 702 (2012) 673-676.

6. L. Lapeire, K. Verbeken, E. Martinez Lombardia, I. De Graeve, L.A.I. Kestens, H. Terryn, Copper: a model alloy to understand the role of microstructure in sustainability, in: European Metallurgical Conference, Proceedings (2011) 1631-1644.

7. I. De Baere, L. Lapeire, W. Van Paepegam, S. Daggumati, K. Verbeken, J. Degrieck, Macromechanical and microscopic study of the fatigue damage behaviour of carbon fabric/PPS thermoplastic composite, in: Sampe Europe Technical Conference, Proceedings (2011)

Presentations on international conferences

1. E. Martinez Lombardia, L. Lapeire, V. Maurice, L. Klein, I. De Graeve, H. Terryn, K. Verbeken, L. Kestens, P. Marcus, Y. Gonzalez-Garcia, A. Mol, H. Terryn (2014, November), Use of local electrochemical methods (SECM, STM) and AFM to differentiate microstructural effects (EBSD) on very pure copper. 19th international corrosion congress, Jeju Island, South Korea. (Oral presentation)

2. E. Martinez Lombardia, L. Lapeire, V. Maurice, L. Klein, I. De Graeve, H. Terryn, K. Verbeken, L. Kestens, P. Marcus, Y. Gonzalez-Garcia, A. Mol, H. Terryn (2014, September), Study of the relationship between microstructure and corrosion properties of polycrystalline copper. The European corrosion congress (EUROCORR 2014), Pisa, Italy. (Oral presentation).

3. L. Lapeire, J. Sidor, E. Martinez Lombardia, K. Verbeken, I. De Graeve, H. Terryn, L. Kestens (2014, August), Texture comparison of cold rolled and cryogenically rolled pure copper. International conference on textures of materials (ICOTOM-17), Dresden, Germany. (Oral presentation)

4. E. Martinez Lombardia, Y. Gonzalez-Garcia, L. Lapeire, I. De Graeve, K. Verbeken, L. Kestens, H. Terryn (2014, June), Localised study of the effect of crystallographic orientation on the electrochemical activity of pure copper. 19th Meeting of the Portuguese electrochemical society, University of Aveiro, Portugal. (Oral presentation)

5. L. Lapeire, E. Martinez Lombardia, K. Verbeken, I. De Graeve, L. Kestens, H. Terryn (2013, December), On the role of the crystallographic grain characteristics in the corrosion behaviour of polycrystalline copper. International conference on processing and manufacturing of advanced materials (THERMEC), Las Vegas, United States of America. (Oral presentation)

6. E. Martinez Lombardia, L. Lapeire, V. Maurice, L. Klein, I. De Graeve, H. Terryn, K. Verbeken, L. Kestens, P. Marcus, H. Terryn (2013, September). Study of the effect of crystallographic orienation on the electrochemical behavior of pure copper. The European corrosion congress (EUROCORR 2013), Lisbon, Portugal. (Oral presentation)

7. L. Lapeire, E. Martinez Lombardia, K. Verbeken, I. De Graeve, L. Kestens, H. Terryn (2013, June), Visualization of differences in the electrochemical grain boundary activity in polycrystalline copper by gold nanoplating, XIV International conference on Intergranular and Interphase Boundaries in Materials, Halkidiki, Greece. (Poster presentation)

8. E. Martinez Lombardia, L. Lapeire, Y. Gonzalez-Garcia, I. De Graeve, K. Verbeken, L. Kestens, H. Terryn (2013, February), Scanning Electrochemical Microscopy to study the effect of the crystallographic orientation on the electrochemical activity of pure copper. 7th Workshop on Scanning Electrochemical Microscopy (SECM-7), Ein Gedi, Israel. (Oral presentation).

9. E. Martinez Lombardia, L. Lapeire, I. De Graeve, H. Terryn, K. Verbeken, L. Kestens (2012, September). Study of the influence of the microstructure on the electrochemical activity of copper. The European corrosion congress (EUROCORR 2012), Istanbul, Turkey. (Oral presentation)

10. L. Lapeire, E. Martinez Lombardia, K. Verbeken, I. De Graeve, L. Kestens, H. Terryn (2011, December). Combined EBSD and AFM to study the corrosion behavior of ETP-Cu. International conference on textures of materials (ICOTOM-16), Mumbai, India. (Oral presentation).

11. L. Lapeire, E. Martinez Lombardia, K. Verbeken, L. Kestens, I. De Graeve, L. Kestens (2011, April).Combine EBSD and AFM to study the corrosion behavior of ETP-Cu. Texture and Anisotropy 2011, Ghent, Belgium. (Poster presentation).

Table of contents

List of symbols

$\sum n$	Coincidence site lattice boundary with 1/n common lattice points across the boundary
d	Spacing between crystallographic planes
D	Diffusion coefficient
e	Macroscopic strain
e_b	Fraction of strain in bulk
e_{SB}	Fraction of strain in shear band
F	Faraday's constant
h	Planck's constant
h_f	Final thickness
h_i	Initial thickness
i_{limit}	Diffusion-limited current
L	Contact length
m	Electron mass
n	Rotation axis
q	Charge density
R	Rolling cylinder radius
r	Radius of the microelectrode
t	Diffusion time
V_{SB}	Volume fraction of shear bands
γ	Shear strain
δ	Thickness of the diffusion layer
θ_a	Angle between the incident beam and the scattering plane

θ	Misorientation angle
λ	Wavelength of the incident beam
ϕ	Euler angle
ϕ_w	Work function
φ_1	Euler angle
φ_2	Euler angle

List of abbreviations

AFM	Atomic force microscopy
CI	Confidence index
CSL	Coincident site lattice
CV	Cyclic voltammogram
DOF	Degrees of freedom
DSC	Differential scanning calorimetry
EBSD	Electron backscatter diffraction
EBSP	Electron backscatter pattern
EC-STM	Electrochemical scanning tunneling microscopy
ETP	Electrolytic though pitch
FCC	Face centered cubic
FE-SEM	Field emission scanning electron microscope
GB	Grain boundary
GOS	Grain orientation spread
HAGB	High angle grain boundary
IPF	Inverse pole figure
IQ	Image quality
LAGB	Low angle grain boundary
ND	Normal direction (in a rolled product)
OCP	Open circuit potential
ODF	Orientation distribution function
OIM	Orientation imaging microscopy
RD	Rolling direction (in a rolled product)

RT	Room temperature
RX	Recrystallization
SB	Shear band
SECM	Scanning electrochemical microscopy
SEM	Scanning electron microscope
SFE	Stacking fault energy
SHE	Standard hydrogen electrode
SPM	Scanning probe microscopy
TD	Transverse direction (in a rolled product)
TMP	Thermomechanical processing
VPSC	Visco plastic self-consistent
XRD	X-Ray diffraction

Chapter 1
Introduction

1.1 Background

Metals are materials pre-eminently used for structural applications. Since the use of metals is extremely versatile, they are exposed to an enormous diversity of environments. Often, this interaction has a detrimental influence on the mechanical, physical and esthetical properties. The degradation of the material properties, due to the fact that the metal surface is electrochemically active in contact with an aqueous environment, is often quoted as corrosion. Corrosion not only has a technological meaning and decreases the life span of metals; it also has important economic consequences and might even be responsible for accidents, sometimes even with fatal outcome.

In the pursuit of increasing the sustainability of metals, a detailed knowledge of the electrochemical behavior is of crucial importance. The electrochemical behavior is the combined effect of two features: the electrochemical potential as a thermodynamic property and the current density of the electrochemical reaction as a kinetic property.

In current state-of-the-art literature corrosion is often considered as a macroscopic phenomenon, where the emphasis is rather on compositional effects, which implies that the possible effect of microstructural characteristics is often overlooked [1-5]. However, recent literature suggests an important correlation between the reactivity of metals and alloys and the grain orientation, the grain size and the grain boundaries [6-8]. These studies demonstrate that the local, microscopic features influence the electrochemical behavior, but a physically founded relationship is still lacking.

1.2 Objective and approach of the thesis

In analogy with mechanical engineering, where the bulk microstructural features of the metal are related to its mechanical properties, this dissertation aims to link the electrochemical behavior to the microstructural characteristics of the metal surface. The electrochemical behavior that is observed on the metal on a macroscopic scale is the convolution of the individual contributions of local electrochemical processes. Thus, in order to understand the general electrochemical behavior, it is mandatory to study the local electrochemistry.

Figure 1-1 introduces schematically the approach of this doctoral dissertation. Since microstructural features as grain orientation, grain size and grain boundary characteristics are

controlled via thermomechanical processing (TMP), a first step in this dissertation consists in designing microstructures by appropriately modifying the metal manufacturing process. This is done by hot rolling, room temperature (RT) rolling, cryogenic rolling and annealing.

With the help of both X-ray diffraction (XRD) and electron backscatter diffraction (EBSD) the microstructural characteristics of the metal will be evaluated. With these techniques information is obtained on the grain size, overall texture, specific grain orientation and grain boundary characteristics.

In addition to the microstructural characterization, atomic force microscopy (AFM), scanning electrochemical microscopy (SECM) and in situ electrochemical scanning tunneling microscopy (in situ EC-STM) will be used to evaluate the local electrochemical behavior of the metal in combination to an in-house developed technique called gold-nanoplating.

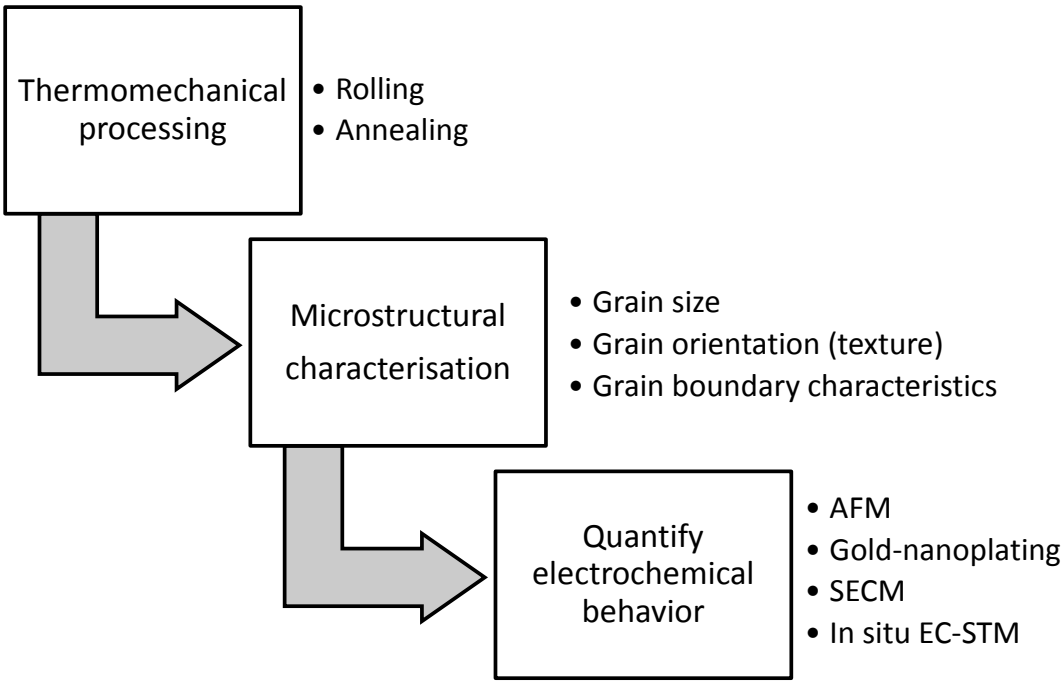

Figure 1-1: Approach of this doctoral dissertation.

1.3 Outline

Figure 1-2 presents the layout of this doctoral dissertation.

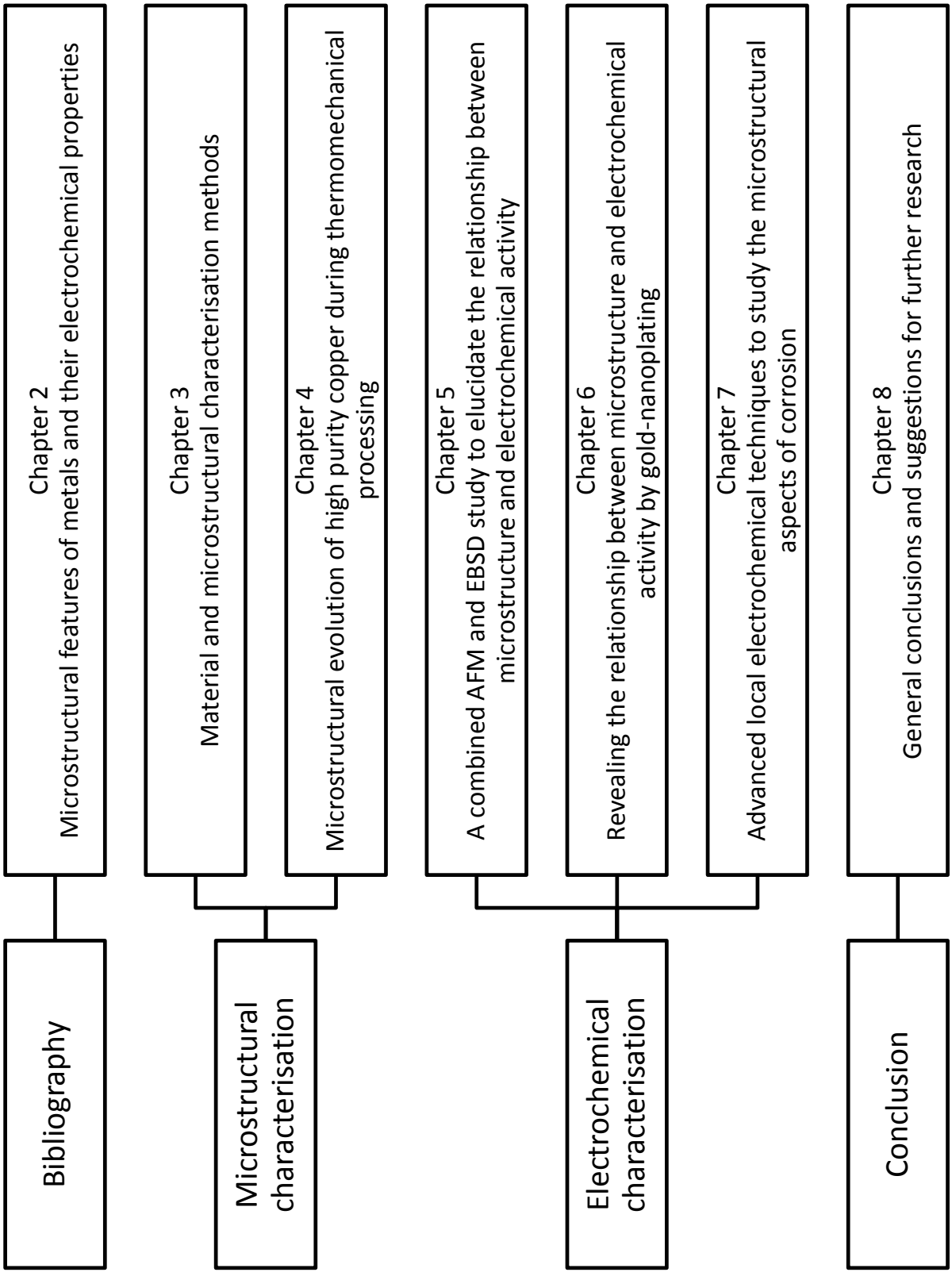

Figure 1-2: Layout of this doctoral dissertation.

The bibliography is covered in chapter 2, which discusses the results reported in the literature about the link between the microstructural features of metals and their electrochemical properties. All these studies demonstrate that the local, microscopic features affect the electrochemical behavior, but that a physically based comprehensive understanding of these phenomena is still lacking.

In chapter 3 the choice of high purity copper as a model system is motivated and the different techniques to obtain a full characterization of the microstructure are explained.

The different TMP routes and their influence on the microstructure are presented in chapter 4. Both the influence of hot rolling, RT rolling, cryogenic rolling and annealing on the microstructure of a high purity copper sample is discussed. These different, fully characterized materials are the starting point for the measurements presented in the subsequent chapters.

In chapters 5 to 7, the focus is on the quantitative study of the microscopic electrochemical behavior of pure copper, related to the microstructural features, through different techniques, both existing and newly developed.

The atomic force microscope (AFM) is used in chapter 5 to explore the relationship between the grain orientation and the corresponding electrochemical behavior. In an innovative approach, the influence of the orientation of neighboring grains on the corrosion behavior of a single grain is reported.

The newly developed gold-nanoplating technique is described in chapter 6. It appears that it is a technique that is able to visualize and quantify the electrochemical activity of grains and grain boundaries in polycrystalline copper. Regarding grain boundaries it is a technique that can separate random from so called special boundaries and the experimental results can be correlated with the grain boundary energy. When focusing on the crystallographic orientations, the results obtained in chapter 5 regarding the influence of neighboring grains on the electrochemical activity of a single grain are confirmed.

In chapter 7, two micro electrochemical techniques, namely scanning electrochemical microscopy (SECM) and in situ electrochemical scanning tunneling microscopy (in situ EC-STM) are used to determine locally the influence of both grains and grain boundaries on the electrochemical behavior. The experimental results described in the previous chapter are confirmed with these local electrochemical techniques.

The main conclusions of this doctoral dissertation are presented in chapter 8, together with a number of suggestions for future work.

Whereas the complete PhD was carried out in the frame of a common project between UGent and VUB, all results presented in chapter 4 were mainly the results obtained in my part of the collaboration. The results summarized in chapter 7 were mainly the work of dr. ir. Esther Martinez Lombardia, who recently defended her PhD at the VUB and was supervised by prof. dr. ir. Herman Terryn and prof. dr. ir. Iris De Graeve. My task in chapter 7 was to steer the microstructure in the best possible way to obtain microstructural features which were optimal for the local electrochemical techniques used. Dr. ir. Martinez Lombardia and I worked in close collaboration to perform and understand the observations presented in chapter 5. The gold-nanoplating technique (chapter 6) was first tried and developed by dr. ir. Esther Martinez Lombardia and dr. ir. Roberto Gaggiano. The further development and optimizing of the technique was done by myself.

1.4 References

1. Ghali, E., W. Dietzel and K.U. Kainer, General and localized corrosion of magnesium alloys: A critical review. Journal of Materials Engineering and Performance, 2004. 13(1): p. 7-23.

2. Alfantazi, A.M., T.M. Ahmed and D. Tromans, Corrosion behavior of copper alloys in chloride media. Materials & Design, 2009. 30(7): p. 2425-2430.

3. Andreatta, F., H. Terryn, M.M. Lohrengel and J.H.W. De Wit, Use of scanning Kelvin probe force microscopy and microcapillary cell to investigate local corrosion behaviour of 7xxx aluminium alloys. Local Probe Techniques for Corrosion Research, 2006: p. 126-136.

4. van den Bos, C., H.C. Schnitger, X. Zhang, A. Hovestad, H. Terryn and J.H.W. De Wit, Influence of alloying elements on the corrosion resistance of rolled zinc sheet. Corrosion Science, 2006. 48(6): p. 1483-1499.

5. Caicedo-Martinez, C.E., E.V. Koroleva, G.E. Thompson, P. Skeldon, K. Shimizu, G. Hoellrigl, C. Campbell and E. McAlpin, Influence of impurities in aluminium on surface treatment. Corrosion Science, 2002. 44(11): p. 2611-2620.

6. Davepon, B., J.W. Schultze, U. Konig and C. Rosenkranz, Crystallographic orientation of single grains of polycrystalline titanium and their influence on electrochemical processes. Surface & Coatings Technology, 2003. 169: p. 85-90.

7. Ralston, K.D. and N. Birbilis, Effect of Grain Size on Corrosion: A Review. Corrosion, 2010. 66(7).

8. Miyamoto, H., K. Yoshimura, T. Mimaki and M. Yamashita, Behavior of intergranular corrosion of < 011 > tilt grain boundaries of pure copper bicrystals. Corrosion Science, 2002. 44(8): p. 1835-1846.

9. Gaggiano, R., E. Martinez Lombardia, I. De Graeve, L. Lapeire, K. Verbeken, L.A.I. Kestens and H. Terryn, Gold nanoplating as a new method for the quantification of the electrochemical activity of grain boundaries in polycrystalline metals. Electrochemistry Communications, 2012. 24(0): p. 97-99.

Chapter 2
Microstructural features of metals and their electrochemical properties

2.1 Introduction

In this bibliographic chapter a short theoretical background will be given about the different microstructural features of a metal. In the first part, the answer will be given on the following questions: what are grains and grain boundaries? What is texture? In the second part, the relationship between these microstructural features and the electrochemical activity reported in literature will be discussed.

2.2 Theoretical background

2.2.1 Grains

Most crystalline materials used in industrial applications are polycrystalline, meaning that they consist of aggregates of many very small crystals, called grains. Figure 2-1 illustrates schematically how grains and grain boundaries appear in a polycrystalline material.

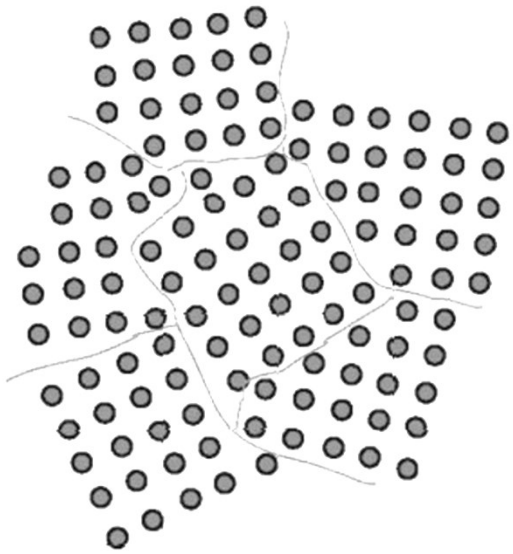

Figure 2-1: Representation of grains and grain boundaries in polycrystalline aggregates.

The crystallographic orientation varies from grain to grain. This crystallographic orientation is defined as a mathematical transformation, which correlates the sample or global coordinate system (attached to the sample) to the crystal or local coordinate system (attached to the crystal). This transformation can be represented by different mathematical expressions, which have one common characteristic, namely all of them require exactly three independent parameters to uniquely and unambiguously characterize the orientation. In this thesis the representation by Miller indices, Euler angles and the angle-axis description [1] is commonly used.

- Miller indices

A frequently used representation of crystal orientations in sheets consists of the specifications of the miller indices of that crystal plane which is parallel to the plane of the sheet, as well as the indices of the crystal direction parallel to the rolling direction (RD). Figure 2-2 shows a cubic crystal with [001] direction parallel to RD and the (110) plane parallel to the plane of the sheet. Depending on how the crystal symmetry is incorporated, the Miller indices can be written in different ways. Either with specific indices (hkl)[uvw] or either by non-specific or family indices {hkl}<uvw>, which refer to an entire set of symmetrically equivalent orientations.

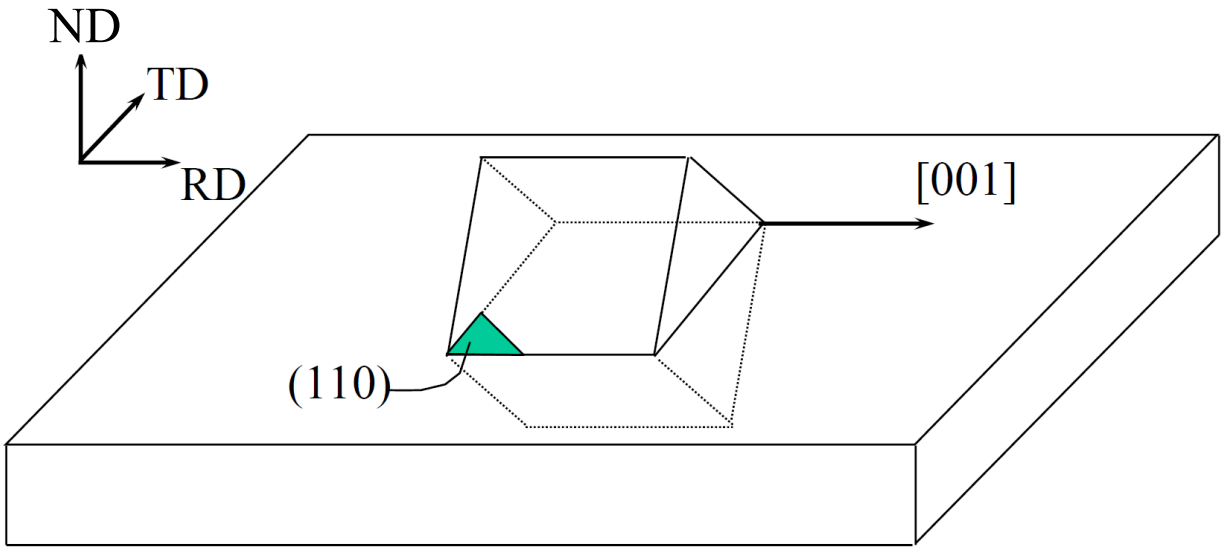

Figure 2-2: Cubic crystal with (110)[001] orientation.

- Euler angles

Any arbitrary crystallographic orientation can be uniquely characterized by three Euler angles φ_1, φ and φ_2. These refer to three consecutive rotations about the axes of the sample coordinate system (X_s Y_s Z_s) which bring these axes coinciding with the axes of the crystal coordinate system (X_c Y_c Z_c). The sequence of rotation and the selected rotation axes depend on the adopted convention.

One common convention is that defined by Bunge [1] in which the rotations are defined as follows (Fig. 2-3):

1. Rotation of the sample coordinate system about Z_s with an angle φ.
2. Rotation of the sample coordinate system about X_s with an angle φ until Z_s coincides with Z_c.
3. Rotation of sample coordinate system about Z_s with an angle φ_2 until X_s coincides with X_c and Y_s coincides with Y_c.

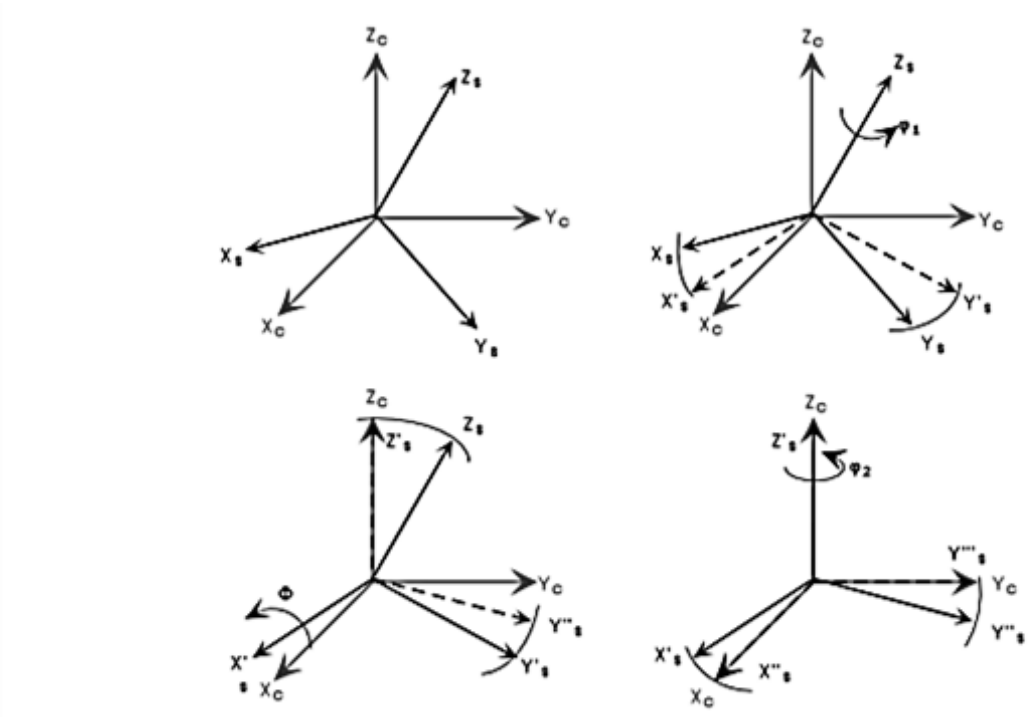

Figure 2-3: Representation of the Euler angles (φ_1, φ, φ_2) [2]

- Angle-axis

An alternative way of representing an orientation is by identifying one rotation axis ***n*** and an angle θ, so that by rotating the crystal reference frame over an angle θ around the axis ***n***, it coincides with the sample reference frame. Axis and angle together are called the axis-angle pair. One characteristic of the rotation axis is that this axis is common for both crystal and sample coordinate system. The axis-angle pair is also very well suited to describe the misorientation between two crystal reference frames.

2.2.2 Grain boundaries

2.2.2.1 General

A vast number of material properties, including corrosion, are controlled by the presence of crystal defects. These defects are conventionally classified according to their dimensions. Thus there are solutes (interstitials or substitutionals) and vacancies (point defects), dislocations (line defects), and grain or phase boundaries (planar defects).

A grain boundary is a structural defect comprising a region of misfit of a few atomic diameters wide, which separates two crystal volumes with different crystallographic orientations but with an identical crystallographic structure.

Five independent parameters must be specified to characterize the mesoscopic structure of a grain boundary. Three parameters describe the misorientation of the crystal lattice and two describe the orientation of the grain boundary plane. The implication of having five independent parameters is that the number of different grain boundary types is quite large [3]. If the five dimensional domain of grain boundary types is discretized in 10° intervals, there are roughly 6×10^3 different grain boundaries for a material with cubic symmetry like copper.

The axis-angle pair is used to specify the three parameters of lattice misorientation Δg, carried by the grain boundary. A misorientation will be specified by a crystallographic axis common to both crystals, [uvw], and a rotation angle θ around that axis. The grain boundary plane orientation, if determined, will be specified by the unit vector **n**.

The properties of grain boundaries are governed by both the intrinsic structural features associated with crystallographic lattice planes that compose the boundary plane and the extrinsic features such as dislocations, vacancies, segregated solutes and second phase particles. Therefore, knowledge of the boundary structure is a necessary condition for understanding the grain boundary behavior [4].

2.2.2.2 Grain boundary structure

Grain boundaries can be divided according to two criteria, cf. figure 2-4. On the one hand, a geometry based description and on the other hand a structure/energy based description. The geometry based description classifies the grain boundaries according to the position of the boundary plane normal ***n*** with respect to the crystal axis of rotation [uvw]. When the boundary plane is perpendicular to the rotation axis the boundary is referred to as a tilt boundary whereas for a twist boundary the boundary plane remains parallel to the rotation axis. In real materials however, grain boundaries have a mixed character of both tilt and twist contributions. Symmetric tilt boundaries are a special category of tilt boundaries. In symmetric tilt boundaries the grain boundary plane holds a symmetric position with respect to the two adjacent crystal lattices, which implies that the coordinates of the grain boundary plane in the crystal reference systems of the neighboring crystals, is identical.

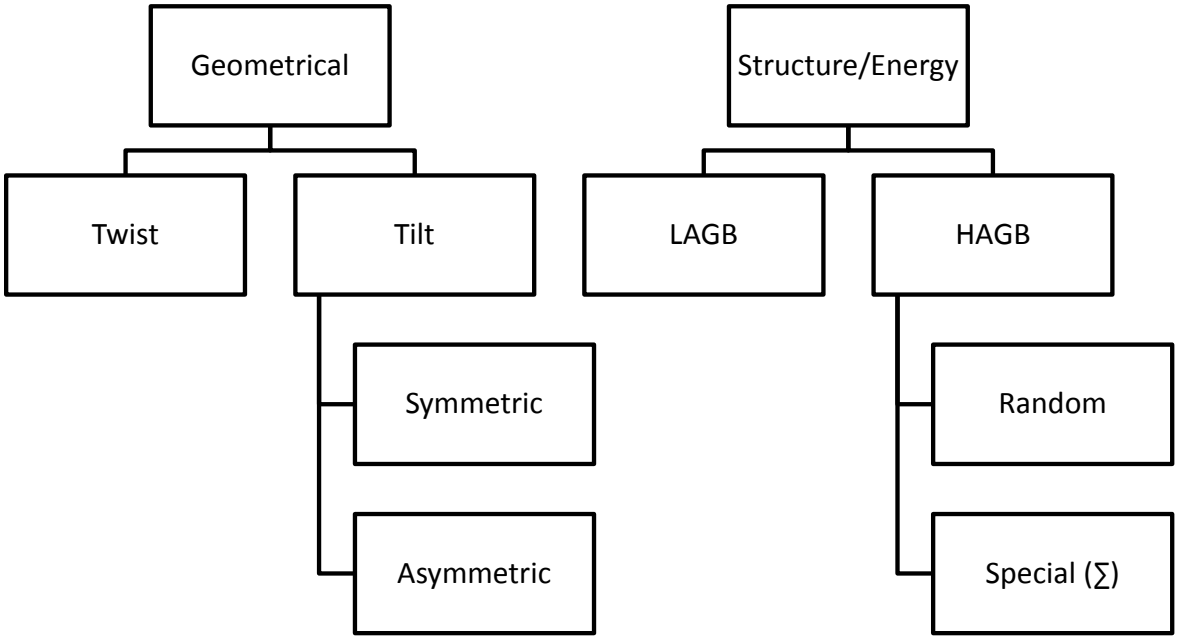

Figure 2-4: Grain boundary classification.

The structure/energy classification categorizes the grain boundaries into low angle grain boundaries (LAGBs) and high angle grain boundaries (HAGBs). This division is based on the dislocation model [5], which states that the geometry of any low angle boundary can be accommodated by a stack of dislocations. So grain boundaries are divided into LAGBs and HAGBs depending on the fact whether or not the crystal misorientation can be accommodated by a stacked array of dislocations. According to the conventional grain boundary theory, the

transition from low to high angle grain boundaries occurs in the range of 10° to 20° misorientation, i.e. the maximum misorientation that can be accommodated without overlap of the dislocations cores.

Although the structure of low angle boundaries is reasonably well understood, much less is known about the structure of high angle grain boundaries. There exists, however, a particular type of high angle grain boundaries, which have a characteristic structure and behave markedly different from random high angle boundaries. These potentially special boundaries are also known as coincident site lattice boundaries (CSLs). The concept of these CSL boundaries, as first proposed by Kronberg and Wilson [6] has considerably advanced the understanding of the structure of high angle boundaries.

Figure 2-5 shows a ∑5 coincident site lattice formed by simple cubic lattices. The grey circles represent one crystal; the red circles represent a neighboring crystal. The blue circles denote sites that are common to both lattices. These are lattice sites that form a common sublattice belonging to the two neighboring lattices; hence they constitute the coincident site lattice. The boundary between two such neighboring crystals, which have a common coincident lattice, is called a CSL boundary.

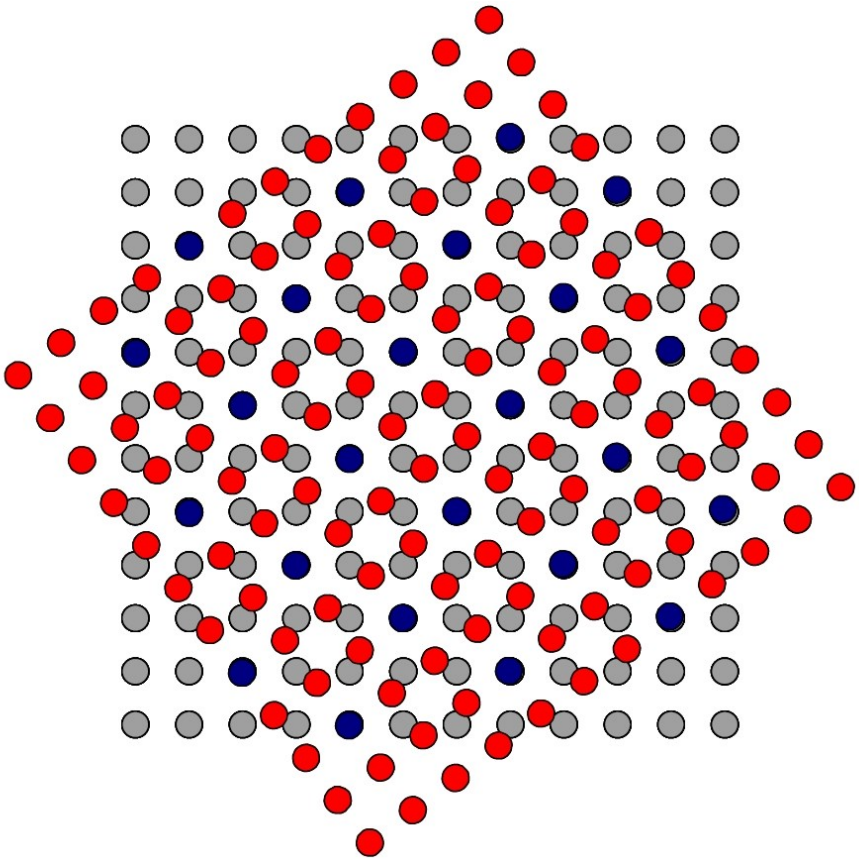

Figure 2-5: Schematic diagram showing a ∑5 CSL lattice [7].

The degree of lattice matching resulting from the relative rotation of the two grains is represented numerically by what is known as the coincidence index or ∑n. For cubic structures, like copper, n is an odd integer, with 1/n being the fraction of lattice points belonging to the coincidence lattice.

Although all grain boundaries can theoretically be classified using the CSL model, it has been suggested that boundaries with a coincident index of ∑n ≤ 29 (low CSL boundaries) possess properties which are generally more desirable than those with ∑n > 29 [8]. However, the concept of CSL boundaries only determines 3 of the 5 degrees of freedom (DOF) necessary to describe to the grain boundary, as it does not identify the grain boundary plane position [9-11]. Therefore it is safer to state that low CSL boundaries have the potential to be associated with special behavior. For instance, the coherent twin, a ∑3 boundary with a {111} grain boundary plane, always exhibits special properties, such as high corrosion resistance, whereas the incoherent twin displays other characteristics. This is linked with the amount of free energy associated with the grain boundary planes, which is the principal feature governing grain boundary behavior. Figure 2-6 shows schematically the influence of the grain boundary plane on the internal structure of a grain boundary. Both figure 2-6a and 2-6b show a ∑3 boundary, described by a 60° misorientation around <111>. However, when the boundary plane is a {111} plane (coherent twin), the boundary plane atoms fit perfectly into both grains. However, if the boundary plane is not parallel to the twinning plane (incoherent twin, figure 2-6b) the atoms at the grain boundary do not fit perfectly into each grain and the boundary energy is higher. Consequently, a CSL will only be special in terms of properties if it can maintain a periodic structure over the boundary plane [12-14].

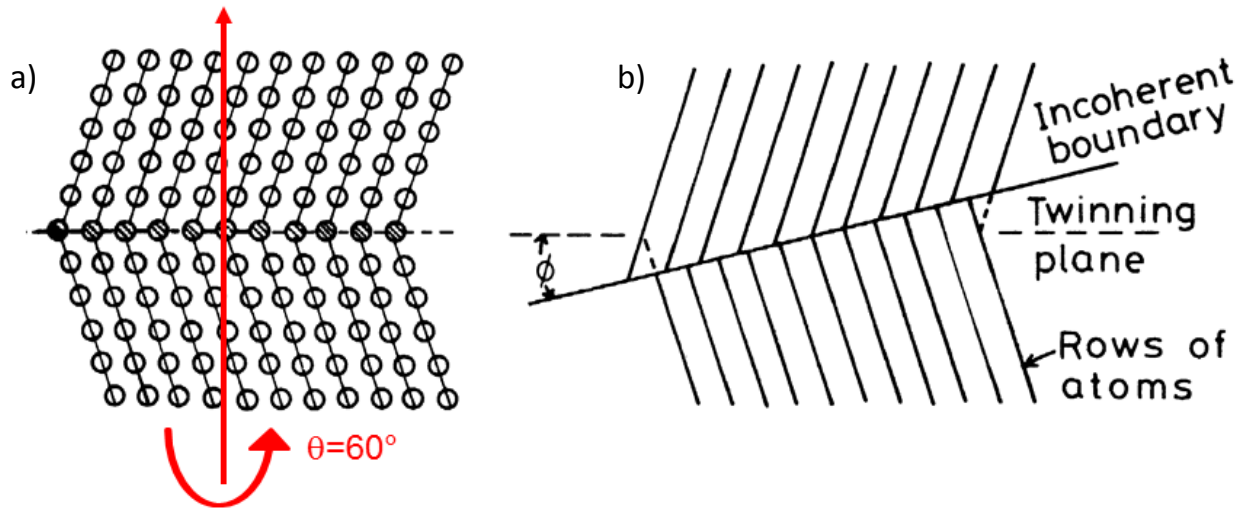

Figure 2-6: ∑3 boundaries. (a) Coherent twin boundary and (b) incoherent twin boundary [15].

2.2.2.3 Grain boundary energy

Knowledge of the energy of the grain boundaries is necessary for the fundamental understanding of all physical and chemical properties of metals. From a general point of view, the energy associated to a grain boundary depends on the boundary structure, which reflects the type and magnitude of misfit between the neighboring grains.

Read and Shockley [5] produced the first successful model, the dislocation model, to predict the energy dependence of grain boundaries. The model, which is limited to grain boundaries with a relatively small misorientation angle (< 15°), recognizes that lattice misorientations can be accommodated by dislocations. As the lattice misorientation increases from zero, it is approximately proportional to the density of dislocations in the grain boundary. As each dislocation carries a discrete amount of excess energy, the grain boundary energy is simply the sum of the dislocations energies plus the energy of interaction that arises as they are brought together to form the boundary.

Several computational studies are reported in literature in order to investigate the energy of grain boundaries as a function of their structure [16-20]. The grain boundary energy has been mostly investigated from an atomistic approach based on reliable inter-atomic potentials. However, with this method only a few millions of atoms can be considered which is too small to study real grain boundaries. Olmsted and Holm [17, 20] used the embedded atom method interatomic potentials to calculate the energy of a set of 388 distinct grain boundaries in several face-centered cubic (fcc) metals. They found that there is a rough correlation between the grain boundary energy and the net expansion (i.e. free volume) of the boundary. It was suggested that boundaries with the same mesoscopic structure tend to take on energetically similar microscopic configurations, and that there is an element dependent proportionality constant that scales with the boundary energy [17, 20]. The first assertion, i.e. grain boundaries that are close in crystallographic space are similar in energy, was already articulated by Brandon in 1966 [21].

Also many researchers have attempted to survey grain boundary energies using a number of experimental techniques in various metals [22, 23]. Even a thermodynamically correct geometrical model was proposed to measure the grain boundary triple line energy [24].

However, there is not yet a systematic experimental study on grain boundary energy on a statistically relevant set of data covering a wide range of grain boundaries in terms of crystal misorientation or boundary plane inclination. Since variations in grain boundary energy can influence the local reactivity of a metal in a specific environment and consequently the extent of the different corrosion processes, a detailed study on the grain boundary energy is required to fully understand the electrochemical behavior of a metal.

2.2.3 Texture

Crystallographic texture, or simply texture, refers to the orientation of the crystals within a polycrystalline sample. The importance of texture lies in the anisotropy of many material properties, like magnetization, induced by the non-random distribution of the orientations in the material, whether naturally occurring or as a result of thermomechanical processing. The analysis of texture in any material can be approached at two different length scales. Macrotexture refers to the analysis of the average texture displayed by a volume of material containing a large population of grains on the millimeter scale. Microtexture refers to the local presence of preferred orientations on the microstructural scale. The term microtexture also has the connotation of knowing the precise position of individual grains in the sample and inherently their size and shape. In this work macrotexture orientation measurements are obtained by X-ray diffraction (XRD). For determining the microstructure a wide variety of diffraction techniques are available in both transmission and scanning electron microscopes. In this work the electron backscatter diffraction (EBSD) technique attached to a scanning electron microscope (SEM) is used. Excellent reviews on this measurement technique can be found in literature [25-27].

The representation of crystallographic textures is complex. Until the mid-90's the standard method of representing textures was by means of pole figures. Nowadays there is increasing use of orientation distribution functions (ODFs). In this work, for representing the texture, ODFs are used.

Consider the case of a rolled sheet in which a particular volume element has the orientation (hkl)[uvw]. The orientation of this element can be described in terms of its three Euler angles, defined by Bunge [1]. Because three variables have been used to identify one specific orientation (hkl)[uvw], the ODF can be displayed in a 3D space defined by the three Euler angles as Cartesian coordinate axes in this space, cf. figure 2-7a. In our work we mostly work with rolled fcc material, for which the ODF is mostly shown as a series of slices cutting through the three dimensional Euler space at φ_2 = 0°, 5°, 10°, …., 90°; cf. figure 2-7b.

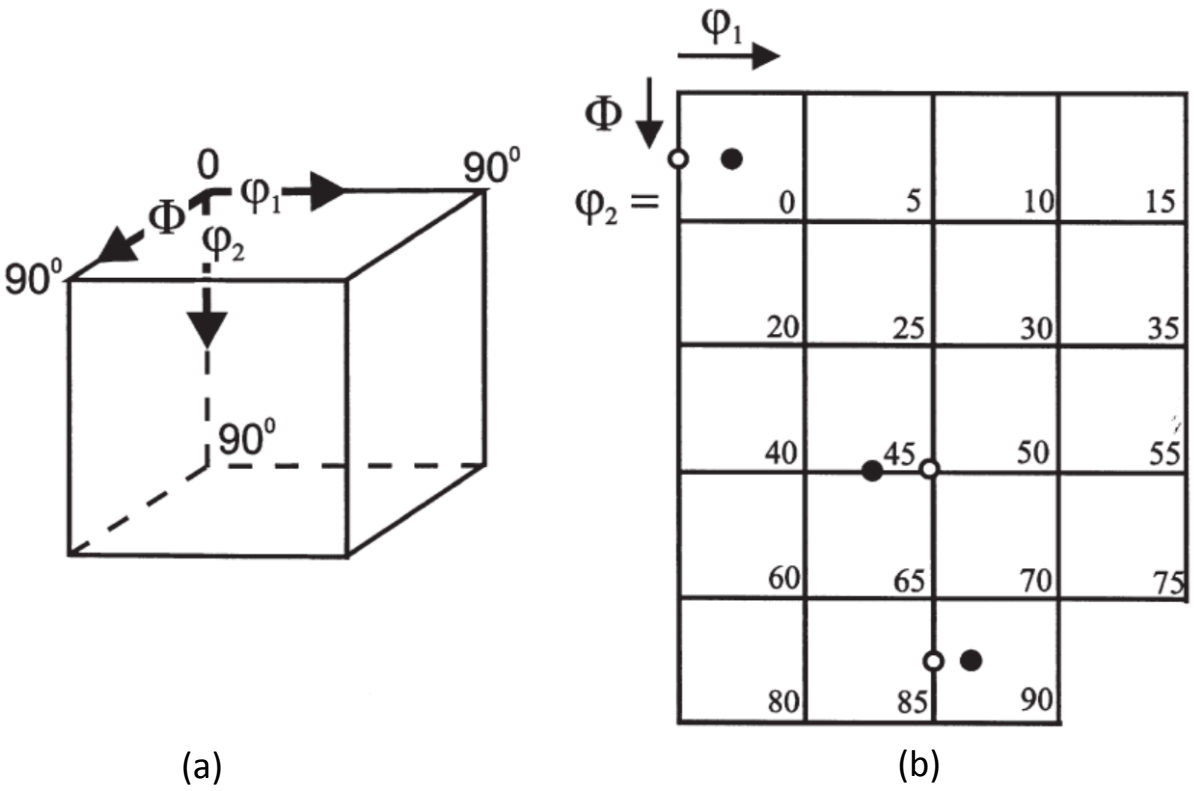

Figure 2-7: (a) Location of Euler angles in ODF space; (b) ODF sections showing location of {011}<211> (filled circles), and {110}<001> (open circles) orientations [4].

2.3 Relationship between microstructural features and electrochemical activity

The review of literature suggests that any microstructural feature in a metal that influences the reactivity of the surface can affect the electrochemical response of the material. For this reason, the reported influences of microstructural features as grain boundaries, grain orientation and grain size are listed in this section. Some authors even try to link the influence of a thermomechanical processing step on the electrochemical behavior. It becomes clear that a comprehensive description of the relationship between the microstructural features of a metal, governed by thermomechanical processing, and the electrochemical behavior is still lacking.

2.3.1 Grain boundaries

Grain boundaries and triple junctions have unique properties because of their relatively open structure compared to the lattice [28]. In certain electrolytes they can act as preferential sites for corrosion, but being unaffected in others [29]. The grain boundaries can increase the reactivity of a surface and this promotes either dissolution reactions but also passivation (or a more protective oxide) depending on the electrolyte.

Grain boundary electrochemistry has been studied by various local electrochemical techniques. These techniques include scanning vibrating electrode technique [30], scanning droplet cell [31], scanning Kelvin probe force microscopy [32] and micro-capillary cell technique [33]. These techniques provide a powerful tool for the development of a fundamental understanding of corrosion phenomena at grain boundaries. However, there are some limitations to the abilities of current local electrochemical techniques mainly due to their lateral resolution (around 20 µm). Some studies were reported in the literature on grain boundaries, observed at higher lateral resolution by using atomic force microscopy (AFM) [31, 34].

All these studies on intergranular corrosion with the different electrochemical techniques can be subdivided in two main categories. Either they evaluate corrosion as a function of the specific alloying elements and precipitates present in the grain boundaries [30, 35-37], or they link intergranular corrosion with the structure of the grain boundaries [38-43].

When the electrochemical response is observed as a function of the specific alloying elements and precipitates, the main hypothesis is the following: alloying elements alter the electron-conducting and/or ion-conducting properties of the oxide film on the metal surface. For example, in a low-Cr ferritic steel addition of Zr can prevent intergranular corrosion [37], while a low concentration of Cu in Zn inhibits the formation of a passivating film and reduces the stability of that film [35].

By looking at the research papers that link intergranular corrosion with the structure of the grain boundaries, different approaches can be distinguished. Some characterize the grain boundary only as a function of its misorientation angle. For instance, Miyamoto et al. found, by examining a Cu bicrystal, a critical misorientation angle that controls if either a ridge or a groove is formed at the grain boundary [43].

Other authors link the corrosion behavior with the CSL structure of the grain boundaries, assuming that CSL boundaries could have desirable properties in terms of corrosion resistance [38-41]. They found that most ∑1 grain boundaries (LAGB) are resistant to intergranular corrosion. And they all reported a higher resistance to intergranular corrosion for the boundaries with a low ∑ CSL value. However, Wolf et al. [44] indicated that a low ∑ CSL is a necessary, but not a sufficient criterion for special properties. They revealed that the properties of a grain boundary are not only dependent on the crystal misorientation, but also on the grain boundary plane. As a consequence of this, several papers have been written [9, 10, 12, 45, 46] about the associations between intergranular corrosion and grain boundary geometry described in terms of 5 degrees of freedom. The most recurrent observation in these papers is the higher corrosion resistance of the ∑3 boundary with a {111} boundary plane (i.e. coherent ∑3 boundaries).

2.3.2 Grain orientation

The crystallographic orientation and its packing density are believed to have an influence on the electrochemical behavior of that specific grain [47-57].

Some authors use single crystals to explore the influence of grain orientation on corrosion behavior [47, 48]. For example, Schultze et al. [47] found out that in a Zr and a Ta single crystal, the oxide formation increases with decreasing surface atom density. Also several studies have been done on copper single crystals. By means of EC-STM Kunze et al [58] studied the duplex oxide film formed on copper (111) and (001) monocrystals. A slightly thicker oxide layer is formed on the Cu(111) surface compared to the Cu(001) surface. The higher stability of the Cu_2O layer formed on the Cu(111) oriented grain compared to that formed on the Cu(001) monocrystal was also confirmed. Additionally, there are some publications on pure bi-crystals. Schreiber et al. [49] measured different current densities on the crystallographic (100) and (111) planes in a bi-crystal of pure iron. It is almost impossible, however, to correlate the results on single- and bi-crystals [47, 48] with those on textured polycrystalline samples.

Therefore, different authors quantify the corrosion kinetics and the oxidation as a function of the differently oriented grains in a polycrystalline material. In a FeAlCr alloy, Lill et al. [59] concluded, by means of cyclic voltammetry in a microcapillary cell, that the critical current density on a grain with <100> // ND orientation is 53% higher when compared to a <111> // ND oriented grain. Park et al. [52] observed on the surface of a polycrystalline Zn sample, a strong dependence of oxide growth on the grain orientation. They found out that oxide formation was greater on low index grains compared to high indexed ones. Also the grain orientation dependent dissolution behavior was studied. With use of Scanning Electron Microscopy (SEM) and Atomic Force Microscopy (AFM), Wang et al. [56] discovered that for Alloy 690, a high-chromium nickel alloy, the dissolution rates increases when the grain surface diverges to {111}.

2.3.3 Grain size

Several works [60, 61] have attempted to reveal the relationship between grain size and the electrochemical behavior over a wide range of grain sizes. However, the existing literature is often contradictory. Since also the different processing routes used to decrease the grain size can influence other parameters like texture, residual stresses and impurity segregation, the influence of the grain size on the electrochemical behavior remains as yet unclear.

In Al and Zn, Osorio et al. [62] studied the role of different microstructural morphologies and grain sizes, demonstrating that grain size and morphology can affect the cathodic branch of the potentiodynamic polarization curves in a NaCl solution. They reported that microstructures with larger grains exhibit more noble corrosion potentials and are related with lower corrosion rates. Song et al. [63] demonstrated that ultrafine grains had a positive influence on the pitting

behavior of industrial Al. They attribute this behavior to a relatively dense oxide film, caused by the higher amount of grain boundaries in the material. The increased corrosion resistance with decreasing grain size in Al, was also confirmed by Ralston et al. [64].

When studying the effect of grain size on the corrosion resistance of Cu and Cu alloys, mixed results have been presented. The effect of grain refinement has been reported to have either little effect [65, 66], produce increased susceptibility [29, 67, 68], or decreased susceptibility [69-74], based on the electrochemical behavior in a number of electrolytes. In general, changes in polarization behavior as a function of grain size, whether positive or negative, tend to be relatively small, possibly suggesting that grain size or grain boundary density have little direct effect on the corrosion resistance in Cu and Cu alloys. However, fine grained Cu does appear to be less susceptible to localized corrosion, even if the electrochemical tests indicate a faster overall corrosion rate [29, 65, 67, 75].

Via scanning kelvin electron probe measurement [74] nanocrystalline Cu was termed as being more electrochemically stable, with a higher electron work function than coarser grained microstructures. In NaOH electrolytes, improved passive film stability was attributed to higher grain boundary density, which was believed to contribute to the rapid formation of a passive layer, through diffusion and more active electrons near grain boundaries [74, 76]. However, passive films formed on fine grained Cu also have been identified as less protective compared to the ones formed on coarse grained samples, with higher activity of atoms near the surface and grain boundaries possible interfering with oxide formation, resulting in a more corrosion susceptible alloy [29, 68].

Thus, also in Cu and Cu alloys, the effects of processing are intertwined with the observed corrosion behavior and the exact processes employed to obtain various grain sizes may have a large impact on the electrochemical response. For example, localized corrosion, in some cases, may be due to impurity segregation to grain boundaries caused by annealing applied to coarsen the microstructure [29, 67]. The degree to which differences in corrosion susceptibility are due to grain size or other microstructural/chemical effects induced by the heat treatment is not clear. E.g., homogeneous corrosion, as opposed to localized intergranular attack, observed in fine grained Cu produced by equal channel angular pressing (ECAP) may be due in part to the residual stress as much as the small grain size [29, 65].

2.3.4 Thermomechanical processing

The existing literature on the effect of thermomechanical processing on intergranular corrosion behavior is often contradictory. Both an increased and a decreased susceptibility to intergranular corrosion after cold rolling are observed. Barbucci et al. [77] and Songbo et al. [78] observed a raise in corrosion rate after cold rolling, respectively in an AISI 301 stainless steel and Cu, while Nam et al. [79] detected a decrease in corrosion rate with an increase in the

degree of cold reduction in low-alloy steel. Also higher susceptibility to localized attack due to rolled-in oxides is reported [33].

The published papers are inconclusive in as far that they do not allow identifying the contribution of individual microstructural effects on the electrochemical behavior produced by the thermomechanical processing.

2.4 Conclusions

In order to increase the sustainability of metals, a more detailed understanding of the corrosion phenomenon is of crucial importance. The review of literature suggests an important influence of the microstructure on the electrochemical activity.

In this chapter, the different microstructural features of metals were discussed. In the second part, a literature review is given of the effect of these microstructural features on the electrochemical activity of the metal.

All studies on grain boundary electrochemistry with various local electrochemical techniques demonstrate an effect of the grain boundary structure and alloying elements on the grain boundary corrosion behavior. However, there are some limitations to the abilities of the current local electrochemical techniques, mainly due to their lateral resolution and the limited field of view. For this reason, only limited information on the electrochemical behavior of a few specific grain boundaries is provided.

Only a few studies are published on the influence of the crystallographic orientation of the grain on the corrosion behavior. They correlate the differences in electrochemical activity of the different oriented grains with surface energy, packing density and surface atom density.

When studying the effect of the grain size on corrosion resistance, contradictory results are obtained. This is because the different processing routes to alter the grain size also influence other microstructural features such as grain boundary structure and grain orientation, but also chemical properties of grain boundaries may be affected by the processing route, such as e.g. the concentration of GB segregated elements. Hence, only limited conclusions can be drawn on the effects of TMP on the electrochemical behavior of a metal.
Most studies demonstrate that the local, microscopic features influence the electrochemical behavior, but a physically based relationship is still lacking.

By means of a controlled variation of the microstructure of a carefully selected metal and a thorough characterization of the electrochemical behavior, it is the objective of this work to achieve a better understanding of the link between the microstructural features of a metal and its electrochemical behavior.

2.5 References

1. Bunge, H.J., Texture analysis in Materials Science. 1982, London: Butterworths.

2. TSL and I. EDAC, OIM Analysis Users Manual, ed. T. laboratories. 2001.

3. Rohrer, G.S., D.M. Saylor, B. El Dasher, B.L. Adams, A.D. Rollett and P. Wynblatt,, The distribution of internal interfaces in polycrystals. Zeitschrift Fur Metallkunde, 2004. 95(4): p. 197-214.

4. Humphreys, F.J. and M. Hatherly, Recrystallization and Related Annealing Phenomena. 2004, Oxford: Elsevier Ltd.

5. Read, W.T. and W. Shockley, Dislocation Models of Crystal Grain Boundaries. Physical Review, 1950. 78(3): p. 275-289.

6. Kronberg, M.L. and F.H. Wilson, Trans. Mettal. Soc. A.I.M.E., 1949. 185: p. 501.

7. Verbeken, K., Orientation selection in ultra low carbon steel during thermally activated phenomena induced by cold deformation, in Department of Materials Science and Engineering. 2004, Ghent University: Ghent.

8. Watanabe, T., Structural effects on grain-boundary segregation, hardening and fracture. Journal De Physique, 1985. 46(NC-4): p. 555-566.

9. Randle, V., 'Special' boundaries and grain boundary plane engineering. Scripta Materialia, 2006. 54(6): p. 1011-1015.

10. Randle, V., The role of the grain boundary plane in cubic polycrystals. Acta Materialia, 1998. 46(5): p. 1459-1480.

11. Rohrer, G.S., Grain boundary energy anisotropy: a review. Journal of Materials Science, 2011. 46(18): p. 5881-5895.

12. Randle, V., Twinning-related grain boundary engineering. Acta Materialia, 2004. 52(14): p. 4067-4081.

13. Randle, V., The coincidence site lattice and the 'sigma enigma'. Materials Characterization, 2001. 47(5): p. 411-416.

14. Randle, V., H. Davies and I. Cross, Grain boundary misorientation distributions. Current Opinion in Solid State & Materials Science, 2001. 5(1): p. 3-8.

15. Porter, D.A. and K.E. Easterling, Phase Transformations in Metals and Alloys, Third Edition (Revised Reprint). 1992: Taylor & Francis.

16. Rohrer, G.S., E.A. Holm, A.D. Rollett, S.M. Foiles, J. Li and D.L. Olmsted, Comparing calculated and measured grain boundary energies in nickel. Acta Materialia, 2010. 58(15): p. 5063-5069.

17. Holm, E.A., D.L. Olmsted and S.M. Foiles, Comparing grain boundary energies in face-centered cubic metals: Al, Au, Cu and Ni. Scripta Materialia, 2010. 63(9): p. 905-908.

18. Uesugi, T. and K. Higashi, First-principles calculation of grain boundary energy and grain boundary excess free volume in aluminum: role of grain boundary elastic energy. Journal of Materials Science, 2011. 46(12): p. 4199-4205.

19. Alexander, K.C. and C.A. Schuh, Exploring grain boundary energy landscapes with the activation-relaxation technique. Scripta Materialia, 2013. 68(12): p. 937-940.

20. Olmsted, D.L., S.M. Foiles and E.A. Holm, Survey of computed grain boundary properties in face-centered cubic metals: I. Grain boundary energy. Acta Materialia, 2009. 57(13): p. 3694-3703.

21. Brandon, D.G., Structure of high-angle grain boundaries. Acta Metallurgica, 1966. 14(11): p. 1479-&.

22. Amouyal, Y. and E. Rabkin, A scanning force microscopy study of grain boundary energy in copper subjected to equal channel angular pressing. Acta Materialia, 2007. 55(20): p. 6681-6689.

23. Molodov, D.A., C. Gunster, G. Gottstein and L.S. Shvindlerman, A novel experimental approach to determine the absolute grain boundary energy. Philosophical Magazine, 2012. 92(36): p. 4588-4598.

24. Zhao, B., J.C. Verhasselt, L.S. Shvindlerman and G. Gottstein, Measurement of grain boundary triple line energy in copper. Acta Materialia, 2010. 58(17): p. 5646-5653.

25. Dingley, D.J., A comparison of diffraction techniques for the sem. Scanning Electron Microscopy, 1981: p. 273-286.

26. Wright, S.I., J.W. Zhao and B.L. Adams, Automated-determination of lattice orientation from electron backscattered kikuchi diffraction patterns. Textures and Microstructures, 1991. 13(2-3): p. 123-131.

27. Randle, V., Electron backscatter diffraction: Strategies for reliable data acquisition and processing. Materials Characterization, 2009. 60(9): p. 913-922.

28. Flewitt, P.E.J. and R.K. Wild, Grain boundaries: their microstructure and chemistry, ed. L. John Wiley ans Sont. 2001, Chichester: John Wiley and Sons, Ltd.

29. Luo, W., C. Qian, X.J. Wu and M. Yan, Electrochemical corrosion behavior of nanocrystalline copper bulk. Materials Science and Engineering a-Structural Materials Properties Microstructure and Processing, 2007. 452: p. 524-528.

30. Liu, Z.Y., X.G. Li and Y.F. Cheng, In-situ characterization of the electrochemistry of grain and grain boundary of an X70 steel in a near-neutral pH solution. Electrochemistry Communications, 2010. 12(7): p. 936-938.

31. Woldemedhin, M.T., D. Raabe and A.W. Hassel, Grain boundary electrochemistry of beta-type Nb-Ti alloy using a scanning droplet cell. Physica Status Solidi a-Applications and Materials Science, 2011. 208(6): p. 1246-1251.

32. Andreatta, F., A. Turco, I. de Graeve, H. Terryn, J.H.W. de Wit and L. Fedrizzi, SKPFM and SEM study of the deposition mechanism of Zr/Ti based pre-treatment on AA6016 aluminum alloy. Surface & Coatings Technology, 2007. 201(18): p. 7668-7685.

33. Buytaert, G., Premendra, J.H.W. de Wit, L. Katgerman, B. Kernig, H.J. Brinkman and H. Terryn, Electrochemical investigation of rolled-in subsurface layers in commercially pure aluminium alloys with the micro-capillary cell technique. Surface & Coatings Technology, 2007. 201(8): p. 4553-4560.

34. Skidmore, T., R.G. Buchheit and M.C. Juhas, Grain boundary energy vs. misorientation in Iconel (R) 600 alloy as measured by thermal groove and OIM analysis correlation. Scripta Materialia, 2004. 50(6): p. 873-877.

35. van den Bos, C., H.C. Schnitger, X. Zhang, A. Hovestad, H. Terryn and J.H.W. De Wit, Influence of alloying elements on the corrosion resistance of rolled zinc sheet. Corrosion Science, 2006. 48(6): p. 1483-1499.

36. Caicedo-Martinez, C.E. E.V. Koroleva, G.E. Thompson, P. Skeldon, K. Shimizu, G. Hoellrigl, C. Campbell and E. McAlpine, Influence of impurities in aluminium on surface treatment. Corrosion Science, 2002. 44(11): p. 2611-2620.

37. Park, J.H., J.K. Kim, B.H. Lee, H.S. Seo and K.Y. Kim, Effect of Zr addition on intergranular corrosion of low-chromium ferritic stainless steel. Scripta Materialia, 2014. 76: p. 77-80.

38. Kokawa, H., M. Shimada, M. Michluchi, Z.J. Wang and Y.S. Sato, Arrest of weld-decay in 304 austenitic stainless steel by twin-induced grain boundary engineering. Acta Materialia, 2007. 55(16): p. 5401-5407.

39. Kim, S.H., U. Erb, K.T. Aust and G. Palumbo, Grain boundary character distribution and intergranular corrosion behavior in high purity aluminum. Scripta Materialia, 2001. 44(5): p. 835-839.

40. Lin, P., G. Palumbo, U. Erb and K.T. Aust, Influence of grain-boundary-character-distribution on sensitization and intergranular corrosion of alloy-600. Scripta Metallurgica Et Materialia, 1995. 33(9): p. 1387-1392.

41. Hill, L.R., V. Randle and O. Engler, Five parameter distribution of planes in AA 5182 aluminium alloys with relevance to intergranular corrosion resistance. Materials Science and Technology, 2013. 29(8): p. 1006-1011.

42. Zhao, Y., I.C. Cheng, M.E. Kassner and A.M. Hodge, The effect of nanotwins on the corrosion behavior of copper. Acta Materialia, 2014. 67: p. 181-188.

43. Miyamoto, H., K. Yoshimura, T. Mimaki and M. Yamashita, Behavior of intergranular corrosion of < 011 > tilt grain boundaries of pure copper bicrystals. Corrosion Science, 2002. 44(8): p. 1835-1846.

44. Wolf, D., On the relationship between symmetrical tilt, twist, special, and favored grain-boundaries. Journal De Physique, 1985. 46(NC-4): p. 197-211.

45. Randle, V., G.S. Rohrer, H.M. Miller, M. Colemanand G.T. Owen, Five-parameter grain boundary distribution of commercially grain boundary engineered nickel and copper. Acta Materialia, 2008. 56(10): p. 2363-2373.

46. Miyamoto, H., K. Ikeuchi and T. Mimaki, The role of grain boundary plane orientation on intergranular corrosion of symmetric and asymmetric 110 tilt grain boundaries in directionally solidified pure copper. Scripta Materialia, 2004. 50(12): p. 1417-1421.

47. Schultze, J.W., M. Pilaski, M.M. Lohrengel and U. Konig, Single crystal experiments on grains of polycrystalline materials: Oxide formation on Zr and Ta. Faraday Discussions, 2002. 121: p. 211-227.

48. Ashton, R.F. and M.T. Hepworth, Effect of crystal orientation on anodic polarization and passivity of zinc. Corrosion, 1968. 24(2): p. 50-56.

49. Schreiber, A., J.W. Schultze, M.M. Lohrengel, F. Karman and E. Kalman, Grain dependent electrochemical investigations on pure iron in acetate buffer pH 6.0. Electrochimica Acta, 2006. 51(13): p. 2625-2630.

50. Davepon, B., J.W. Schultze, U. Konig and C. Rosenkranz, Crystallographic orientation of single grains of polycrystalline titanium and their influence on electrochemical processes. in Frontiers of Surface Engineering Conference and Exhibition (FSE 2001). 2001. Nagoya, Japan: Elsevier Science Sa.

51. Lill, K.A., A.W. Hassel, G. Frommeyer and M. Stratmann, Scanning droplet cell investigations on single grains of a FeAlCr light weight ferritic steel. in 5th International Symposium on Electrochemical Micro and Nano Technologies. 2004. Tokyo, JAPAN: Pergamon-Elsevier Science Ltd.

52. Park, C.J., M.M. Lohrengel, T. Hamelmann, M. Pilaski and H.S. Kwon, Grain-dependent passivation of surfaces of polycrystalline zinc. Electrochimica Acta, 2002. 47(21): p. 3395-3399.

53. Konig, U. and B. Davepon, Microstructure of polycrystalline Ti and its microelectrochemical properties by means of electron-backscattering diffraction (EBSD). Electrochimica Acta, 2001. 47(1-2): p. 149-160.

54. Maurice, V., L.H. Klein, H.H. Strehblow and P. Marcus, In situ STM study of the surface structure, dissolution, and early stages of electrochemical oxidation of the Ag(111) electrode. Journal of Physical Chemistry C, 2007. 111: p. 16351-16361.

55. Wiame, F., V. Maurice and P. Marcus, Initial stages of oxidation of Cu(111). Surface Science, 2007. 601(5): p. 1193-1204.

56. Wang, S.Y. and J.Q. Wang, Effect of grain orientation on the corrosion behavior of polycrystalline Alloy 690. Corrosion Science, 2014. 85: p. 183-192.

57. Song, J.M., Y.S. Zou, C.C. Kuo and S.C. Lin, Orientation dependence of the electrochemical corrosion properties of electrodeposited Cu foils. Corrosion Science, 2013. 74: p. 223-231.

58. Kunze, J., V. Maurice, L.H. Klein, H.H. Strehblow and P. Marcus In situ STM study of the duplex passive films formed on Cu(111) and Cu(001) in 0.1 M NaOH. Corrosion Science, 2004. 46(1): p. 245-264.

59. Lill, K.A., A.W. Hassel, G. Frommeyer and M. Stratmann, Scanning droplet cell investigations on single grains of a FeAlCr light weight ferritic steel. Electrochimica Acta, 2005. 51(5): p. 978-983.

60. Ralston, K.D., N. Birbilis and C.H.J. Davies, Revealing the relationship between grain size and corrosion rate of metals. Scripta Materialia, 2010. 63(12): p. 1201-1204.

61. Ralston, K.D. and N. Birbilis, Effect of Grain Size on Corrosion: A Review. Corrosion, 2010. 66(7).

62. Osorio, W.R., C.M. Freire and A. Garcia, The role of macrostructural morphology and grain size on the corrosion resistance of Zn and Al castings. Materials Science and Engineering a-Structural Materials Properties Microstructure and Processing, 2005. 402(1-2): p. 22-32.

63. Song, D., A.B. Ma, J.H. Jiang, P.H. Lin and D.H. Yang, Corrosion behavior of ultra-fine grained industrial pure Al fabricated by ECAP. Transactions of Nonferrous Metals Society of China, 2009. 19(5): p. 1065-1070.

64. Ralston, K.D., J.G. Brunner, S. Virtanen and N. Birbilis, Effect of Processing on Grain Size and Corrosion of AA2024-T3. Corrosion, 2011. 67(10): p. 10.

65. Hellmig, R.J., M. Janecek, B. Hadzima, O.V. Gendelman, M. Shapiro, X. Molodova, A. Springer and Y. Estrin, A portrait of copper processed by equal channel angular pressing. Materials Transactions, 2008. 49(1): p. 31-37.

66. Yu, B., P. Woo and U. Erb, Corrosion behaviour of nanocrystalline copper foil in sodium hydroxide solution. Scripta Materialia, 2007. 56(5): p. 353-356.

67. Vinogradov, A., T. Mimaki, S. Hashimoto and R. Valiev, On the corrosion behaviour of ultra-fine grain copper. Scripta Materialia, 1999. 41(3): p. 319-326.

68. Barbucci, A., G. Farne, P. Matteazzi, R. Riccieri and G. Cerisola, Corrosion behaviour of nanocrystalline Cu90Ni10 alloy in neutral solution containing chlorides. Corrosion Science, 1999. 41(3): p. 463-475.

69. Wang, Y.M., M.W. Chen, F.H. Zhou and E. Ma, High tensile ductility in a nanostructured metal. Nature, 2002. 419(6910): p. 912-915.

70. Gobernado, P., R.H. Petrov and L.A.I. Kestens, Recrystallized {311} < 136 > orientation in ferrite steels. Scripta Materialia, 2012. 66(9): p. 623-626.

71. Jasieéski, Z., H. Paul, A. Piątkowski and A. Litwora, Microstructure and Texture of Copper Single Crystal of (112)[111] Orientation Undergoing Channel-Die Compression at 77 K. Journal of Materials Processing Technology, 1995. 53(1–2): p. 187-194.

72. Wang, Y.M., M.W. Chen, H.W. Sheng and E. Ma, Nanocrystalline grain structures developed in commercial purity Cu by low-temperature cold rolling. Journal of Materials Research, 2002. 17(12): p. 3004-3007.

73. Nikfahm, A., I. Danaee, A. Ashrafi and M.R. Toroghinejad, Effect of Grain Size Changes on Corrosion Behavior of Copper Produced by Accumulative Roll Bonding Process. Materials Research-Ibero-American Journal of Materials, 2013. 16(6): p. 1379-1386.

74. Tao, S. and D.Y. Li, Tribological, mechanical and electrochemical properties of nanocrystalline copper deposits produced by pulse electrodeposition. Nanotechnology, 2006. 17(1): p. 65-78.

75. Yu, J.K., E.H. Han, L. Lu, X.J. Wei and M. Leung , Corrosion behaviors of nanocrystalline and conventional polycrystalline copper. Journal of Materials Science, 2005. 40(4): p. 1019-1022.

76. Elkedim, O., H.S. Cao, C. Meunier and E. Gaffet, Preparation of nanocrystalline copper by hot and cold compaction : Characterization of mechanical and electrochemical properties, in Mechanically Alloyed, Metastable and Nanocrystalline Materials, Part 2, M.D. Baro and S. Surinach, Editors. 1998. p. 843-848.

77. Barbucci, A., M. Delucchi, M. Panizza, M. Sacco and G. Cerisola, Electrochemical and corrosion behaviour of cold rolled AISI 301 in 1 M H2SO4. Journal of Alloys and Compounds, 2001. 317: p. 607-611.

78. Songbo, Y. and D.Y. Li, Effects of prior cold work on corrosion and corrosive wear of copper in HNO/sub 3/ and NaCl solutions. Materials Science & Engineering A (Structural Materials: Properties, Microstructure and Processing), 2005. 394(1-2): p. 266-276.

79. Nam, N.D., D.Y. Lee, J.G. Kim and N.J. Park, Effect of Cold Rolling on the Corrosion Properties of Low-Alloy Steel in an Acid-Chloride Solution. Metals and Materials International, 2014. 20(3): p. 469-474.

Chapter 3
Material and microstructural characterization methods

3.1 Introduction

Since the goal of this doctoral dissertation is to obtain a better understanding of the link between the microstructural features of the metal and its electrochemical behavior, a systematic approach is needed. This consists on the one hand of a controlled variation and detailed characterization of the microstructure of a carefully selected metal and, on the other hand, meticulous quantification of the resulting electrochemical behavior.

In this chapter the choice of the model system will be discussed and the different techniques to obtain a full characterization of the microstructure will be elucidated.

3.2 Material selection

3.2.1 High purity copper

Nearly all metals for structural applications consist of many grains with different crystallographic orientations. For the purpose of the present study, the objective is to consider a relatively simple model system of which the microstructure can be controlled. As revised in the literature review (chapter 2), studies are often focused on metals such as stainless steel, aluminum and titanium, which are covered by a native oxide film. This film dominates the electrochemical response and thus complicates the interpretation and correlation with the underlying metal microstructure. To circumvent this problem copper will be used as a model system. Copper can be obtained with a high purity and the nm-thin surface oxide film does not disturb the electrochemical behavior to the same extent as for less noble metals. It is also possible to remove this oxide film [1]. When working with pure copper, the compositional effects of alloying elements on the electrochemical behavior can be excluded. Another reason why copper is chosen as the model system is because its medium stacking fault energy. As a result of this, copper is a metal that shows abundant annealing twinning when exposed to a thermomechanical treatment. This offers an extra degree of freedom to control the population of specific grain boundary types in the microstructure [2-4].

The investigated material in this dissertation is high purity cast copper, obtained from Aurubis® (Belgium). Chemical analysis confirmed that it contained no sulfur and only a minute amount of oxygen (27 ppm). The microstructure and texture of this material will be varied by thermomechanical processing, which includes hot rolling, room temperature rolling and

cryogenic rolling and annealing (chapter 4). In this way, the grain size, the crystallographic texture and the grain boundary orientation can be controlled to some extent by varying the deformation and annealing parameters.

3.2.2 Crystal structure of copper

Typical for metals and all crystalline materials in general, is the fact that all atoms are stacked in a repeating or periodic array over large atomic distances. A large number of the physical and chemical properties of crystalline materials depend on the crystal structure, such as e.g. density, heat transfer and electrical conductivity.

To describe the crystalline structure of a material, it is convenient to subdivide this ordered atomic structure into small repeat entities called unit cells. This unit cell is the basic structural unit of the crystal structure and defines the crystal structure on the basics of its geometry and atomic positions within.

Copper has a face-centered cubic (fcc) crystal structure (Fig. 3-1). This means that copper has a unit cell of cubic geometry, with atoms located at each of the corners and the centers of all the cube faces. Each corner atom is shared among eight unit cells, whereas a face-centered atom belongs to only two. Therefore, one-eighth of each of the eight corner atoms and one-half of each of the six face atoms, or a total of four whole atoms, is assigned to a given unit cell.

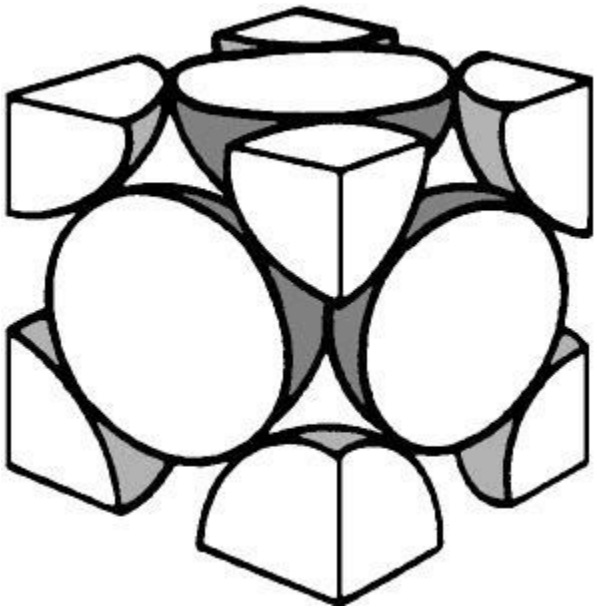

Figure 3-1: Face-centered cubic unit cell

Other familiar metals having the fcc crystal structure are aluminum, silver, gold, nickel and lead.

3.2.3 Electrochemical behavior of copper

Thermodynamically, the electrochemical behavior of copper can be derived from the Pourbaix diagrams [5] as illustrated in figure 3-2a for copper immersed in pure H_2O and 3-2b, where copper is immersed in H_2O that contains chloride ions.

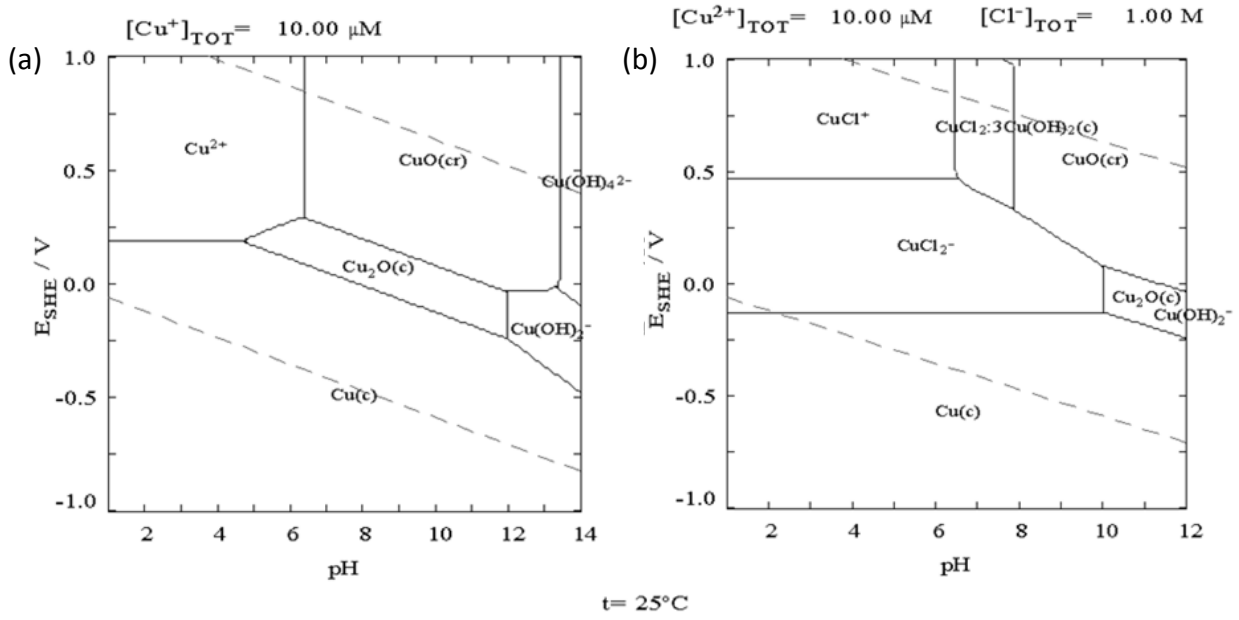

Figure 3-2: Pourbaix diagram of Cu immersed in (a) H_2O and (b) H_2O containing Cl^- ions [5].

The Pourbaix diagram maps out possible stable phases of an aqueous electrochemical system. The different lines correspond to the chemical and electrochemical equilibrium conditions, where the activities of the species are equal on both sides of that line. Pourbaix diagrams are used to predict whether or not a metal corrodes, passivates or is immune to corrosion. In the case of copper (Fig. 3-2) different domains of reactivity of copper can be seen: immunity (Cu), areas of passivation (CuO and Cu_20) and corrosion (Cu^+ and Cu^{2+}). The large area of stability of Cu is noticed.

No passivation of Cu is seen in the acid region (pH < 7) and in solutions with a pH > 12. In solutions with a pH between 7 and 12 the passivation of Cu is possible. This implies that when working in an acid region, the air-formed oxide layer can be reduced, allowing an oxide-free surface to work with. However, always take in account that these diagrams just give thermodynamic information, no information on reaction rate or kinetic effects can be retrieved from them.

Comparing figure 3-2a and 3-2b, the effect of chlorides on the electrochemical activity of Cu is shown. When chloride ions are present in the solution the size of the stability zone of Cu decreases. Also the area where soluble products are formed enlarges. This comparison shows that chloride is a potential threat for the stability of copper and its alloys.

3.3 Microstructural characterization techniques

To evaluate the microstructural characteristics and the microtexture of Cu, electron backscatter diffraction (EBSD), a technique that can be attached to a scanning electron microscope (SEM) will be used. The macrotexture will be obtained by X-ray diffraction (XRD) using texture goniometers.

3.3.1 Sample preparation

Sample preparation for X-ray diffraction consists of grinding and mechanical polishing down to 1 µm coarse diamond paste.

For EBSD measurements, two additional steps were applied namely an oxide polishing step with OPS colloidal silica (0.25 µm) followed by and electrolytic polishing step with the Lectropol 5® (15V, 30s) with electrolyte D2 from Struers®, which is a phosphoric acid based solution.

3.3.2 Electron backscatter diffraction

Electron backscatter diffraction (EBSD) is based on the acquisition and analysis of Kikuchi diffraction patterns from bulk samples in the scanning electron microscope (SEM).

3.3.2.1 Data acquisition

Figure 3-3 gives a schematic representation of a typical EBSD installation. When a stationary electron beam hits the specimen surface, it interacts with a given volume of crystalline mater. Elastic collisions of incident electrons with the metal ions generate a diffuse scattering of electrons, which implies that electrons are incident to crystal planes from all different types of directions. These electrons are diffracted at crystal planes within the probed volume, according to Bragg's law (3.1).

$$2d\sin\vartheta_a = n\lambda \qquad (3.1)$$

Where

- d is the spacing between the crystallographic planes
- ϑ_a is the angle between the incident beam and the scattering plane
- n is an integer
- λ is the wavelength of the incident beam

The fraction of diffracted backscattered electrons which are able to escape form the specimen surface is maximized by tilting the specimen. The diffraction patterns arise therefore from typically up to 50 nm depth from the specimen surface [6]. The trajectory of the backscattered electrons produce two diffraction cones on either site of the diffracting set of planes, called Kossel cones. The very low wavelengths of electrons causes the opening angle of these diffraction cones to be near to 90°, and hence the intersection of a pair of diffraction cones with a plane appears as a set of two nearly parallel straight lines. These sets of straight lines or bands formed on the phosphor screen, and captured by a charge coupled device (CCD) camera are called electron backscattered patterns (EBSP). These patterns are also known as Kikuchi diffraction patterns. From these patterns, information on the specimen's crystallographic phase, specific crystallographic orientation (up to 1° angular precision [7], crystalline lattice distortion (image quality (IQ)) and some additional parameters concerning the accuracy of the measurements (e.g. confidence index (CI)) is gathered.

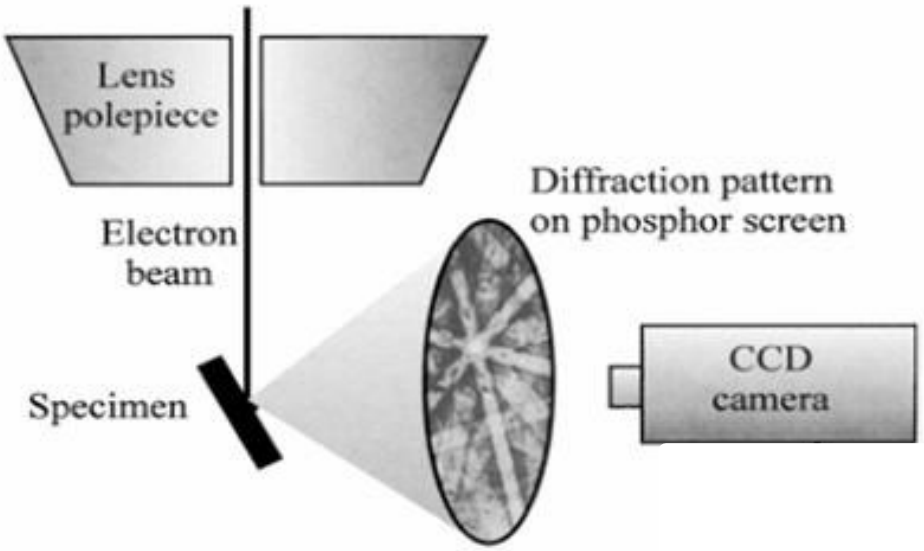

Figure 3-3: Schematic diagram of a typical EBSD setup [8].

3.3.2.2 Data processing and analysis

One of the most widely used programs for automated collection and processing of Kikuchi diffraction patterns is the Orientation Imaging Microscopy (OIM) software program from EDAX-TSL®. In this program, as the electron beam scans the sample, the Kikuchi diffraction patterns are collected and analyzed step by step. This implies that the crystal structure is selected from a set of pre-defined possibilities, the pattern is indexed and the orientation is calculated.

One of the most revealing ways to represent the data is the orientation map (sometimes called an orientation imaging micrograph), which is a description of an area of the microstructure in terms of its crystallographic constituents. In figure 3-4 an orientation map of the cast Cu is given where the different crystallographic orientations are represented according to a certain color code.

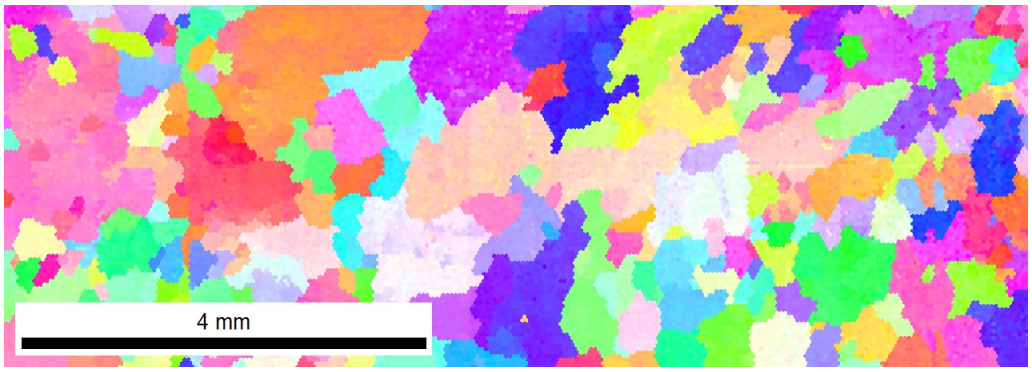

Figure 3-4: Orientation map of the cast Cu sample.

- IPF map

The most used orientation map in this doctoral thesis is the inverse pole figure (IPF) map. The inverse pole figure shows how the selected direction in the sample reference frame is distributed in the reference frame of the crystal. For example, the normal direction inverse pole figure map (Fig. 3-5a) displays which crystallographic directions in the polycrystalline sample are parallel to the normal direction.

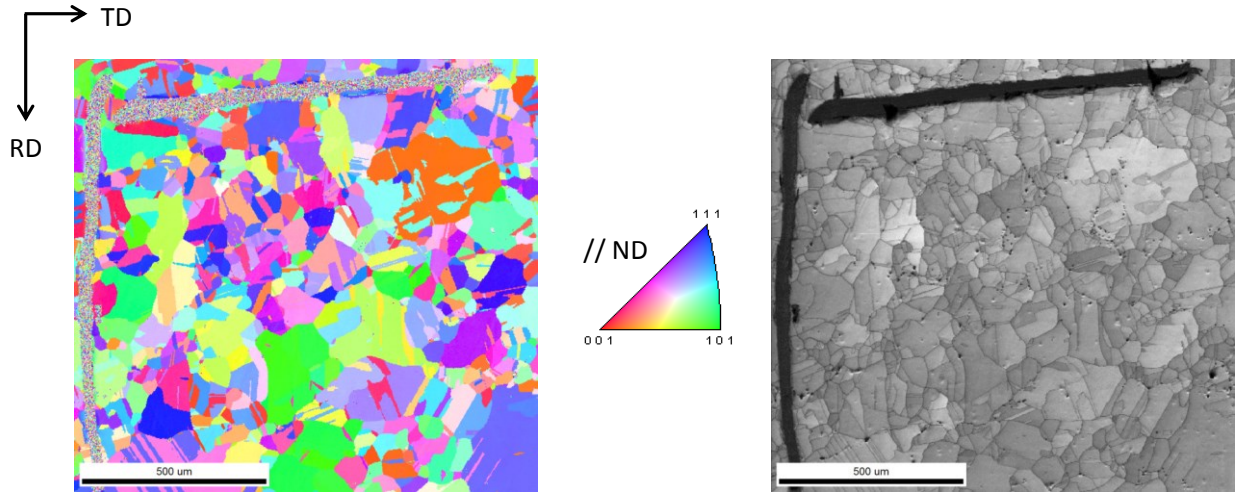

Figure 3-5: (a) IPF map and (b) IQ map of a hot rolled and annealed Cu sample, with scratch.

- IQ map

The image quality parameter or IQ describes the sharpness contrast of the Kikuchi diffraction pattern. The IQ is dependent on the material itself and its condition, so it is not an absolute value, but a function of the parameters used to index the pattern as well as other factors such as sample preparation and video processing. From a materials science standpoint, the most interesting factor affecting the quality of the diffraction pattern is the perfection of the crystal lattice in the diffracting volume. This means that any distortion to the crystal lattice, like the presence of grain boundaries and precipitates or strain [9], will produce lower quality diffraction patterns. Darker shades in the IQ map denote lower IQ values.

When looking at the IQ map in figure 3-5b, the grain boundaries are clearly seen. This is because, when the electron beam is situated near a grain boundary, the diffraction volume may contain both crystal lattices separated by the boundary. In this way, the diffraction pattern will be composed of a mix of both patterns leading to a lower image quality. Also scratches are easily detected in an IQ map as can be seen in figure 3-5b.

- Grain boundary map

Data from EBSD orientation maps can also been used to characterize the grain boundary misorientation distributions. Figure 3-6 is an example of an IQ map with on top of that the grain boundary information of a Cu sample. In black the random high angle boundaries (>15°) are depicted. White boundaries indicate the ∑3 boundaries, which are characterized by a crystallographic misorientation of <111>60°. These ∑3 boundaries may be associated with special properties, as for instance increased corrosion resistance.

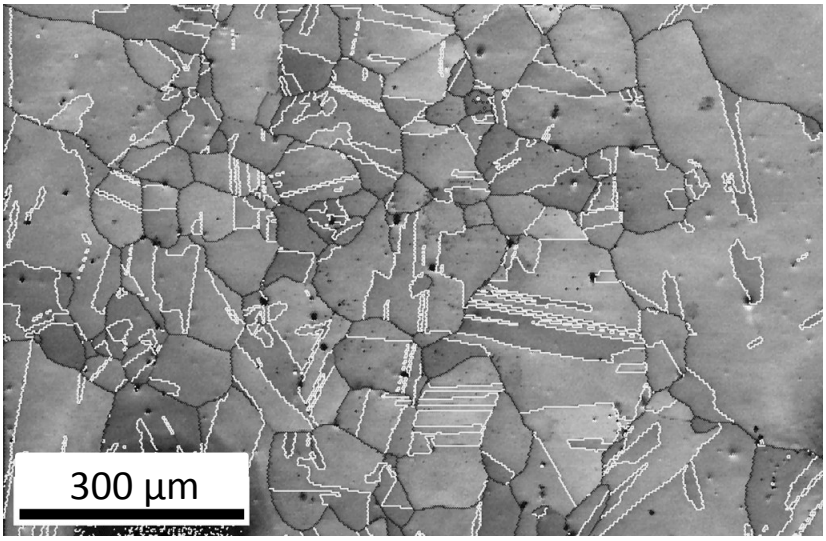

Figure 3-6: IQ map of a hot rolled and annealed Cu sample. Black lines denote random high angle boundaries (>15°) and white lines are ∑3 boundaries.

- Microtexture

With the EBSD technique it is also possible to measure the microtexture of a polycrystalline material [10]. Microtexture is the spatially specific texture measured on an individual orientation basis.

In this work, the automated crystal mapping is executed by the EDAX-TSL® system, which was attached to an FEI® Field Emission (FE)-SEM operated at 20 kV, with a specimen tilt of 70°.

3.3.3 X-Ray Diffraction

With the X-ray diffraction (XRD) technique, the macrotexture can be determined. It is a macroscopic technique with a large beam-material interaction volume, whereby no information is available regarding the locations of the crystals that give rise to X-ray reflections.

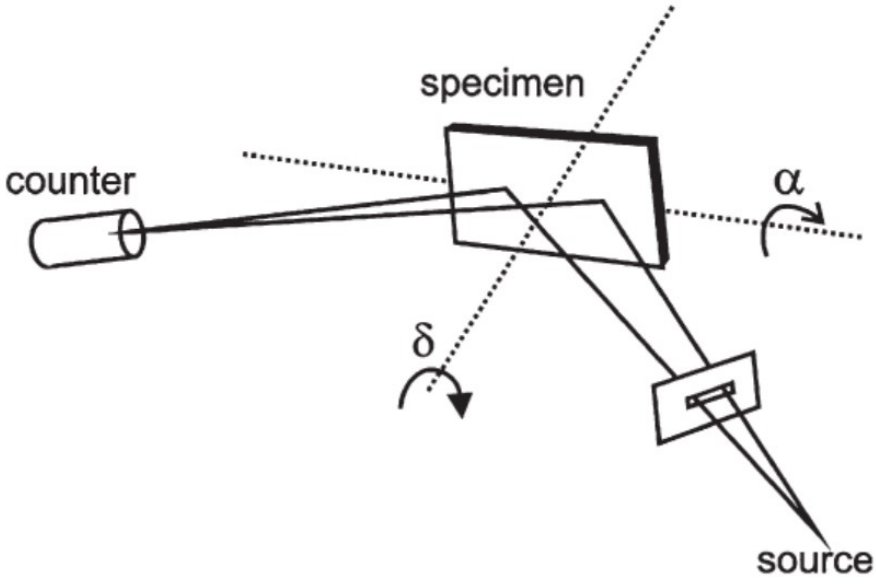

Figure 3-7: The reflection method for pole figure determination [11]

The most commonly used XRD technique is the one developed by Schulz in 1949 [12]. During such measurement, the specimen is mounted in a two-circle goniometer (Fig. 3-7). This goniometer permits simultaneously, a rotation over an angle, δ, around the sample normal and a rotation, α, about the orthogonal axis to the plane defined by the sample normal and the diffraction vector, which is parallel to the bisector of incident and diffracted beams. The incident and diffracted beams, which are restricted by a series of slits, are set at the appropriate Bragg angles for diffraction from the selected plane. The intensity of the diffracted beam is measured by normal counting methods and normalized to that obtained from a randomly oriented specimen. Because of the defocussing effects that develop as α approaches 90°, this technique

provides incomplete pole figures that extends only to α= 70 – 85° from the center. When an ODF is required, then 3 to 4 pole figures are measured from the sample. The raw data is used to derive a pole distribution function, $p_{(hkl)}$, for a particular diffracting plane (hkl). The combination of all possible p values, gives the ODF.

In this work, the pole figures of the Cu samples are determined with the Siemens D5000 diffractometer using Mo Kα radiation. The following (incomplete) pole figures were recorded: (111), (200), (220) and (311). The ODFs were calculated by the classical pole figure inversion method developed by Bunge [13] and improved by the Ghost correction procedure of Van Houtte [15]. For further processing of ODFs, e.g. calculating of volume fractions of given components, the MTM-FHM software by Van Houtte [15] was employed.

3.4 References

1. Strehblow, H.H., V. Maurice and P. Marcus, Initial and later stages of anodic oxide formation on Cu, chemical aspects, structure and electronic properties. Electrochimica Acta, 2001. 46(24-25): p. 3755-3766.

2. Kumar, M., W.E. King and A.J. Schwartz, Modifications to the microstructural topology in f.c.c. materials through thermomechanical processing. Acta Materialia, 2000. 48(9): p. 2081-2091.

3. Kumar, M., A.J. Schwartz and W.E. King, Microstructural evolution during grain boundary engineering of low to medium stacking fault energy fcc materials. Acta Materialia, 2002. 50(10): p. 2599-2612.

4. Randle, V. and M. Coleman, A study of low-strain and medium-strain grain boundary engineering. Acta Materialia, 2009. 57(11): p. 3410-3421.

5. Pourbaix, M., Atlas of electrochemical equilibria in aqueous solutions. 1974: National Association of Corrosion Engineers.

6. Randle, V., Electron backscatter diffraction: Strategies for reliable data acquisition and processing. Materials Characterization, 2009. 60(9): p. 913-922.

7. El-Dasher, B.S., B.L. Adams and A.D. Rollett, Viewpoint: experimental recovery of geometrically necessary dislocation density in polycrystals. Scripta Materialia, 2003. 48(2): p. 141-145.

8. Humphreys, F.J., Review - Grain and subgrain characterisation by electron backscatter diffraction. Journal of Materials Science, 2001. 36(16): p. 3833-3854.

9. Wardle, S.T., L.S. Lin, A. Cetel and B.L. Adams, Orientation imaging microscopy - monitoring residual stress profiles in single crystals using an image-quality parameter, iq, in Fifty-Second Annual Meeting - Microscopy Society of America/Twenty-Ninth Annual Meeting - Microbeam Analysis Society, Proceedings, G.W. Bailey and A.J. GarrattReed, Editors. 1994. p. 680-681.

10. Dingley, D.J. and V. Randle, Microtexture determination by electron back-scatter diffraction. Journal of Materials Science, 1992. 27(17): p. 4545-4566.

11. Humphreys, F.J. and M. Hatherly, Recrystallization and Related Annealing Phenomena. 2004, Oxford: Elsevier Ltd.

12. Schulz, L.G., A direct method of determining preferred orientation of a flat reflection sample using a Geiger counter X-ray spectrometer. Journal of Applied Physics, 1949. 20: p. 1030-1033.

13. Bunge, H.J., Texture analysis in Materials Science. 1982, London: Butterworths.

14. Vanhoutte, P., A method for the generation of various ghost correction algorithms - the example of the positivity method and the exponential method. Textures and Microstructures, 1991. 13(4): p. 199-212.

15. Van Houtte, P., MTM-FHM Software version (second ed.). 1995: MTM-KU Leuven.

Chapter 4
Microstructural evolution of high purity copper during thermomechanical processing[1]

4.1 Introduction

The microstructural features such as texture, grain size and grain boundary orientation are controlled by the specific features of the thermomechanical manufacturing process (TMP) of the material under consideration. In this chapter it is the objective to vary a number of microstructural state variables of the high purity copper in a controlled way. The variation in microstructure is needed because each electrochemical technique requires a specific microstructure in terms of grain size, grain boundary type, shape, etc. For instance, the grain size of the sample has to be compatible with the resolution of the local electrochemical technique used. First of all the standard TMPs are presented, which include hot rolling, room temperature (RT) rolling and annealing. Their effect on the microstructure of the high purity Cu will be discussed. In order to develop a fully recrystallized material with a very small grain size and random texture, as required for a sample that will be investigated with scanning tunneling microscopy (chapter 7), a somewhat unconventional TMP has to be introduced, namely *cryogenic* rolling. In the last part of this chapter, the influence of cryogenic rolling on both the texture and microstructure will be discussed. This will be done by comparing cryogenically rolled copper with room temperature rolled copper.

4.2 Typical texture evolution in FCC metals

The orientation changes that take place during deformation are not random. They are a consequence of the fact that deformation occurs on the most favorable oriented slip or twinning system, and therefore, the deformed metal possesses a preferred orientation or texture. If after deformation recrystallization takes place, nucleation occurs preferentially in association with specific features of the microstructure, i.e. recrystallization starts in regions of particular interest. Also the growth of the nucleus is affected by the orientations of adjacent regions in the microstructure. These two features, nucleation and growth, ensure that a preferred orientation develops in the recrystallized metal. These textures are called recrystallization textures to distinguish them from the related but quite different deformation textures from which they develop.

[1] Part of this chapter is based on the following publication: L. Lapeire, J. Sidor, P. Verleysen, K. Verbeken, I. De Graeve, H. Terryn, L. Kestens, Texture comparison between room temperature rolled and cryogenically rolled pure copper, Acta Materialia, *submitted*.

The deformation texture of fcc metals are determined primarily by the stacking fault energy (SFE) (γ_{SFE}). The stacking fault energy, which is a function of the chemical composition of the material, determines the extent to which unit dislocations dissociate into partial dislocations. As a rule of thumb it can be said that the higher the alloy content the lower the SFE, which is typically illustrated by a metal such as brass of which the SFE energy reaches a minimum exactly at the binary composition of 50 at.% Cu and 50 at.% Zn. When the SFE is high, the dissociation of a perfect dislocation in two partials is unlikely and the material deforms only by dislocation glide. Lower SFE materials display wider stacking faults zones and have more difficulties for cross-slip and climb, such materials are more prone to deformation by twinning. Textures of metals with high SFE are referred to as metals with a pure metal texture, whereas materials with a low value of γ_{SFE} are commonly addressed as metals with a Brass type or alloy type of texture. Pure copper has a SFE of ~80 mJm^{-2} and is considered a material with medium stacking fault energy, where dislocation glide is the deformation mode.

The typical texture components observed in rolled fcc metals as copper are shown in table 4.1 and displayed in the ODF sections (with ϕ_2= 0°, 45° and 65°) of figure 4-1.

Component	**{hkl}**	**<uvw>**	φ_1	φ	φ_2
Copper (C)	112	111	90	35	45
S	123	364	59	37	63
Goss (G)	011	100	0	45	90
Brass (B)	011	211	35	45	90
Dillamore (D)	4 4 11	11 11 8	90	27	45
Cube	001	100	0	0	0

Table 4.1: Main texture components in rolled fcc metals [1].

Conventionally, the rolling textures in fcc metals are described in terms of two fibers being the α-fiber with <110>// ND (Fig. 4-2) and the β-fiber, which connects the Copper ({112} <111>) and Brass ({110} <112>) orientations via the S ({123} <364>), the {325} <10 15 12> and the {314} <596> component [2]. The major difference between the β-fiber and other fibers commonly observed in metals is that there is no common crystallographic plane or direction of orientations characterizing the β-fiber, although the fiber can be approximately described by the following expression (4.1) [2]:

$$\{h,\ 1,\ h+1\} = \langle \frac{h(h+1)}{\frac{3}{4}-h}, \frac{2h(h+1)}{\frac{1}{2}-h}, \frac{h^2}{h-3/4} + \frac{2h}{h-1/2} \rangle \qquad (4.1)$$

A schematic representation of the α- and β- fibers is given in the three dimensional Euler angle space in figure 4-2.

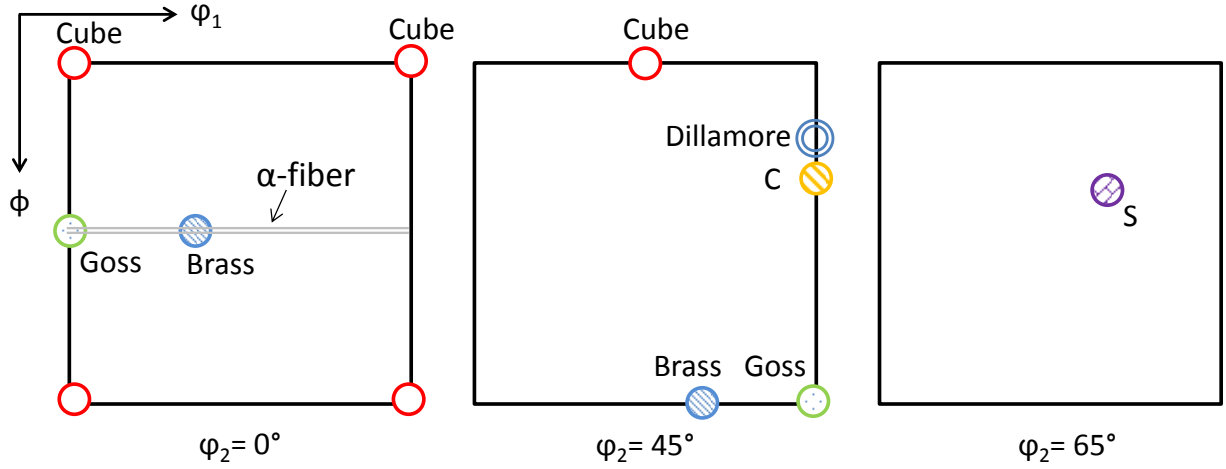

Figure 4-1: ODF sections (with φ_2= 0°, 45° and 65°) of the main texture components in rolled fcc metals.

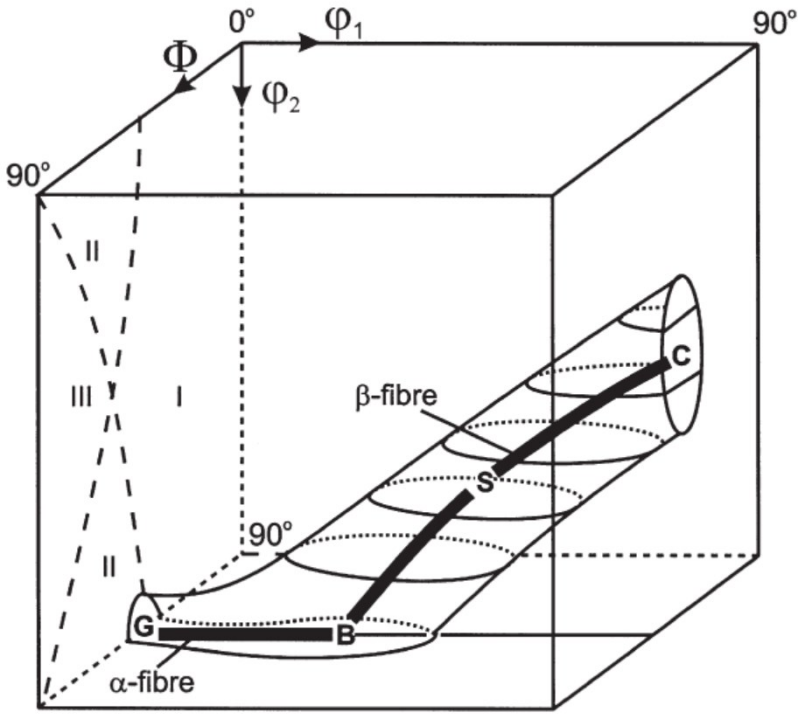

Figure 4-2: Schematic representation of the fcc rolling texture in first subspace of 3D Euler angle space [3].

After recrystallization of a heavily deformed fcc material of medium to high SFE, the texture consists of a strong cube component. This strong cube texture in copper can be eliminated by adding quite small amounts of alloying elements. These alloying elements are believed to reduce the SFE and therefore change the deformation and subsequent annealing textures. Besides the cube component, other textural components can be found in the recrystallization texture of fcc metals. In many cases the origin of the different components is still a matter of debate. The possible recrystallization components in fcc metals are listed in table 4.2 and displayed in the ODF sections (with φ_2= 0°, 45° and 65°) of figure 4-3. The Goss {011}<100>, Q {013}<231> and perhaps the P {011}<122> and R {124}<211> components are believed to be associated with nucleation at shear bands.

Component	{hkl}	<uvw>	φ_1	φ	φ_2
Cube	001	100	0	0	0
Goss (G)	011	100	0	45	0
S	123	634	59	37	63
P	011	122	70	45	0
Q	013	231	58	18	0
R	124	211	57	29	63

Table 4.2: Components of recrystallization textures in fcc metals [1].

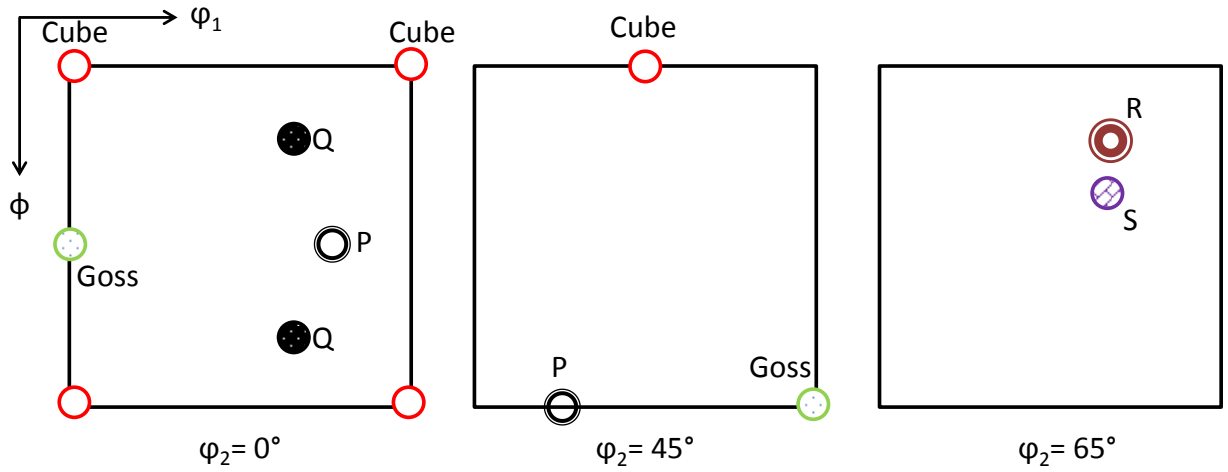

Figure 4-3: ODF sections (with φ_2= 0°, 45° and 65°) of the main texture components in recrystallized fcc metals.

4.3 High purity copper

4.3.1 Cast

The initial material in this dissertation is high purity cast copper, obtained from Aurubis© (Belgium). During the casting process, the crystals grow and form open, tree like structures called dendrites. Figure 4-4a displays the inverse pole figure (IPF) map of the cast copper. The texture of this material is almost random, which implies that no preferred orientation is present in the cast structure. The mean grain size is 343 µm and almost no ∑3 and ∑9 boundaries are observed (a total length fraction of 0.3%). To wipe out the features of the as-cast microstructure, like the dendritic structure and the very large grains, a hot rolling step is necessary.

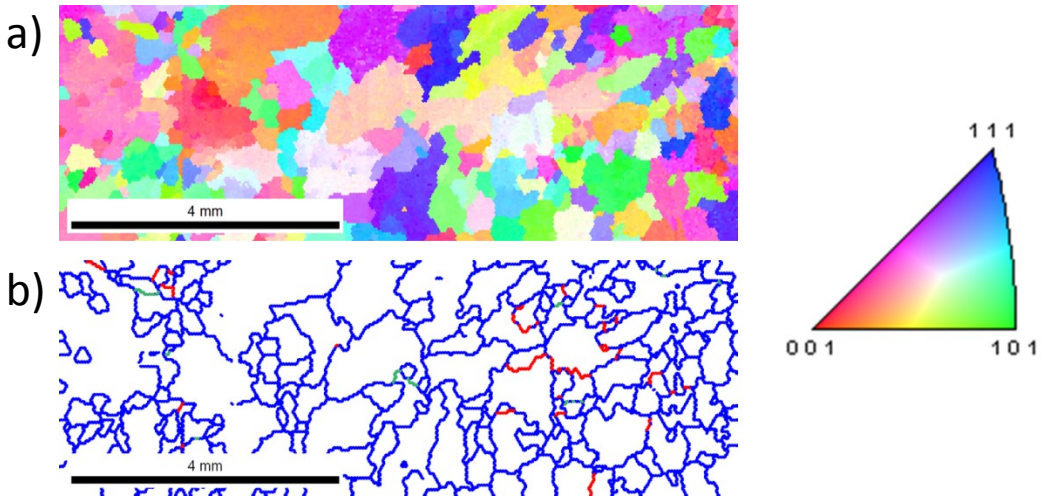

Figure 4-4: (a) IPF map and (b) grain boundary map of the cast high purity copper. High angle boundaries, ∑3 boundaries and ∑9 boundaries are depicted by blue, red and green lines respectively.

4.3.2 Hot rolling

Rolling is a metal forming process in which the metal is passed through one (or more) pairs of rolls to reduce the sheet thickness. Classification of the rolling process is done based on the temperature of the metal rolled. If the temperature of the metal is above the recrystallization temperature, the process is called hot rolling. Conversely, if the metal temperature is below its recrystallization temperature, the process is termed cold or room temperature rolling.

In this dissertation, a 75% hot rolling reduction at 350°C was applied. This hot rolling allowed destroying the cast microstructure and produced a completely recrystallized microstructure. The sheet thickness was reduced from 24.9 mm to 6.4 mm.

After hot rolling the texture and microstructure was evaluated in the mid-thickness section of the sheet. A completely recrystallized microstructure is observed with an average grain size of 14 µm and with 12% of ∑3 boundaries by length fraction. The texture (Fig. 4-5) exhibits a near random distribution of orientations with an absolute maximum of 2.4 x random. This texture is the initial texture for both the RT rolled as the cryogenic rolled material.

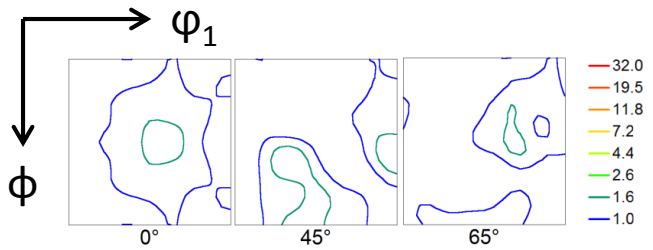

Figure 4-5: ODF sections (with φ_2= 0°, 45°, 65°) of the mid-thickness of the copper sample prior to subsequent rolling.

4.3.3 Room temperature rolling

The starting material for the room temperature (RT) rolling process is the hot rolled material (6.4 mm thickness). The multi-pass unidirectional RT rolling was carried out in a two-roll mill of which the cylinders were oil lubricated. Different reductions of respectively 17%, 42%, 61%, 80% and 92% were carried out corresponding to true logarithmic strains of 0.19, 0.55, 0.94, 1.59, 2.08 and 2.55, respectively.

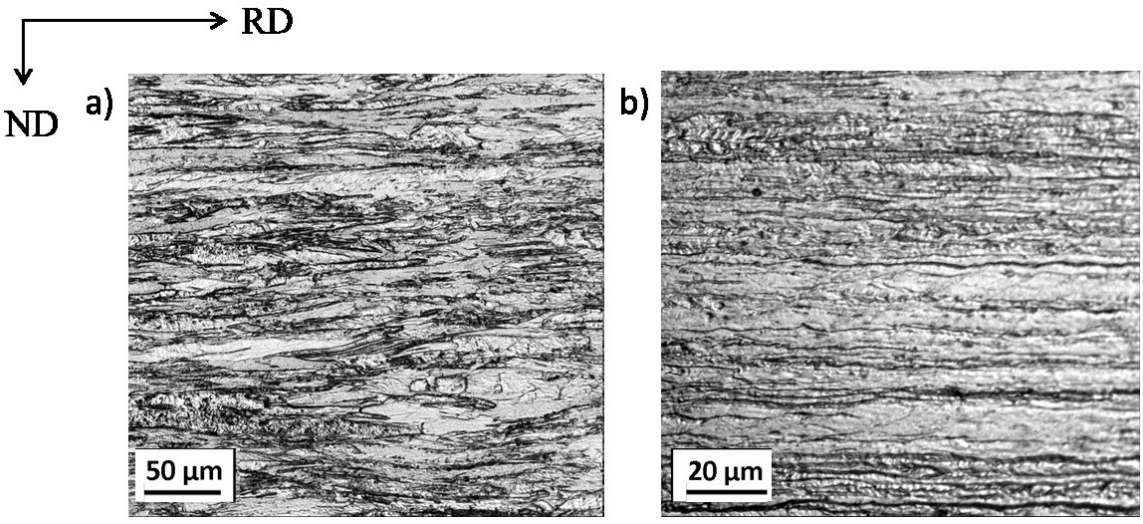

Figure 4-6: Optical micrographs of high purity copper after RT rolling (a) 61% and (b) 92% (etchant: 1:1 H_2O_2: NH_4OH).

After RT rolling all grains possess a so-called pancaked shape, implying that all grains are elongated along the rolling direction (Fig. 4-6) and compressed along the normal direction in order to accommodate for the macroscopically imposed strain field.

Figure 4-7 shows the orientation density values along the α- (<011>// ND) (Fig. 4-7a), the τ- (<011>// TD) (Fig 4-7b) and the β-fiber (Fig. 4-7c) for RT rolled copper. For low reductions the variation of intensity along the fibers is small with values of 2-4 times random. The homogeneity along the α- and the τ-fiber deteriorates as rolling continues. The brass component (α-fiber) and the copper component (τ-fiber) strengthen and become the major component in heavily RT rolled high purity copper. The β-fiber is becoming more and more prominent as rolling continues.

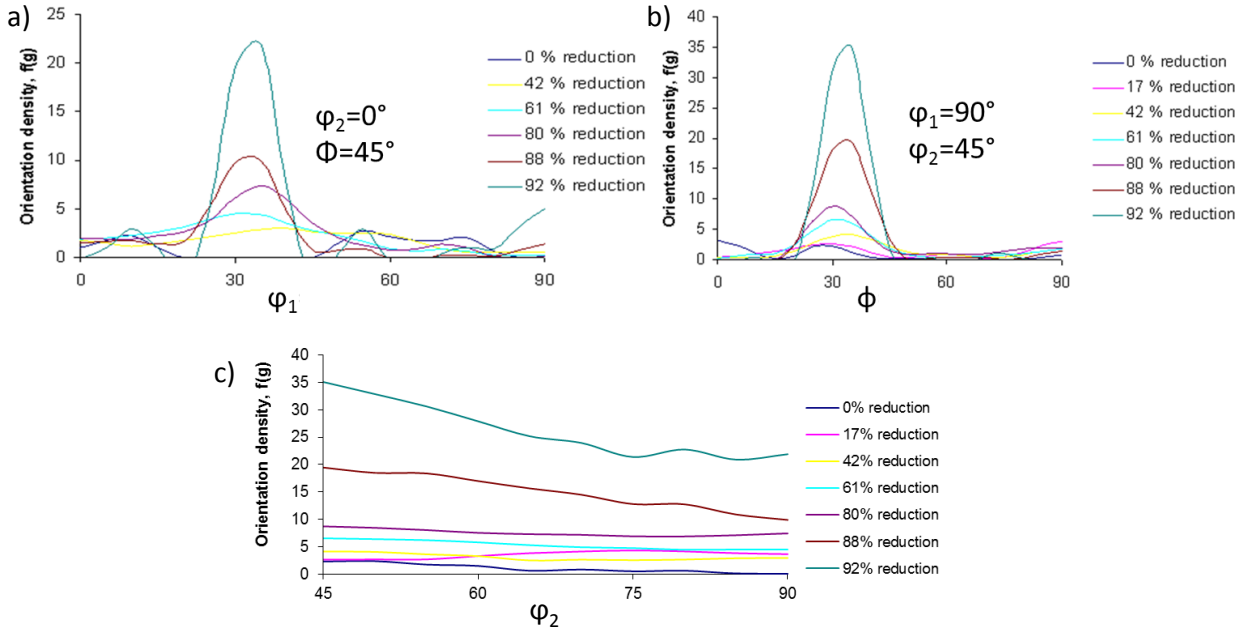

Figure 4-7: Orientation density f(g) along the major fibers in RT rolled high purity copper rolled to different reductions with (a) α-fiber, (b) τ-fiber and (c) β-fiber.

4.3.4 Annealing

Annealing is a heat treatment applied to products during and after rolling. There are three stages of the annealing process that sequentially can occur as the temperature of the material is raised. The first stage is recovery, which results in softening of the metal through removal of excess dislocations and the internal stresses they cause. Recovery occurs at the lower temperature stage of all annealing processes and it is essentially a process of elimination and

reconfiguration of dislocation structures. Grain size and shape do not change in the recovery process. In the second stage, called primary recrystallization, new strain-free grains nucleate in the deformed matrix structure and these nuclei grow to replace the deformed grains. If the annealing is allowed to continue after the completion of recrystallization, normal or abnormal grain growth may occur, which represents the third stage of the series of thermally activated softening processes.

All RT rolled samples underwent four different annealing treatments. In this way, different textures and variation in grain size and amount of CSL boundaries are obtained. The four different annealing treatments are:

- 60 s, 250°C, salt bath
- 20 min, 250°C, salt bath
- 1 h, 250°C, salt bath
- 8 h, 500°C, oven

After the annealing treatment, all samples were quenched in water.

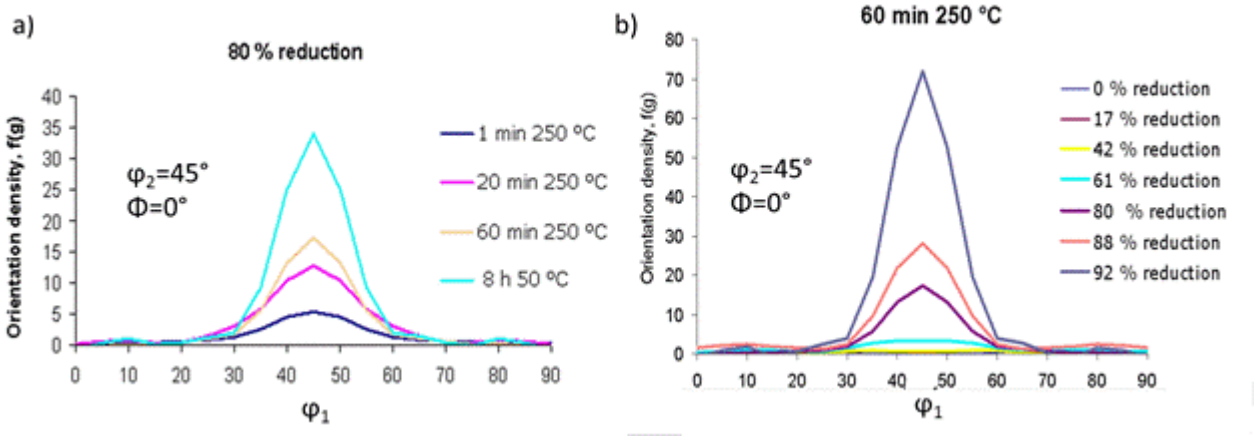

Figure 4-8: Representation of the ϑ-fiber. (a) Intensity of the ϑ-fiber of 80% RT rolled copper after different annealing treatments. (b) Intensity of the ϑ-fiber after annealing at 250°C step during 60 min, for different RT rolling reductions.

The intensities along the θ-fiber (<001>// ND) for different annealing treatments and different RT rolling reductions are represented in figure 4-8. In this figure it is seen that, for the same RT rolling reduction, the cube component becomes stronger as the annealing time and annealing temperatures are increased. The behavior after 80% rolling reduction is representative for the other rolling reductions. In figure 4-8b the intensity of the θ-fiber is represented for the same

annealing treatment (60 min, 250°C), but for different RT rolling reductions. This shows that the cube component is getting more pronounced as the rolling reduction increases.

By changing the annealing treatment, not only changes in texture can be observed, but also the amount of CSL boundaries can be affected (Fig. 4-9). Longer and higher annealing times give rise to higher length fraction of ∑3 and ∑9 grain boundaries. In figure 4-10 the mean grain size as a function of the different annealing treatments is depicted for 61% RT rolled copper. This figure shows that the mean grain size remains almost constant up to 60 min annealing. Only at longer annealing times a noticeable increase in grain size is observed.

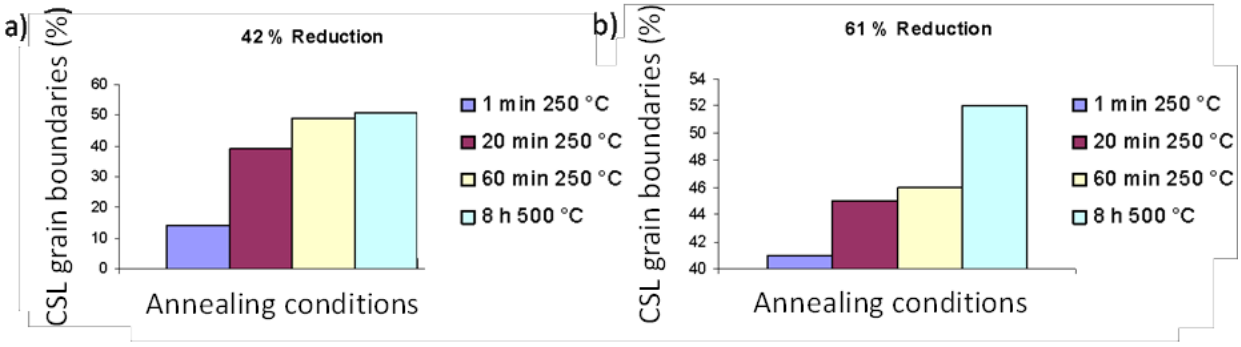

Figure 4-9: Length fraction of CSL grain boundaries (∑3 and ∑9) as a function of the different annealing treatments. (a) 42% RT rolled copper and (b) 61% RT rolled copper.

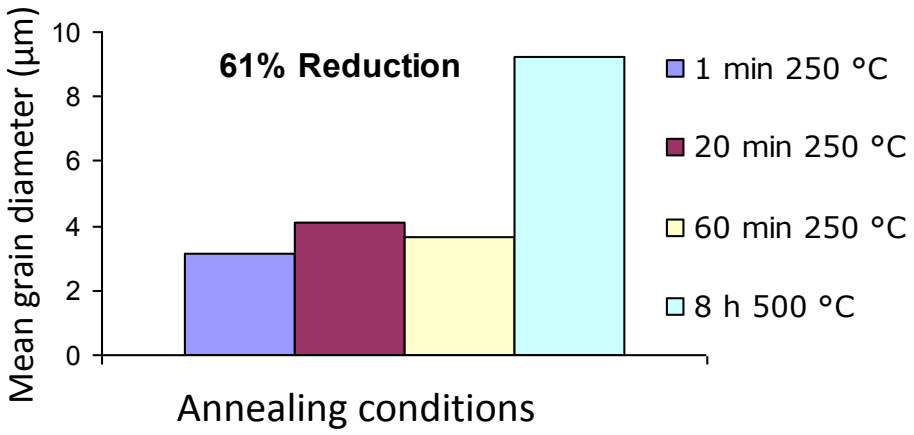

Figure 4-10: Mean grain diameter as a function of the different annealing conditions for 61% RT rolled copper.

4.4 Cryogenic rolling

For the electrochemical scanning tunneling microscope (EC-STM) measurements reported in chapter 7, a material with a very small grain size and a random texture is needed. To this purpose, cryogenic rolling will be conducted. In the last part of this chapter on the microstructural evolution of pure copper during TMP, the influence of cryogenic rolling on the texture and the microstructure of pure copper is investigated by electron backscatter diffraction (EBSD), both in the deformed and the annealed state. This is done by comparing cryogenically rolled copper with room temperature rolled copper, rolled to the same thickness reductions.

4.4.1 Introduction

Nowadays, there is a considerable renewed interest in the deformation of metals at very low absolute temperatures, which is known as cryogenic deformation [4-8]. The majority of the research published on this topic was performed on aluminum and copper, most likely because of the lower homologous temperatures of these metals. It is assumed that rolling at cryogenic temperature may result in enhanced grain refinement and associated strengthening when compared to rolling at room temperature [9]. It is believed that very low temperatures suppress the processes of dynamic recovery, promote an increase in the dislocation density, activate mechanical (deformation) twinning [5, 10] and thereby promote the formation of extremely fine-grained structures after annealing. It is well established that lowering the stacking fault energy (SFE) and deformation temperature promotes deformation twinning over dislocation slip [1]. Metals with intermediate SFEs, like pure copper, normally deform by dislocation slip during rolling at room temperature [11]. Literature reports remain ambiguous on the occurrence of deformation twinning in pure copper rolled at cryogenic temperatures [5, 10, 12-14].

Another potential effect of cryogenic rolling is the formation of a very weak, almost random texture after annealing in Cu and Al alloys [15, 16]. There is evidence that this can be linked to the occurrence of shear bands in the deformation texture. This was first suggested by Ridha and Hutchinson [15], after observing an almost random texture in copper when shear bands were detected in the deformed microstructure. This was in sharp contrast to the strong cube recrystallization texture observed after annealing of a similar batch of copper but without shear bands in the deformation structure. Shear bands are very potent sites for the nucleation of recrystallization because of their highly localized strain. It is confirmed experimentally that shear bands do indeed act as nucleation sites during annealing of Cu and Al alloys [16-20]. If a sufficient growth capacity of these nucleated grains is assumed, the question arises how nucleation at shear bands can affect the recrystallization texture. Because the nuclei provided by the shear bands have to compete with nuclei formed at other nucleation sites, including cube-bands, second-phase particles and grain boundaries [18].

Only limited information on the detailed influence of nucleation at shear bands on the texture is available in the literature. The most accepted theory is that the impact of nucleation at shear bands on the recrystallization texture is two-fold [15]. At first, the shear bands are known to cut through the cube bands, in this way reducing the nucleation sites available for nucleation of the cube orientation. Secondly, nucleation at shear bands may give rise to the formation of new orientations that are usually not observed in the recrystallization textures of fcc metals. In fcc materials two types of shear bands can develop depending on the SFE of the material. In materials with medium to high SFE Cu-type shear bands are formed, the precursory obstacles are the elongated dislocation walls of a cell block structure. In FCC materials with low SFE energy, where deformation twinning is occurring frequently, brass-type shear bands are formed. In this case the obstacles are fine twin-matrix lamellae [19]. Only limited and sometimes contradictory information on the influence of nucleation at the brass- and Cu-type shear bands on the texture is available in literature. There is some evidence that there may be preferred nucleation of some orientations at the Cu-type shear bands in Al-Mg alloys [16, 18], Al-Cu alloys [21, 22] and commercially pure Al [23]. It is stated [18, 23-25] that peaks around the Goss {011}<100>, Q {013}<231> and perhaps the P {011}<122> and R {124}<211> orientations are associated with nucleation at Cu-type shear bands, since they appear in the recrystallization texture of these materials. In the case of the brass-type shear bands the situation is more complex because of the existence of a second-as deformed component due to the twins within the shear bands [14, 19, 20].

In the last part of this chapter, the aim is to obtain a better understanding of the texture development in the cryogenic rolling process of pure copper. To this purpose, the textures and microstructures of room temperature (RT) rolled and cryogenically rolled material, starting from an identical batch of pure copper, is studied in detail. Also the differences in texture and microstructure between the RT rolled and cryogenically rolled copper after annealing are examined. The texture evolution inside the shear band is modelled using the visco plastic self-consistent (VPSC) model and compared with the experimentally determined shear band texture.

4.4.2 Material processing

The initial material in this study is the hot rolled material presented in section 4.3.2. Part of the initial material is cryogenic rolled to 50%, 75% and 90% overall thickness reductions (true logarithmic strain: 0.7; 1.4 and 2.3). In order to provide cryogenic deformation conditions, the rolling sample is soaked for 10 min in liquid nitrogen prior to each rolling pass. During rolling the temperature is monitored and never exceeded -2°C. After completion of the cryogenic rolling process, specimens are stored at -17°C to avoid extensive recovery or even recrystallization at RT of the cryogenically rolled copper [26]. Subsequently, part of the cryogenically rolled material is soaked in a salt bath at 200°C for 60 s, to the purpose of obtaining a completely

recrystallized small grained microstructure. Other cryogenically rolled material was submitted to a salt bath annealing treatment at 200°C for 180 s.

To compare the texture and microstructure of the cryogenically rolled material with a RT rolled material, another sample of the initial material is RT rolled with the same overall thickness reductions as the cryogenically rolled material. For acquiring a completely recrystallized material, the RT rolled material is annealed for 180 s at 200°C in a salt bath.

The rolling experiment at both room temperature (RT) and at cryogenic temperature was performed on a two-high rolling mill with the roll diameters of 120 mm. The change of contact length to mean thickness ratio (*L/h*), calculated by equation 4.2 is shown in figure 4-11 for the current rolling schedule.

$$\frac{L}{h} = \frac{2\sqrt{R(h_i - h_f)}}{h_i + h_f} \tag{4.2}$$

with R the rolling cylinder radius, h_i and h_f are the initial and final thicknesses, respectively.

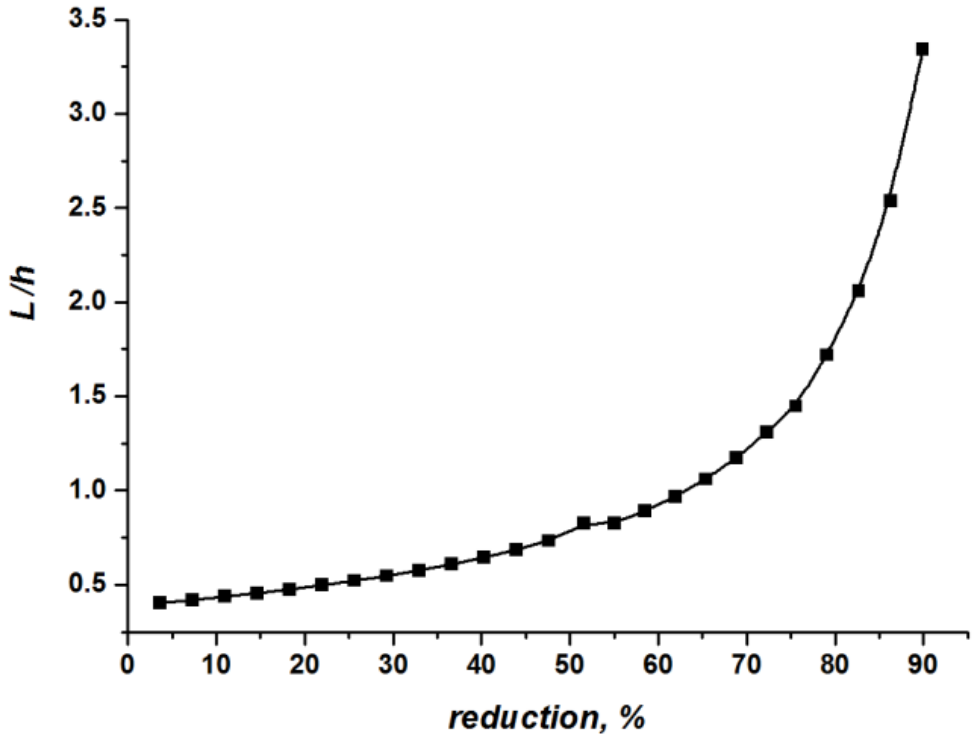

Figure 4-11: Change of contact length to mean thickness ratio as a function of the applied reduction. Every point in the plot corresponds to a sequential rolling pas.

As shown in figure 4-11, the first 50% deformation was performed with small roll draughts, i.e. *L/h* varying from 0.4 to 0.8. From 50% to 75% the material was rolled with the *L/h* ratio changing from 0.8 to 1.4, whereas the rolling reductions between 80% and 90% were applied with rather large roll draughts varying from 2.0 to 3.3. The rolling geometry, as quantified by the *L/h* ratio, accounts for the strain distributions across the thickness. It is well known [27-29] that small roll draughts tend to induce a strong shear deformation gradient across the thickness, while large *L/h* values guarantee a relatively homogenous through-thickness strain distribution, approximating the characteristics of plane strain compression.

Electron backscatter diffraction (EBSD) observations on both the cryogenically and RT rolled copper are made on the longitudinal plane containing the rolling and normal directions. The typical flat-rolling convention is adopted with ND being the normal direction, RD the rolling direction and TD the transverse direction. The textural observations are made on the mid-thickness section of the rolled samples. All textures are represented by orientation distribution functions (ODFs). For simplicity, only three ODF sections (with φ_2 = 0°, 45° and 65°) are shown, in which the fcc rolling and annealing texture components are represented. Figure 4-12 and table 4.3 show the main orientations observed during the different thermomechanical processing steps of pure Cu, both after RT rolling as after cryogenic rolling. For the deformed materials, no specific sample symmetry was assumed.

To obtain a suitable surface preparation for EBSD, the copper is mechanically ground and polished, followed by a finishing electropolishing step (10 V, 10 s) in a phosphoric acid electrolyte. The EBSD system is attached to a Quanta FEI® field emission scanning electron microscope (FE-SEM) operated at 20 kV. Measurements were carried out with a step size depending on the sample grain size, and the orientation data were post-processed with the commercial orientation imaging software OIM-TSL®. For texture analysis, in order to obtain a statistically reliable texture representation, several scans were stitched together with a minimum of 0.36 mm^2 scanned area per sample. A misorientation threshold of 15° was used to differentiate low angle grain boundaries (LAGBs) from high angle grain boundaries (HAGBs). For LAGBs, a lower limit cut-off of 2° was used, i.e. misorientations lower than 2° were considered to exceed the angular resolution of the system. The ∑3 boundary fraction is defined as the length fraction of ∑3 boundaries with respect to the total length of high angle grain boundaries. Since recrystallization at RT is reported for cryogenically deformed copper [26] partitioning between recrystallized and deformed grains is done based on the grain orientation spread (GOS) parameter in the cryogenically rolled samples. This GOS parameter has been used by Konkova et al. [26] for the same purpose. Grain size measurements of the recrystallized materials are made by the linear-intercept method.

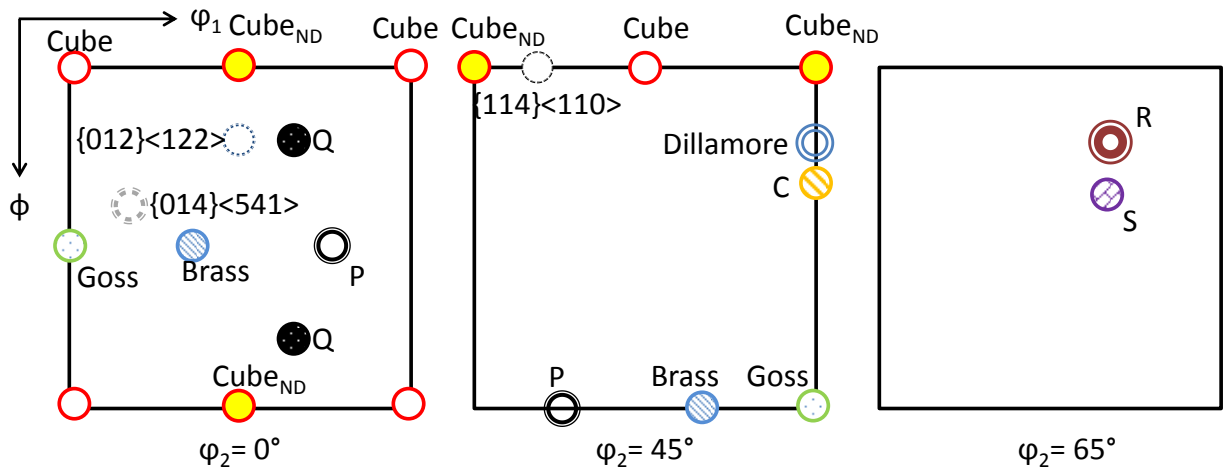

Figure 4-12: ODF sections (with φ_2= 0°, 45° and 65°) of the main texture components observed during thermomechanical processing of pure copper.

Component	{hkl}	<uvw>
Cube	001	100
ND rotated cube ($Cube_{ND}$)	001	110
Copper (C)	112	111
Brass	011	211
Goss (G)	011	100
Dillamore	4 4 11	11 11 8
S	123	634
P	011	122
Q	013	231
R	124	211

Table 4.3: Main texture components observed during thermomechanical processing of pure copper.

4.4.3 Texture comparison between RT rolled and cryogenically rolled pure copper

4.4.3.1 Initial material

A detailed texture analysis of the initial material is given in section 4.3.2. A completely recrystallized microstructure is observed with an average grain size of 14 µm and with 12% of ∑3 boundaries by length fraction. The texture (Fig. 4-5) exhibits a near random distribution of orientations with an absolute maximum of 2.4 x random. This texture is the initial texture for both the RT rolled and the cryogenically rolled material.

4.4.3.2 Deformed material

4.4.3.2.1 Deformed state after 50% deformation

To the purpose of comparing the deformation texture of the RT rolled material with the cryogenically rolled material, a texture analysis was carried out on both materials, rolled to the same overall thickness reductions (50%, 75% and 90%). Figure 4-13a and 4-13b show the rolling textures after 50% reduction at room and at cryogenic temperatures, respectively.

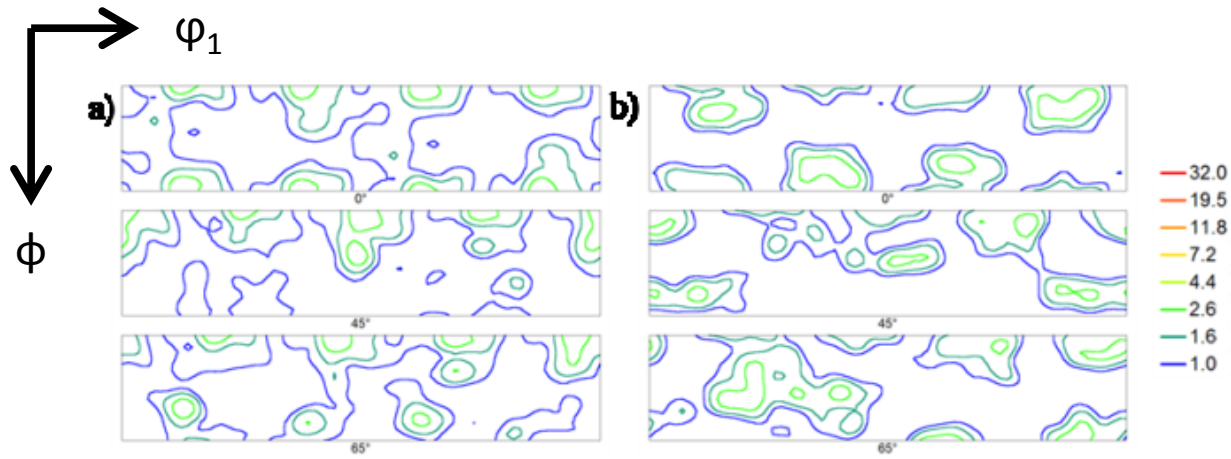

Figure 4-13: ODF sections (with φ_2= 0°, 45°, 65°) of the mid-thickness section after 50% deformation (a) RT rolled, (b) cryogenic rolled.

Although β-fiber textures tend to develop even after small reductions, in the present case, after 50% RT deformation, the texture in the mid-thickness (Fig. 4-13a) remained weak (no peaks higher than 4 x random) and the observed texture was obviously different from the conventional β-fiber. In the 50% RT rolled material the ND-rotated cube component {100} <110> was present, which may be reminiscent of RD-ND shear during rolling. Indeed, rolling with small roll draughts induced extensive shear deformation across the thickness [28, 29], which accounted for the appearance of fcc shear texture components such as the {100} <110> orientation.

After 50% cryogenic reduction (Fig. 4-13b), an equally weak texture was observed in the mid-thickness of the sample, with the same intensity as in the RT rolled sample (4 x random). The same texture component was observed as in the 50% RT rolled material, namely the ND-rotated cube component.

4.4.3.2.2 Deformed state after 75% deformation

In the material RT rolled to 75% reduction, the overall texture intensity was strengthened and both α- and β-fibers appeared in the ODF (Fig. 4-14a). The α-fiber Goss {011} <100> and Brass {011} <211> components were observed, together with the β-fiber copper {112} <111> and S {123} <634> components. The brass component was the most intense, with a maximum intensity of 13.8 x random. Orthorhombic sample symmetry was observed.

After 75% cryogenic rolling (Fig. 4-14b), the rolling texture exhibited some similar features as the conventionally rolled texture, although major differences were observed as well. After cryogenic rolling, the texture exhibited a maximum of 10.6 x random on the Brass component, which is somewhat weaker as compared to the conventionally rolled sample. The orthorhombic symmetry was broken and only monoclinic symmetry was observed. It should be mentioned that recrystallization occurred already to some extent in the 75% cryogenically rolled sample and therefore, to determine the texture of the deformed cryogenically rolled material, partitioning was required between the deformed and the recrystallized grains based on the GOS distribution. Grains with an orientation spread higher than 2° were considered to be deformed.

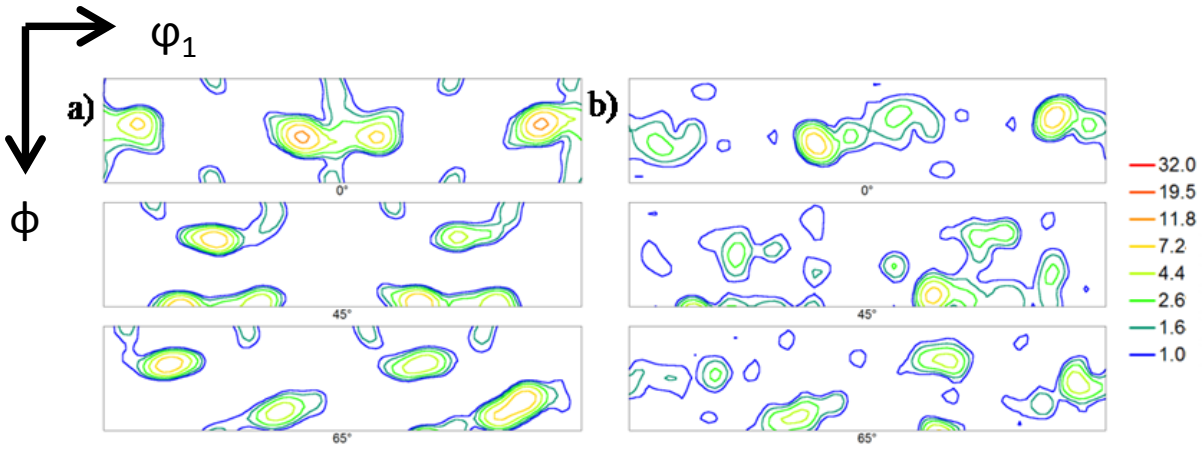

Figure 4-14: ODF sections (with φ_2= 0°, 45°, 65°) of the mid-thickness section after 75% deformation (a) RT, (b) cryogenic.

Figure 4-15 shows the image quality (IQ) maps of the RT rolled (a) and cryogenically rolled (b) copper after 75% deformation. Although the deformation texture of these two materials was quite similar, a large difference was observed in their microstructures. In the cryogenically rolled material, in contrast to the RT rolled material, numerous macro shear bands (SBs) were

observed. These bands form thin planar sheets that were inclined at ~35° to the RD. A secondary minor set of SBs were observed at an inclination angle of ~20° to RD. It is assumed that SBs are formed as the result of a plastic instability, which energetically favors plastic deformation in a restricted volume of the material [17, 30-32]. At certain places these SBs seemed to form an array of rhomboidal prisms with axis parallel to the transverse direction (Fig. 4-15b). These SBs were believed to be associated with metals that have partially deformed by twinning, so these SBs most probably are brass-type of SBs [3, 17].

Since SBs largely affect the stored energy distribution, they may have a strong impact on the recrystallization behavior, and in many cases SBs act as preferred nucleation sites [16-20]. Ample evidence exists that preferred nucleation of certain orientations occurs at SBs [16, 18, 21]. In the present case, this was verified by analyzing the EBSD scans collected on the cryogenically rolled sample.

In the grain orientation spread map (Fig. 4-16a), grains with an orientation spread lower than 2° were colored white (step size EBSD measurement: 0.06 μm). Since recrystallized grains usually show an orientation spread of less than 2° it is believed that all white grains were recrystallized. When comparing the IQ map (Fig. 4-15b) with the GOS map (Fig. 4-16a), it is clearly seen that all recrystallized grains are located inside the SBs. The low IQ inside the SBs was assigned to its high stored energy and the very small grain size of the recrystallized grains. In figure 4-16b the IQ map is shown concurrently with the main texture components observed inside the SBs with a tolerance of 10° from the ideal orientation. It is obvious that the texture inside the SBs was not random, but certain orientations were dominant. The main orientations are the following: β-fiber components (with Brass {011} <211>, {718} <26 50 29> and {314} <596>), {15 12 7} <6 11 6>, {014} <541>, {114} <110>, R {124} <211>, Q {013} <213> and the Goss component {011} <100>. Also the shear {001 } <110> component (ND rotated cube) was observed. No traces of the P component {011} <122>, a component frequently associated with nucleation at SBs, were found.

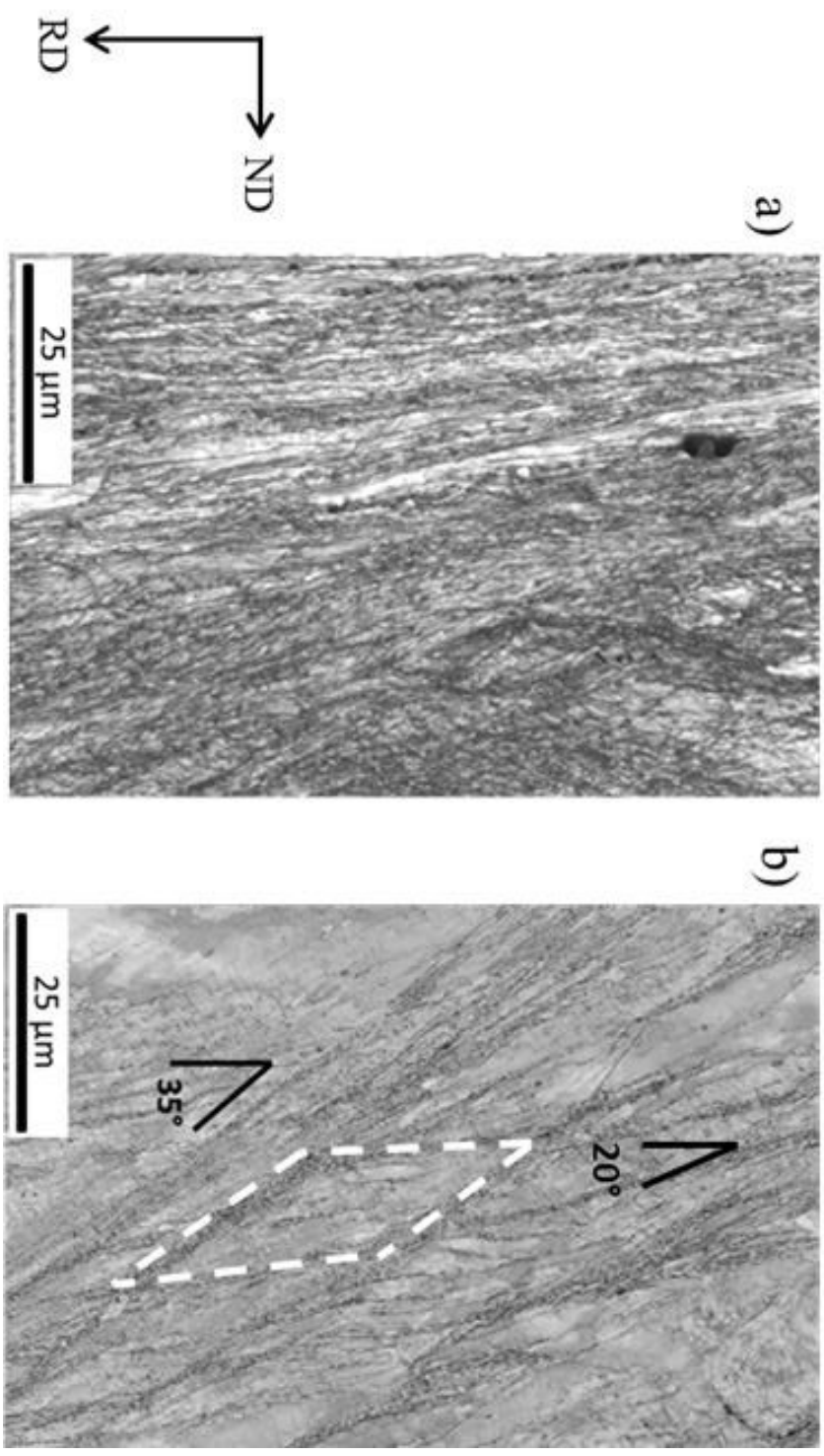

Figure 4-15: Image Quality (IQ) map of the mid-thickness section after 75% deformation (a) RT, (b) cryogenic rolled.

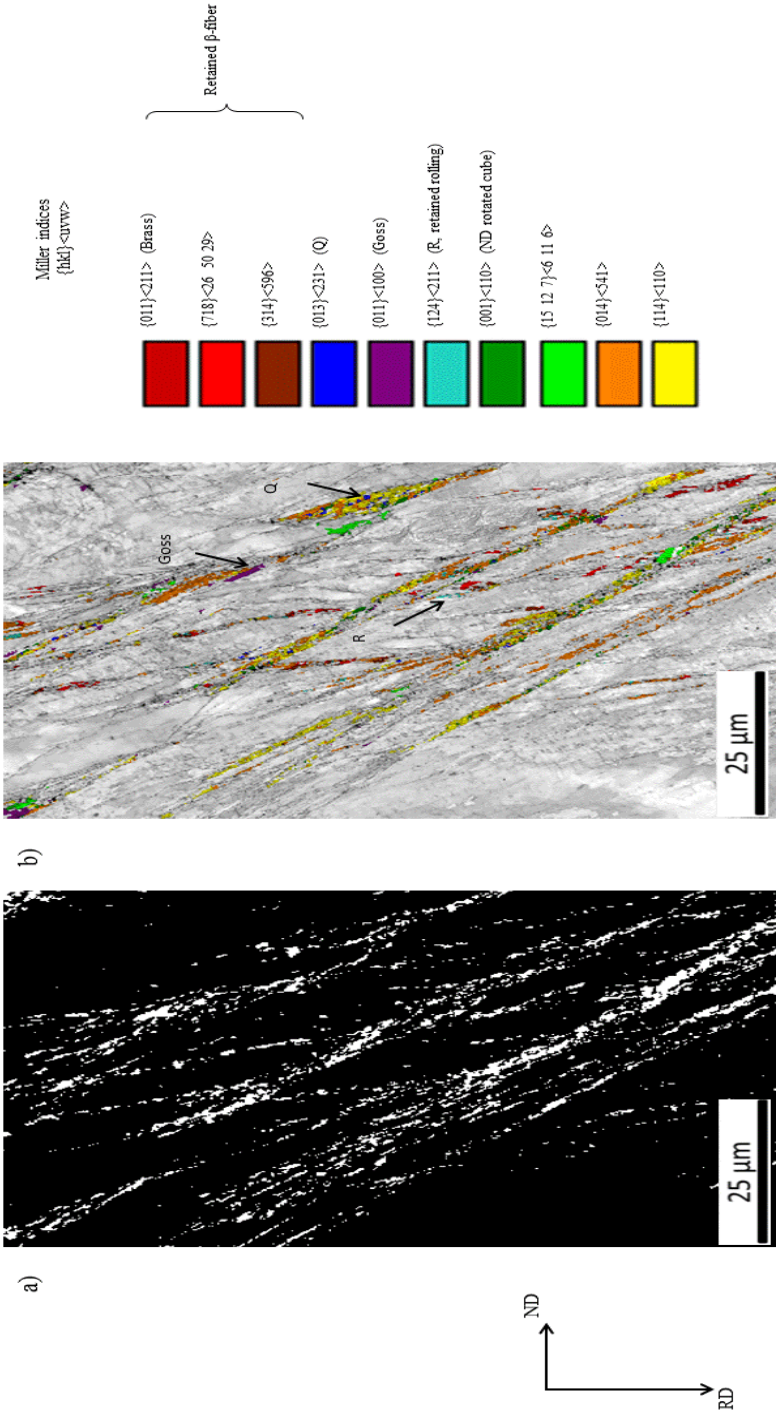

Figure 4-16: EBSD maps of the mid-thickness section after 75% cryogenic deformation. (a) Grain orientation spread (GOS) map, grains with an orientation spread lower or higher than 2° are colored white and black, respectively. (b) IQ map with indication of the main texture components found inside the shear bands.

The ODF of figure 4-17 is composed by considering all the dominant SB orientations, identified in figure 4-16b, with equal weights ignoring the true experimentally observed volume fractions. This procedure was applied to level out statistical noise in the experimental data, given the relatively few SB grains that were observed. We assume in this work that the ODF of figure 4-17, which is derived from recrystallized SB orientations, is also representative for the texture before recrystallization.

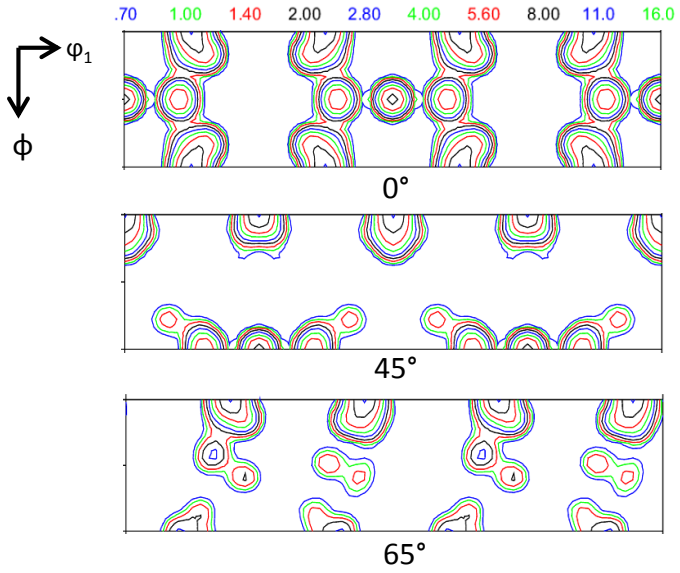

Figure 4-17: ODF sections (with φ_2= 0°, 45°, 65°) of the dominant grains with GOS < 2° located inside the SBs of the 75% cryogenically deformed copper sample, assuming equal weights for each observed orientation.

4.4.3.2.3 Deformed state after 90% deformation

Both RT and cryogenically rolled textures exhibited orthorhombic symmetry, which corresponded to the symmetry associated with plane strain compression. After 90% reduction, at RT the texture became much sharper (Fig. 4-18a), with the strongest peak of 19 x random on the Brass component. The intensity distribution along the α-fiber became more heterogeneous and developed into the single brass component, although, the β-fiber remained present. Another remarkable observation is that there seems to be a mild strengthening of the cube component compared to the 75% RT rolled sample.

As almost half of the area of the 90% cryogenically rolled copper was already recrystallized, due to room temperature annealing [26], partitioning based on the GOS parameter was needed to determine the residual deformation texture. The texture of the remaining deformed grains after 90% cryogenic rolling is represented in figure 4-18b. The same texture components were observed as in the RT rolled copper, although no weakening of the α-fiber was observed. It was thought that this can be due to deformation twinning.

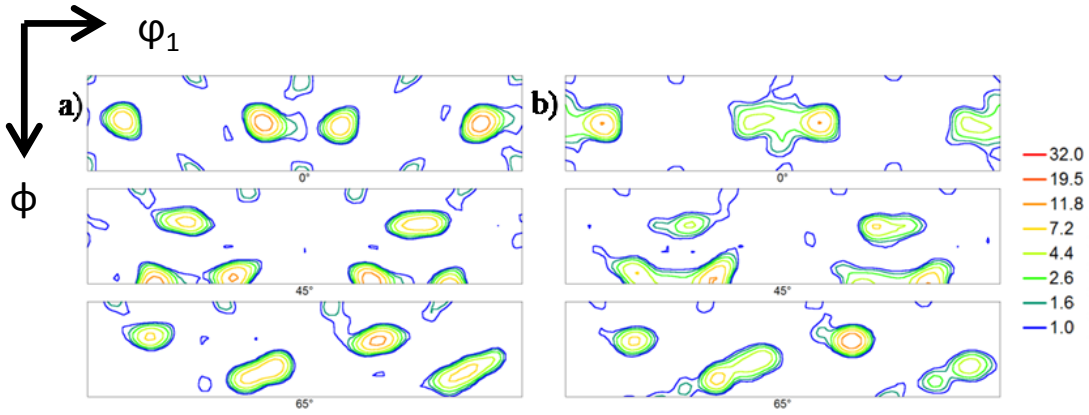

Figure 4-18: ODF sections (with φ_2= 0°, 45°, 65°) of the mid-thickness section after 90% deformation (a) RT, (b) cryogenic.

Figure 4-19, which shows the IQ map together with the HAGBs, LAGBs and ∑3 boundaries, supports this statement. In the bright recrystallized areas, identified by the higher IQ, rectangular shaped ∑3 boundaries were observed. This rectangular morphology is often associated with annealing twins and may thus be related to the occurrence of room temperature annealing. In the deformed part, characterized by the large amount of LAGBs and the lower IQ, lenticular shaped twins were present, which can be identified as deformation twins [1].

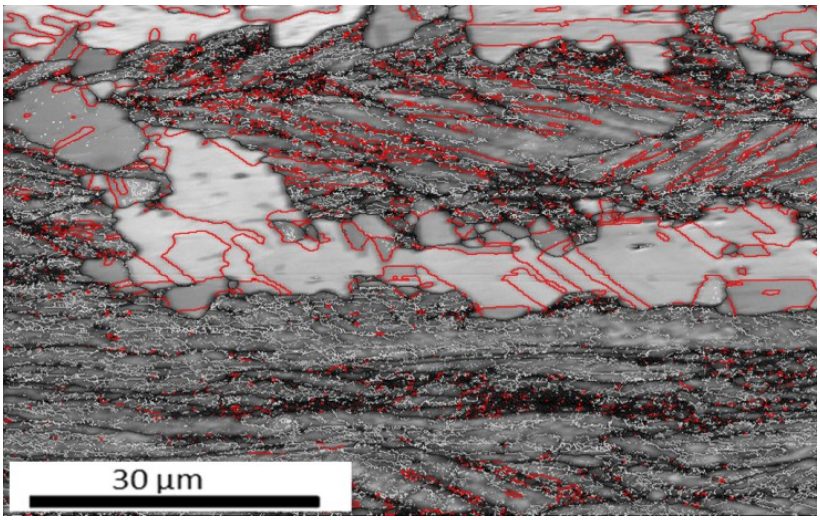

Figure 4-19: Image Quality (IQ) map of the mid-thickness section after 90% cryogenic deformation. HAGBs, LAGBs and ∑3 boundaries are depicted by black, white and red lines, respectively.

4.4.3.3 Annealed material

4.4.3.3.1 Annealed state after 75% deformation

To compare the texture after complete recrystallization for the RT rolled and cryogenically rolled material different annealing treatments were carried out. The first treatment was an annealing in a salt bath for 60 s at 200°C, applied on the 75% RT rolled and the 75% cryogenically rolled samples. In the case of the 75% RT rolled copper sample, the material remained completely deformed, no recrystallized grains were detected. However, when performing the same annealing treatment on the 75% cryogenically rolled material, a fully recrystallized material was obtained. To be able to compare the fully recrystallized textures of the RT rolled copper with the cryogenically rolled copper, an annealing treatment of 180 s at 200°C was performed on the RT rolled copper to produce a completely recrystallized structure.

The texture after annealing of the 75% RT rolled material is shown in figure 4-20a. According to expectation, a strong cube texture was observed with a maximum intensity of 6.6 x random, which is in sharp contrast to the texture observed after complete recrystallization of the 75% cryogenically deformed material (Fig. 4-20c). In the latter case, the texture was very weak with maximum intensity of 2.2 x random. The cube component was entirely absent from the ODF.

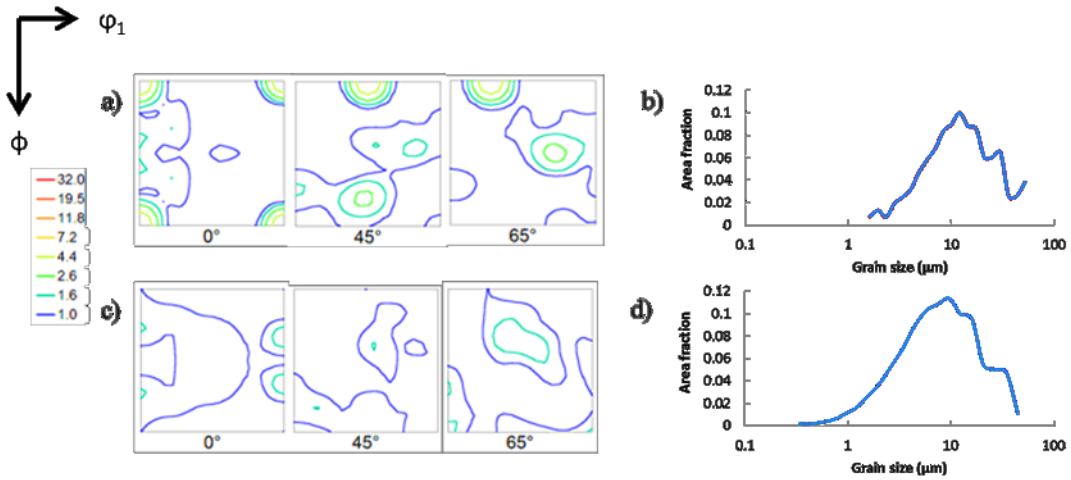

Figure 4-20: (a) ODF sections (with φ_2= 0°, 45°, 65°) and (b) grain size distribution of the mid-thickness section of the sample after 75% RT deformation followed by an annealing treatment of 180 s for 200°C. (c) ODF sections and (d) grain size distribution of the mid-thickness after 75% cryogenic deformation followed by an annealing treatment of 60 s for 200°C.

When comparing the grain size distributions (Fig. 4-20b and 4-20d) of the RT and cryogenically deformed materials annealed to full recrystallization some differences can be observed. The cryogenically rolled material exhibited an average grain size of 1.8 µm, whereas the RT rolled

materials had an average grain size of 5 µm. Both materials had a log-normal grain size distribution and equi-axed grains. With respect to the ∑3 fraction, no large differences were detected between the two materials, i.e. they contain 51% and 50% ∑3 boundaries, respectively.

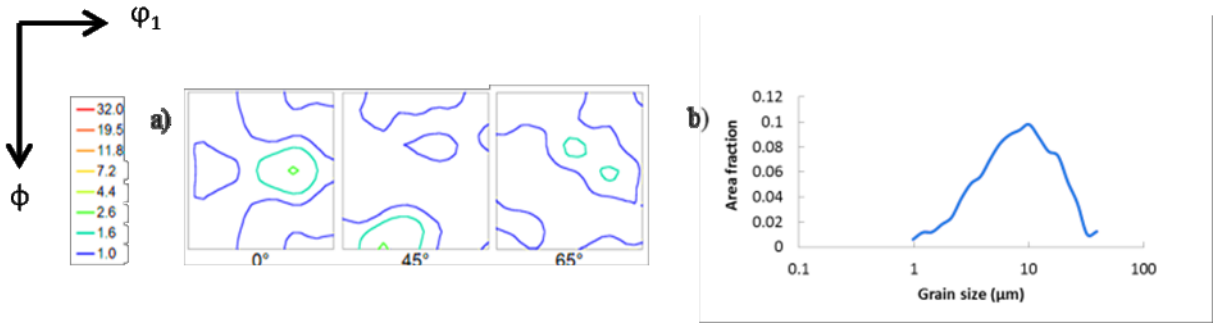

Figure 4-21: (a) ODF sections (with φ_2= 0°, 45°, 65°) and (b) grain size distribution of the mid-thickness of the copper sample after 75% cryogenic deformation followed by an annealing treatment of 180 s for 200°C.

Figure 4-21 shows the texture and the grain size distribution of the 75% cryogenically rolled copper after annealing for 180 s at 200°C. It can be observed that the texture did not evolve substantially; it still remained a nearly random texture, although a tendency for slight strengthening of the cube orientation was observed (compare Fig. 4-21a with Fig. 4.20c). The highest intensity was observed at the P orientation {011} <233>, a recrystallization component which, in Al alloys, is believed to be related to particle stimulated nucleation (PSN) [33, 34]. Engler observed this component inside the SBs in Al-3Mg [18]. The average grain size has increased from 1.8 µm to 3 µm as a result of extended annealing.

4.4.3.3.2 Annealed state after 90% deformation

An annealing treatment in a salt bath at 200°C for 60 s was also applied both on the 90% RT rolled and 90% cryogenically rolled copper samples. In both cases this treatment produced a fully recrystallized material. Figure 4-22a shows the texture of the 90% RT rolled material. The texture was completely dominated by the cube component, which exhibited a maximum of 68.5 random levels. Also in the annealed 90% cryogenically rolled sample the cube component was present (Fig. 4-22c), albeit much less pronounced (maximum intensity 7.4 x random). Similar to the 75% cryogenically deformed sample annealed for 180 s, the P orientation was present. However, now the P component was present together with the Q component. A large difference is observed in the grain size and grain size distributions (Fig. 4-22b and 4-22d) of the two materials. A mean grain size of 1.4 µm, together with a log-normal grain size distribution, was observed in the 90% cryogenically deformed material after recrystallization. This, in contrast with the sample after 90% RT rolling, which exhibited a bimodal grain size distribution, whereby

the smaller grains have an average size of approximately 8 µm and the larger grains a mean grain size of ~100 µm. The majority of the large grains displayed the <001>// ND orientation (cube type). When comparing ∑3 grain boundary fractions, the 90% cryogenic rolled and annealed sample had the higher fraction (65%) compared to the recrystallized 90% RT rolled sample (47%).

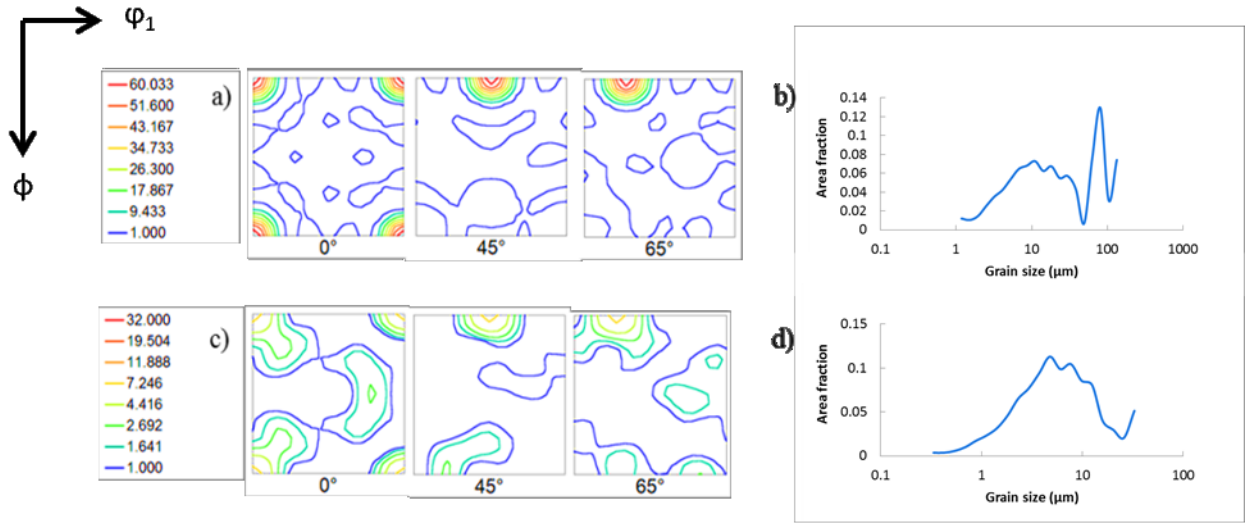

Figure 4-22: (a) ODF sections (with φ_2= 0°, 45°, 65°) and (b) grain size distribution of the mid-thickness of the copper sample after 90% RT deformation followed by an annealing treatment of 60 s for 200°C. (c) ODF sections and (d) grain size distribution of the mid-thickness of the copper sample after 90% cryogenic deformation followed by an annealing treatment of 60 s for 200°C.

4.4.3.4 Modeling texture evolution in the shear bands

The texture evolution inside the SBs of the cryogenically rolled copper was monitored with the visco plastic self-consistent (VPSC) model starting from a random texture [35]. To this purpose the relationship between the macroscopic strain *e* and the shear strain *γ* had to be determined. The strain mode in the SBs is assumed to be simple shear. For negative SBs (Fig. 4-23a), both the angle *α* between the SB and the rolling direction, and the engineering shear strain *γ* are negative, whereas both are positive for positive SBs (Fig. 4-23b).

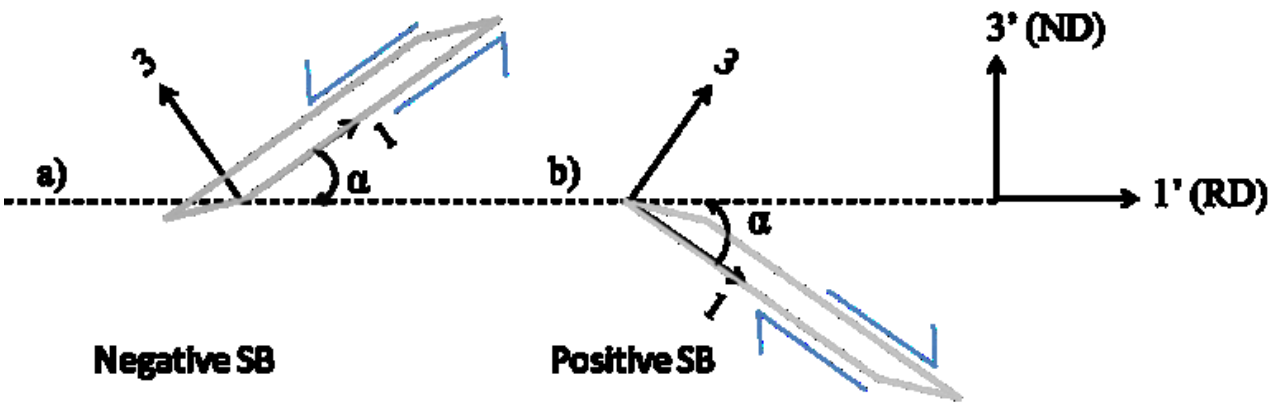

Figure 4-23: Representation of the (a) negative and (b) positive SBs.

The displacement gradient tensor in the macroscopic sample reference system was expressed as:

$$\gamma \begin{pmatrix} \cos\alpha \sin\alpha & 0 & \cos^2\alpha \\ 0 & 0 & 0 \\ -\sin^2\alpha & 0 & -\cos\alpha \sin\alpha \end{pmatrix} \tag{4.3}$$

If it is assumed that the strain may localize in SBs, then the total strain e may be partitioned in a bulk fraction e_B and a shear band fraction e_{SB}:

$$e = e_B (1 - V_{SB}) + e_{SB} V_{SB} \tag{4.4}$$

Whereby V_{SB} represented the volume fraction of the material occupied by SBs.

Assuming that the bulk strain e_B is a fraction β (<1) of the macroscopic strain e then

$$e = \beta e(1 - V_{SB}) + e_{SB} V_{SB} \tag{4.5}$$

The normal strain e_{SB} in the thickness direction for a SB with inclination angle α is related to the shear strain by the following expression:

$$e_{SB} = -\gamma \sin\alpha \cos\alpha \tag{4.6}$$

Consequently,

$$e = \beta e(1 - V_{SB}) - \gamma \sin\alpha \cos\alpha V_{SB} \tag{4.7}$$

From here one can express the strain carried by a SB with respect to the macroscopic strain as:

$$\frac{\gamma}{e} = \frac{1 + \beta(1 - V_{SB})}{V_{SB} \sin\alpha \cos\alpha} \tag{4.8}$$

Figure 4-24 exhibits the strain ratio of the SB to the macroscopic strain as a function of the volume fraction of that SB for two inclination angles, 20° (Fig. 4-24a) and 35° (Fig. 4-24b), i.e. the inclination angles observed in the SBs of the cryogenically rolled material (Fig. 4-16).

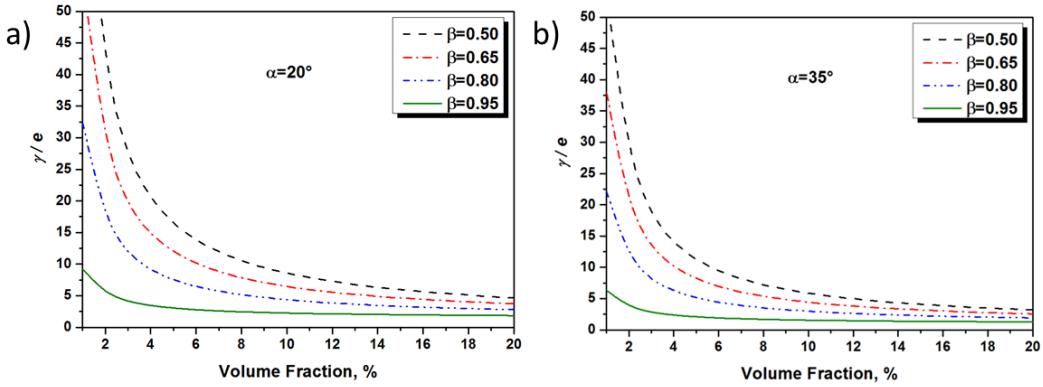

Figure 4-24: Evolution of the shear strain (γ) with respect to the macroscopic strain (e) as a function of the volume fraction of SBs with an inclination angle of 20° (a) and 35° (b) for different fractions of strain accommodated by the matrix.

In general, the shear strain decreased with increasing volume fraction of SBs. Based on the EBSD map of the cryogenically rolled Cu (Figure 4-16b), the volume fraction of both types of SBs was determined. After 75% cryogenic deformation, the deformed copper contained 12% volume fraction of SBs with an inclination angle of 35° and 2% volume fraction of SBs with an inclination angle of 20°. Arbitrarily, assuming that the fraction of macroscopic strain accommodated by the matrix β is between 0.9 and 0.95, it gives rise to a shear strain for both inclination angles between 2 and 7. The β fraction was estimated quite high, because the shear banding is assumed to only accommodate strain at the higher strain amplitudes.

In the crystal plasticity model, the shear strain (γ) was varied between 1 and 10 to observe the effect of the shear strain on the texture evolution inside the SB (Fig. 4-25). In this figure the ODFs were calculated with the VPSC model for positive and negative inclination angles of 20° (Fig. 4-25a) and 35° (Fig. 4-25b). The VPSC model was used with exclusive octahedral slip ({111} <110>), assuming no strain hardening and initial spherical grain shape.

At γ=1 in the SB inclined at ±20° to the RD (Fig. 4-25a) the {012} <122> component is observed, a component close to the Q component. At higher strains the texture tended to rotate towards the β-fiber components. Starting from γ=3 the Dillamore {4 4 11} <11 11 8 > and the ND rotated cube components were intensified. At γ=6 the texture was completely concentrated around the Dillamore component and the ND rotated cube component had rotated towards the

{012} <122> component. At even higher shear strains, the {012} <122> component tended to rotate to the P component via the ideal Q component.

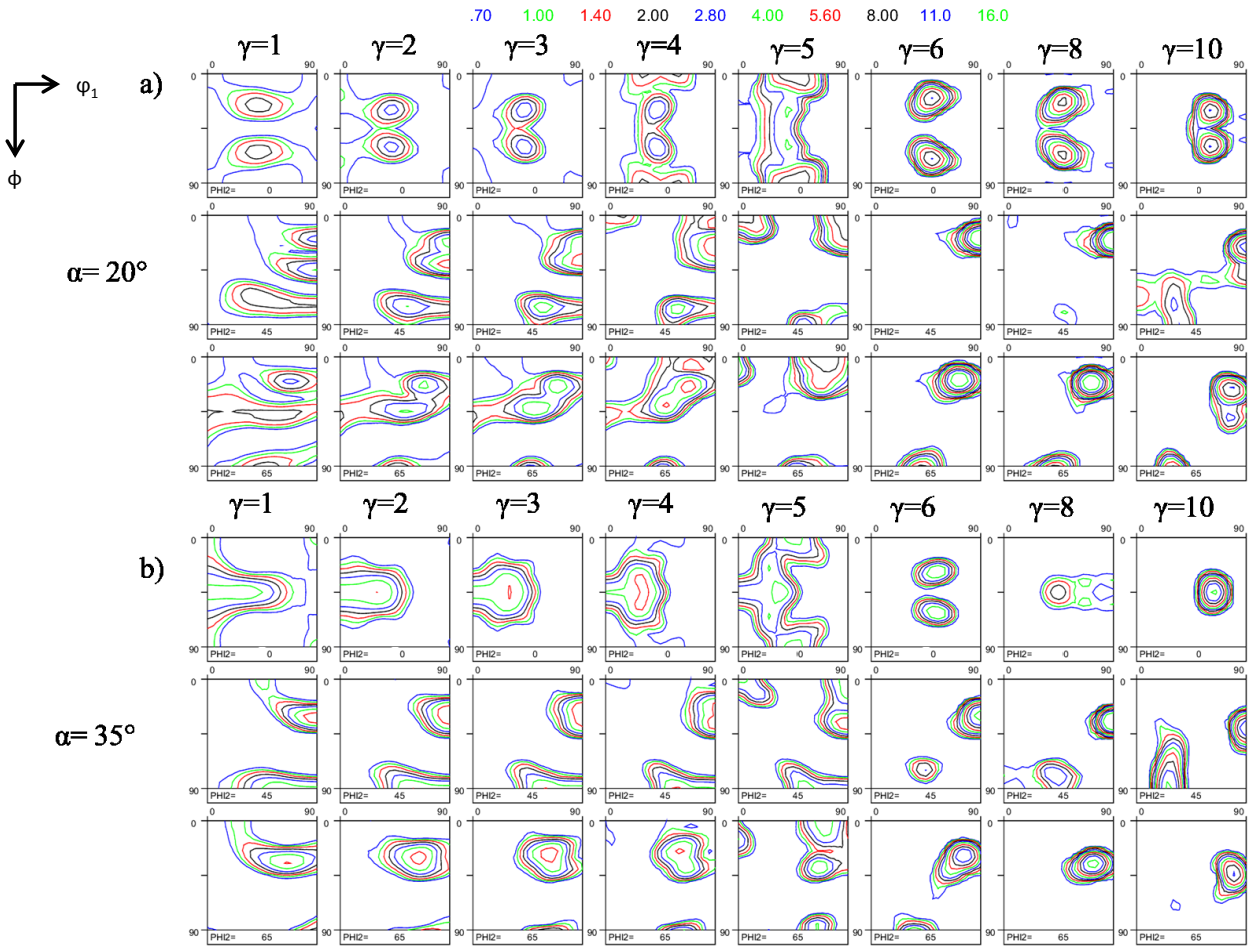

Figure 4-25: ODF sections (with φ_2= 0°, 45°, 65°) of the calculated texture (VPSC) inside SBs with an inclination angle of 20° (a) and 35° (b) for different shear strains (γ= 1, 2, 3, 4, 5, 6, 8 and 10).

When observing the texture evolution in the SB with an inclination angle of ±35° to the RD (Fig. 14-25b) the following observations were made. At lower shear strains, both α- and β-fiber components were observed. At shear strains higher than 4 the brass orientation tended to split up and rotated towards the ND rotated cube component. At *γ*=5 we clearly observed this ND rotated cube component together with the β-fiber orientations. At strains above *γ*=5 the texture rotated towards the P component via the Q component. At *γ*=10 the texture was composed of a strong P and copper component.

In general, for SBs with ±35° and ±20° inclination angles to the RD, the observation was made in the modeled texture, that the ND rotated cube component rotated to the P component via the Q component. This is in good agreement with the assumptions made by Dillamore and Katoh about the origin of the P component in cubic materials [36].

4.4.4 Discussion

4.4.4.1 Effect of RT and cryogenic rolling on the deformation texture

Since the initial material is for both rolling temperatures identical and the texture of the initial sample is completely random (Fig. 4-5), a thorough comparison can be conducted. After 50% RT and cryogenic reduction (Fig. 4-13a and 4-13b), no large difference can be observed between the two textures. Both textures are fairly weak and none of the typical fcc rolling fibers are already present. The observed ND rotated cube orientation is a typical shear texture component. This can be explained by considering the length to mean thickness ratio (*L/h*). The *L/h* ratio for the 50% deformation is low, (*L/h* < 1), and is thus considered to induce strong shear deformation. The reason why this shear component is measured in the mid-thickness of the samples can be the result of the specific roll gap geometry in this experiment, i.e. when the mid-thickness plane of the sample does not coincide with the mid-plane of the rolling gap, the neutral plane in the sample (where the positive and negative shears compensate each other) does not coincide with the mid-thickness plane of the sample.

Comparing the 75% (Fig. 4-14) and the 90% RT and cryogenically rolled copper (Fig. 4-18), some remarkable difference can be perceived. In the 90% cryogenically rolled texture the α-fiber is retained, together with a Goss component that remains strong. This in contrast with the 90% RT rolled texture where weakening of the α-fiber occurred and a sharper texture with pronounced Brass component is observed. It appears that after the cryogenic deformation the texture resembles a Brass type texture, in contrast to the pure metal type texture after RT rolling. A possible explanation for the Brass type texture is the occurrence of deformation twinning, as proposed by Dillamore and Roberts [37]. Numerous lenticular shaped deformation twins are indeed observed after 90% cryogenic deformation (Fig. 4-19), in contrast to the 90% RT rolled material. Another explanation is that the development of a weaker texture after cryogenic rolling is due to the presence of SBs. It is reasonable to assume that the SBs retard the development of the typical rolling textures in the copper matrix.

The effects of strain heterogeneities across the thickness due to roll gap geometry are clearly observed in materials rolled to 50%, 75% and 90% thickness reduction at room temperature. Generally, rolling with high *L/h* ratio > 1 produces a velocity field that closely resembles plane strain compression and hence produces the typical rolling type texture with distinct β-fiber. However, the 75% cryogenically rolled material has characteristics of both shear deformation and plane strain compression. The major differences in texture between the RT rolled and cryogenically rolled sheets after 75% reduction can be explained by the higher friction that is present in the cryogenically rolled material. Due to the reduced temperature compared to RT rolling, more extensive shear deformation is induced during cryogenic rolling. After 90% deformation, both RT and cryogenic rolled textures resemble a plane strain compression

texture. In this case, the texture evolution is governed by the roll gap geometry with high L/h ratio (between 2 and 3.3), ensuring the concentration of shear deformation within the sub-surface layer of the material. The shear could additionally be reduced due to the increase of temperature in the cryogenic experiment. In the current case, the temperature could rise due to heat released during the rolling and due to the heat transfer from the comparatively massive rolling cylinders to the thin sheet.

Another remarkable observation is made in the texture of the RT rolled pure copper, and to a lesser extent in the cryogenic deformed one. Although the initial material has a near random texture, after the higher rolling strain of 90%, the cube component is appearing, albeit in minute strength.

Figure 4-26: Deformed cube grains after 90% deformation (a) RT, (b) cryogenic. LAGB are depicted in white.

Figure 4-26, which represents the deformed (GOS > 2°) cube grains (maximum deviation of 10° for the ideal orientation) in the RT rolled (Fig. 4-18a) and cryogenic rolled copper (Fig. 4-18b), illustrates that the cube orientation is not randomly distributed all over the deformed area, but is present as elongated and deformed grains. The presence of both orientation spread and low angle grain boundaries in the elongated grains of figure 4-26 indicates that the cube component is part of the deformation texture. Figure 4-27 shows the percentage of cube volume fraction (maximum deviation of 10° from the ideal orientation) of both RT rolled and cryogenic rolled pure copper as a function of rolling reduction. The volume fractions are based on the large scale EBSD measurements of the RT and cryogenic rolled materials. Care is taken to ensure that only the texture of the deformed grains was included by excluding grains with a GOS value below 2°. Figure 4-27 shows that cube is formed during the deformation process. Higher deformations tend to stimulate a higher intensity of the cube component. The reason why this cube deformation component is appearing at higher reductions in the cryogenic rolled material than in the RT rolled material can be explained by the following assumptions. Since cube is very sensitive to shear [38] and the higher friction in the cryogenic rolled material leads to more shear, no cube is formed at lower reductions. At higher reductions, the rolled material becomes thinner, and therefore the sample temperature is increased and hence, the deformation texture will be more closely related to the deformation textures formed at RT.

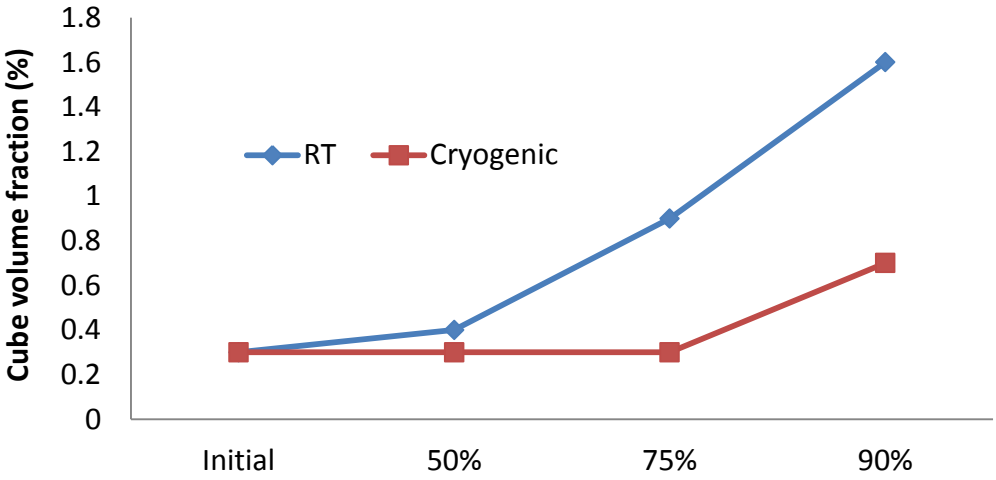

Figure 4-27: Volume fraction of deformed cube orientation in materials rolled at cryogenic and room temperatures (the deformed cube grains are shown in Fig. 4-26).

4.4.4.2 Effect of RT and cryogenic rolling on the deformation microstructure

Some striking differences between the RT rolled and cryogenic rolled microstructures are observed. After 90% RT deformation, no indication of room temperature recrystallization is observed. However, already in the 75% cryogenically rolled copper, that was stored after rolling at -17°C, recrystallized grains are present. Whether this partial recrystallization occurs immediately after the last rolling pass, during low temperature storage, after heating up to room temperature, or during sample preparation, remains unclear. This is in contrast to the findings of Konkova et al. [26], who described the room temperature annealing of cryogenically rolled copper as a relatively slow process. The rapid occurrence of the room temperature recrystallization can be explained by the suppression of dynamic recovery, allowing for an increased accumulated density of dislocations and hence an increased driving force for recrystallization, requiring less thermal activation for the onset of recrystallization [9]. In the 75% cryogenically rolled copper numerous SBs are observed, in contrast to the RT rolled material where no SBs are present. There is a vast body of experimental data showing that SBs act as nucleation sites during recrystallization [16-20] and also this assumption is confirmed in the present study as the grain orientation spread map (Fig. 4-16a) indicates the nucleation of recrystallized grains inside the SBs.

There is evidence of preferred nucleation of some orientations inside the SBs (Fig. 4-16b and Fig. 4-17). The orientations that are associated with nucleation at SBs in Al-alloys, namely Q, Goss, R (retained rolling) and ND rotated cube [16, 18, 21-23] are also observed in the SBs of the 75% cryogenically deformed pure copper. The Goss and the Q components are thought to result

from positive and negative TD rotations associated with the formation of SBs in copper {112} <111> and S {123} <634> oriented grains [24-25]. Also the lower tail of the β-fiber is present inside the SBs (with Brass {011} <211>, {718} <26 50 29> and {314} <596>), together with three orientations newly reported in the present study: {15 12 7} <6 11 6>, {014 }<541>, {114} <110>. No trace of the P component is observed here, although in earlier studies this P component is observed in the macrotexture texture of recrystallized Al-alloys where SBs provide the majority of the nucleation sites [22].

The formation of these components inside the SBs was verified here by applying the VPSC model to plastic strain in positive and negative SBs of 20° and 35° inclination (Fig. 4-25). The recrystallized texture experimentally determined in the SBs after 75% cryogenic deformation is in close resemblance to the modeled deformation texture inside the SBs after an assumed shear strain ratio *γ/e* of 5, compared the ODFs of figure 4-17 and figure 4-25. Given the volume fractions of 12% and 2%, respectively, for ±35° and ±20° inclined SBs, a SB strain ratio *γ/e* of 5 would imply a strain repartition of about 90%. The deformed modeled texture is in close resemblance with the experimentally determined recrystallized grains inside the shear bands. This shows that there is no orientation selection during nucleation inside these SB. These modeled textures could also explain the absence of the P component inside the SB after 75% cryogenic deformation, it seems that the shear strain is not yet high enough to accomplish the rotation from the Q to the P component.

4.4.4.3 Effect of RT and cryogenic rolling on the recrystallization texture

The largest difference between the RT rolled and the cryogenically rolled copper is observed after complete recrystallization. After RT rolling and recrystallization, as expected, a sharp cube texture is developed. After cryogenic rolling and annealing, however, a completely different texture is observed. After 75% cryogenic rolling and annealing, no cube texture is detected and the complete recrystallization texture is very weak.

Figure 4-28 shows that most orientations present in the recrystallized grains can be traced back to SB orientations (Fig. 4-16) after 75% cryogenic rolling and annealing. The P component that was not observed in the SBs is now present in the recrystallization texture. The P component originates from rotations of the Q component in the SBs at higher shear strains (section 4.4.3.4). This suggests that in the bulk volume SBs exist that were subjected to higher shear strains than the shear strain of 5 deduced from the SB orientations in a limited region (Fig. 4-16b).

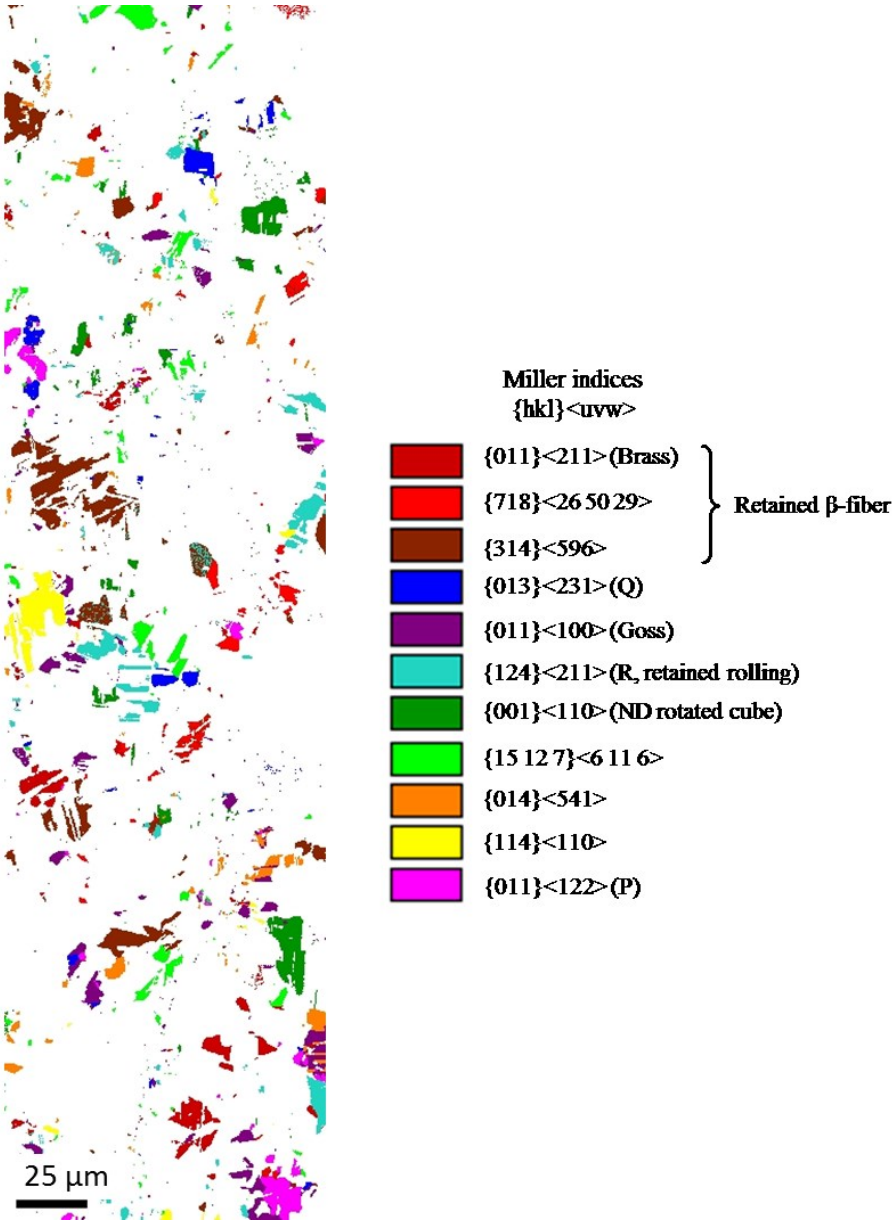

Figure 4-28: Orientation maps of the mid-thickness section of the copper sample after 75% cryogenic deformation followed by an annealing treatment of 60 s for 200°C. All orientations found inside the SBs are depicted on these maps according to the included color code.

Since both the observed recrystallization nuclei and the modeled deformed grains inside the SBs do not display a random texture, an explanation for the weak texture after complete recrystallization has to be given. The data suggest that SB nucleation is prominent in the cryogenically rolled samples, but that in the later stages of annealing an additional randomization process has occurred. It is known from literature that SBs may inhibit cube nucleation since they propagate across the elongated bands of cube oriented cells. In this way they break these cube oriented cells into shorter lengths, destroying their symmetry which

makes them less suitable for nucleation [16]. The further randomization of the texture can be attributed to the presence of annealing twins. The presence of first and second generation annealing twins can induce a texture randomization. An analysis of the length fraction of <110>60° (± 3°) misorientations in the 90% rolled material exhibited a value of 65% and 47% in the cryogenically and RT rolled samples, respectively. It appears that particularly the cube component, which is much more pronounced in the RT rolled material, is less prone to the formation of annealing twins. Hence, the comparative inhibition of cube development in the cryogenically rolled material together with the occurrence of annealing twins predominantly in non-cube oriented grains is responsible for the texture randomization.

After longer annealing times (180 s compared to 60 s), the cryogenically rolled copper remains almost random, but the P component is becoming slightly more intense (intensity: 2.6 x random).

When comparing the annealing texture of the 90% RT and cryogenically rolled material (Fig. 4-13), similar observations can be made as for the 75% deformed material. However, after 90% cryogenic rolling, the texture is no longer completely random, but the cube component is appearing. In contrast to the 75% rolling reduction, at 90% rolling strain, because of the temperature rise due to heat release during rolling and due to heat transfer, the texture will resemble more a RT rolled material and cube nucleation in the bulk of the material will become more important than nucleation at SBs. However, not only the cube component is visible; also a continuous tail from the Q to the P component is present. This is in agreement with the assumption that the P orientation is originating from the rotation of the Q orientation towards the P orientation after further strain (Fig. 4-25).

4.4.4.4 Effect of RT and cryogenic rolling on the grain size and grain size distribution after recrystallization

Although cryogenic rolling is believed to entail the potential of producing nanocrystalline grains [9, 39], this is not the case here. A decrease in grain size is observed in both cryogenically rolled materials, but this decrease is rather small and does not come even close to the nanocrystalline range. A possible explanation is that the accumulated macroscopic strain is not high enough (maximum e: 2.3). Therefore the balance between dislocation generation and recovery is not sufficiently tilted towards efficient storage of high densities of dislocations [9]. The smaller grain size of the 90% cryogenically deformed copper compared to the 75% cryogenic deformed confirms this hypothesis.

When considering the grain size distribution, the main finding is the more narrow recrystallized grain size distribution after cryogenic rolling compared to RT rolling. This is more pronounced in the 90% deformed copper. In this material after RT rolling a bimodal distribution is observed, whereas in the cryogenically rolled material a log-normal grain size distribution persists. The

bimodal distribution is attributed to the much coarser cube grains that are present after recrystallization of the RT rolled material.

4.4.5 Conclusion cryogenic rolling

The texture and microstructure development in cryogenically rolled and RT rolled copper is compared after different rolling reductions, starting from the randomly textured hot rolled material. Whereas the RT rolled copper produces a pure metal texture, the cryogenically rolled copper exhibits a Brass type texture. In the cryogenically rolled material, numerous deformation twins and shear bands are observed, contrary to the RT rolled material. The cube component is observed in both RT and cryogenic rolled copper as part of the deformation texture. After annealing the RT rolled material gives rise to a strong cube texture, in contrast to the cryogenically rolled copper, which exhibits a very weak texture. This weak texture can be attributed to the presence of shear bands inside the cryogenically rolled material. The recrystallization texture inside the shear bands is experimentally determined and is in good agreement with the modeled deformed shear band texture. The cryogenic rolling has also a refining effect on the grain size, although the nanocrystalline range is not reached in the present experiment.

4.5 Conclusion

In this chapter, the controlled variation of the microstructure of pure Cu is discussed. By controlling the deformation and annealing parameters, the grain size, the grain boundary distribution and the texture can be controlled to a certain extent.

After hot rolling of the cast copper, the mean grain size is reduced from an original value of 343 µm to 14 µm. The length fraction of ∑3 boundaries increased for about 0.3% in the cast copper to 12% after hot rolling. An almost fully random texture is observed for both the cast as the hot rolled copper. After RT rolling, pancaked, more elongated grains are observed and a typical rolling texture is developed, consisting of the Goss, Brass, Copper, and S components. By changing the annealing temperatures and times after RT rolling, a quite broad range in RX grain size and intensity of cube component can be obtained. Also the fraction of ∑3 boundaries is dependent on the applied annealing parameters, although no values higher than 54% are obtained after RT rolling and annealing. With the cryogenic rolling it is possible to produce a material with mean grain sizes around 1 µm, a nearly random texture and ∑3 length fractions around 65%.

After a full characterization of the microstructure, the corresponding electrochemical behavior can be determined. In the following chapter Atomic Force Microscopy (AFM) combined with electron backscatter diffraction (EBSD) will be used to quantify the electrochemical behavior of pure copper related to its microstructural features.

4.6 References

1. Humphreys, F.J. and M. Hatherly, Recrystallization and Related Annealing Phenomena. 2004, Oxford: Elsevier Ltd.

2. Sidor, J.J. and L.A.I. Kestens, Analytical description of rolling textures in face-centred-cubic metals. Scripta Materialia, 2013. 68(5): p. 273-276.

3. Hirsch, J. and K. Lucke, Mechanism of deformation and development of rolling textures in polycrystalline fcc metals .2. Simulation and interpretation of experiments on the basis of taylor-type theories. Acta Metallurgica, 1988. 36(11): p. 2883-2904.

4. Konkova, T.N., S.Y. Mironov, A.V. Korznikov and M.M. Myshlyaev, Formation of the microstructure in the course of low-temperature annealing of cryogenically deformed copper. Doklady Physics, 2013. 58(6): p. 240-243.

5. Li, Y.S., N.R. Tao and K. Lu, Microstructural evolution and nanostructure formation in copper during dynamic plastic deformation at cryogenic temperatures. Acta Materialia, 2008. 56(2): p. 230-241.

6. Edalati, K., T. Daio, M. Arita, S. Lee, Z. Horita, A. Togo and I. Tanaka, High-pressure torsion of titanium at cryogenic and room temperatures: Grain size effect on allotropic phase transformations. Acta Materialia, 2014. 68(15): p. 207-213.

7. Darling, K.A., M.A. Tschopp, A.J. Roberts, J.P. Ligda and L.J. Kecskes, Enhancing grain refinement in polycrystalline materials using surface mechanical attrition treatment at cryogenic temperatures. Scripta Materialia, 2013. 69(6): p. 461-464.

8. Magalhaes, D.C.C., M.F. Hupalo and O.M. Cintho, Natural aging behavior of AA7050 Al alloy after cryogenic rolling. Materials Science and Engineering a-Structural Materials Properties Microstructure and Processing, 2014. 593: p. 1-7.

9. Wang, Y.M., M.W. Chen, H.W. Sheng and E. Ma, Nanocrystalline grain structures developed in commercial purity Cu by low-temperature cold rolling. Journal of Materials Research, 2002. 17(12): p. 3004-3007.

10. Zhang, Y., N.R. Tao and K. Lu, Mechanical properties and rolling behaviors of nano-grained copper with embedded nano-twin bundles. Acta Materialia, 2008. 56(11): p. 2429-2440.

11. Sarma, V.S., J. Wang, W.W. Jian, A. Kauffmann, H. Conrad, J. Freudenberger and Y.T. Zhu, Role of stacking fault energy in strengthening due to cryo-deformation of FCC metals. Materials Science and Engineering a-Structural Materials Properties Microstructure and Processing, 2010. 527(29-30): p. 7624-7630.

12. Konkova, T., S. Mironov, A. Korznikov and S.L. Semiatin, Microstructural response of pure copper to cryogenic rolling. Acta Materialia, 2010. 58(16): p. 5262-5273.

13. Konkova, T.N., S.Y. Mironov, V.N. Danilenko and A.V. Korznikov, Effect of Low-Temperature Rolling on the Structure of Copper. Physics of Metals and Metallography, 2010. 110(4): p. 318-330.

14. Paul, H., A. Morawiec, E. Bouzy, J. Fundenberger and A. Piatkowski, Brass-type shear bands and their influence on texture formation. Metallurgical and Materials Transactions a-Physical Metallurgy and Materials Science, 2004. 35A(12): p. 3775-3786.

15. Ridha, A.A. and W.B. Hutchinson, Recrystallization mechanisms and the origin of cube texture in copper. Acta Metallurgica, 1982. 30(10): p. 1929-1939.

16. Duckham, A., O. Engler and R.D. Knutsen, Moderation of the recrystallization texture by nucleation at copper-type shear bands in Al-1Mg. Acta Materialia, 2002. 50(11): p. 2881-2893.

17. Hatherly, M. and A.S. Malin, Shear bands in deformed metals. Scripta Metallurgica, 1984. 18(5): p. 449-454.

18. Engler, O., An EBSD local texture study on the nucleation of recrystallization at shear bands in the alloy Al-3Mg. Scripta Materialia, 2001. 44(2): p. 229-236.

19. Paul, H., A. Morawiec, J.H. Driver and E. Bouzy, On twinning and shear banding in a Cu-8 at.% Al alloy plane strain compressed at 77 K. International Journal of Plasticity, 2009. 25(8): p. 1588-1608.

20. Paul, H., J.H. Driver, C. Maurice and Z. Jasienski, Crystallographic aspects of the early stages of recrystallisation in brass-type shear bands. Acta Materialia, 2002. 50(17): p. 4339-4355.

21. Engler, O., Influence of the Initial Grain Size on the Rolling and Recrystallization Textures in the Alloy Al-1.8% Cu. Textures and Microstructures, 1995. 23(2): p. 61-86.

22. Engler, O., J. Hirsch and K. Lucke, Texture development in al-1.8 wt-percent cu depending on the precipitation state .2. Recrystallization textures. Acta Metallurgica Et Materialia, 1995. 43(1): p. 121-138.

23. Hjelen, J., R. Orsund and E. Nes, Overview no 93 - on the origin of recrystallization textures in aluminum. Acta Metallurgica Et Materialia, 1991. 39(7): p. 1377-1404.

24. Engler, O., Nucleation and growth during recrystallisation of aluminium alloys investigated by local texture analysis. Materials Science and Technology, 1996. 12(10): p. 859-872.

25. Wagner, P., O. Engler and K. Lucke, Formation of cu-type shear bands and their influence on deformation and texture of rolled fcc (112) 111 single-crystals. Acta Metallurgica Et Materialia, 1995. 43(10): p. 3799-3812.

26. Konkova, T., S. Mironov, A. Korznikov, and S.L. Semiatin, On the room-temperature annealing of cryogenically rolled copper. Materials Science and Engineering a-Structural Materials Properties Microstructure and Processing, 2011. 528(24): p. 7432-7443.

27. Asbeck, H.O. and H. Mecking, Influence of friction and geometry of deformation on texture inhomogeneities during rolling of cu single-crystals as an example. Materials Science and Engineering, 1978. 34(2): p. 111-119.

28. Truszkowski, W., J. Krol and B. Major, Inhomogeneity of rolling texture in fcc metals. Metallurgical Transactions a-Physical Metallurgy and Materials Science, 1980. 11(5): p. 749-758.

29. Lee, C.S. and B.J. Duggan, A simple theory for the development of inhomogeneous rolling textures. Metallurgical Transactions a-Physical Metallurgy and Materials Science, 1991. 22(11): p. 2637-2643.

30. Dillamore, I.L., A.J. Roberts and A.C. Bush, Occurrence of shear bands in heavily rolled cubic metals. Metal Science, 1979. 13(2): p. 73-77.

31. Nguyen-Minh, T., .J. Sidor, R.H. Petrov and L.A.I. Kestens, Occurrence of shear bands in rotated Goss ({110} < 110 >) orientations of metals with bcc crystal structure. Scripta Materialia, 2012. 67(12): p. 935-938.

32. Harren, S.V., H.E. Deve and R.J. Asaro, Shear band formation in plane-strain compression. Acta Metallurgica, 1988. 36(9): p. 2435-2480.

33. Engler, O., X.W. Kong and P. Yang, Influence of particle stimulated nucleation on the recrystallization textures in cold deformed Al-alloys .1. Experimental observations. Scripta Materialia, 1997. 37(11): p. 1665-1674.

34. Schafer, C. and G. Gottstein, The origin and development of the P{011}< 111 > orientation during recrystallization of particle-containing alloys. International Journal of Materials Research, 2011. 102(9): p. 1106-1114.

35. Lebensohn, R.A. and C.N. Tome, A self-consistent anisotropic approach for the simulation of plastic-deformation and texture development of polycrystals - application to zirconium alloys. Acta Metallurgica Et Materialia, 1993. 41(9): p. 2611-2624.

36. Dillamore, I.L. and H. Katoh, The mechanisms of recrystallization in cubic metals with particular reference to their orientation-dependence. Metal Science, 1974. 8(3): p. 73-83.

37. Dillamore, I.L. and W.T. Roberts, Rolling textures in f.c.c. and b.c.c. metals. Acta Metallurgica, 1964. 12(3): p. 281-293.

38. Sidor, J., A. Miroux, R. Petrov and L.A.I. Kestens, Microstructural and crystallographic aspects of conventional and asymmetric rolling processes. Acta Materialia, 2008. 56(11): p. 2495-2507.

39. Konkova, T.N., S.Y. Mironov and A.V. Korznikov, Refining of grains in copper by means of cryogenic deformation. Metal Science and Heat Treatment, 2011. 53(1-2): p. 95-100.

Chapter 5
A combined AFM and EBSD study to elucidate the relationship between microstructure and electrochemical activity[1]

In the previous chapter a detailed evaluation was given on the impact of different routes of thermomechanical processing on the microstructural features of the high purity copper which is used in this doctoral thesis. Apart from the observations made on the different physical metallurgical characteristics of the material and how they are influenced by TMP, these changes are also relevant when studying the electrochemical response of the material on a microscopic scale. TMP indeed allows changing to a certain extent the microstructure to make it more suitable for the local electrochemical technique which is used. The present chapter is the first of three experimental chapters that focus on the study, evaluation and quantification of the electrochemical behavior of the high purity copper related to its microstructural features. In this chapter the combined use of Atomic Force Microscopy (AFM) and electron backscatter diffraction (EBSD) it was possible to link the dissolution behavior of polycrystalline copper when submerged in an electrolyte to specific crystallographic and microstructural features.

5.1 Introduction

Recent literature suggests a significant influence of the local crystallographic features on the corrosion behavior of metals. These conclusions were drawn from two types of studies: on the one hand, from local studies on single crystals [1-5] and, on the other hand, from the local evaluation of individual grains in polycrystalline metals [6-10]. Only a few works quantify the corrosion kinetics comparing differently oriented grains. Lill *et al.* investigated the critical current density for the transition from active to passive behavior of a FeAlCr steel (bcc crystal structure) using cyclic voltammetry in a microcapillary cell [11]. Their conclusion was that the critical current density on a grain with <100>// ND orientation is 53% higher as compared to a <111>// ND oriented grain. Schreiber *et al.* [10] measured different current densities on the crystallographic (100) and (111) planes in iron (bcc crystal structure). Their experiment showed that corrosion occurred faster on the most closely packed (111) planes. In a Cu bi-crystal, the misorientation between grains is reported to affect the anodic/cathodic nature of the grains with respect to the grain boundaries [12]. In their work, Miyamoto *et al.* stated that there is a critical misorientation angle between 70.5° and 105° that determines if the grain or the grain

[1] This chapter is based on the following publication: L. Lapeire, E. Martinez Lombardia, K. Verbeken, I. De Graeve, L.A.I. Kestens, H. Terryn, Effect of neighboring grains on the microscopic corrosion behavior of a grain in polycrystalline copper, Corrosion Science 67 (2013) 179-183.

boundary will be attacked or not. Lee and White investigated the dissolution rate of aluminum single crystals (fcc crystal structure) proving that the dissolution rate depends on the crystallographic orientation being the order: (111) > (110) > (001). However, they did not provide an explanation for these findings [13]. All these studies demonstrate that the local, microscopic features influence the electrochemical behavior, but a physically based explanation is still lacking.

Therefore, the grain dependent electrochemical behavior requires more study. This is performed here for polycrystalline high purity Cu by immersing this material in two electrolytes, namely 0.1 M NaCl and 0.5 M Na_2SO_4. By Atomic Force Microscopy (AFM), surface topology visualization was performed, which allowed to evaluate height differences between differently oriented grains after corrosion. The corresponding crystallographic orientation data were obtained by electron backscatter diffraction (EBSD). Comparison between the results obtained with both techniques allowed evaluating the effect of the grain orientation on the corrosion behavior of a polycrystalline material. The basic concepts of the EBSD technique were already discussed above (section 3.3.2), therefore only some background on the AFM technique is given here.

5.2 Atomic force microscopy

Atomic force microscopy (AFM) is one kind of scanning probe microcopy (SPM), where a small probe is used to scan across the sample to obtain information on the surface of the sample [14]. The data are collected as the probe scans along a raster pattern across the sample to form a map of the measured property relative to the X-Y position. The measured property is dependent on the information gathered from the probe's interaction with the sample surface.

The AFM probe has a very sharp tip, in the order of a few nanometers, at the end of a small cantilever. The probe is attached to a piezoelectric scanner tube, which scans the probe across a selected area of the surface. Interatomic forces between the probe tip and the sample surface cause the cantilever to deflect as the sample's surface topography changes. The optical cantilever operates by reflecting a laser beam off the cantilever. The reflected laser beam strikes the position-sensitive photo-detector consisting of a four-segment photo-detector. The differences between the segments indicate the position of the laser spot on the detector and thus the angular deflection of the cantilever (Fig. 5-1).

In this work, the AFM measurements were performed using a Veeco CP II system. The contact mode AFM is used, since we are interested in the surface topology [15]. When working in contact mode, the AFM probe is scanned at a constant force between the probe and the sample surface to obtain a topographical map. When the probe cantilever is deflected by the topographical changes, the scanner adjusts the probe position to restore the original cantilever

deflection. The position of the scanner is used to create a topographical image. Lateral resolution of <1 nm and a height resolution < 0.1 nm were obtained.

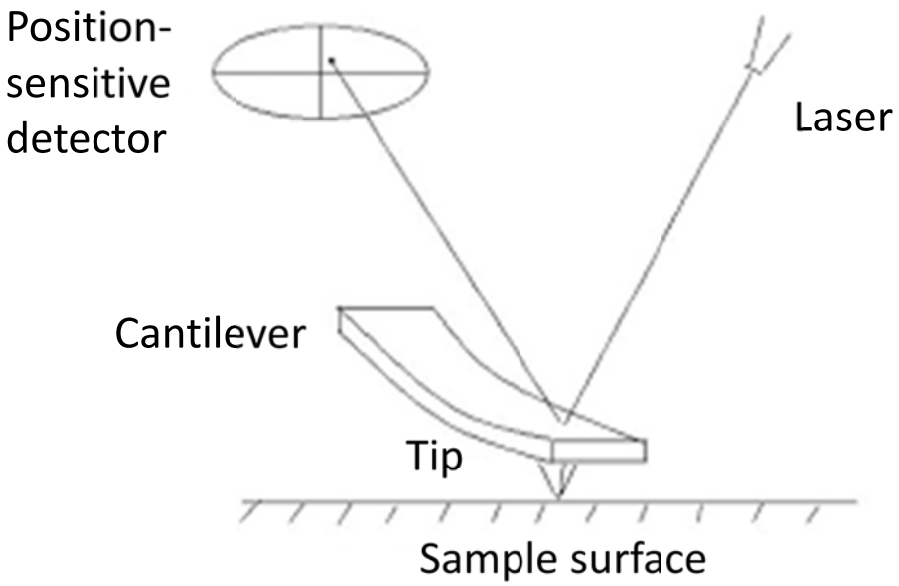

Figure 5-1: Schematic representation of the AFM technique [14].

5.3 Experimental details

In this chapter, the high purity copper underwent a 75% hot rolling reduction, which allowed destroying the cast microstructure and providing a completely recrystallized microstructure, as discussed in section 4.3.2. A room temperature (RT) rolling reduction of 80 % was followed by an annealing treatment for 60 min at 250°C. Subsequently, the material was mechanically ground and polished, finishing with 1 µm diamond paste. In order to be able to identify a unique site of the microstructure with both AFM and EBSD, three indents of 15 µm diameters were made with a Vickers micro-indenter inside a larger polygonal indent (Fig. 5-2).

The hot rolled sample was submerged for 60 min in 0.5 M Na_2SO_4 and the RT rolled and annealed sample for 210 min in 0.1 M NaCl. Na_2SO_4 and NaCl were chosen as electrolyte to evaluate possible differences in corrosion behavior in a Cl^- free and a Cl^- containing medium. The immersion time and electrolyte concentration were determined after an optimization of the experimental parameters with the aim to obtain appropriate conditions for corrosion and, in the meantime, exclude pitting. Subsequently, AFM topology measurements were performed. To obtain a suitable surface preparation for EBSD, a final electropolishing step (10 V, 10 s) in a

phosphoric acid electrolyte appeared to be necessary. EBSD measurements were carried out with a step size of 0.5 µm.

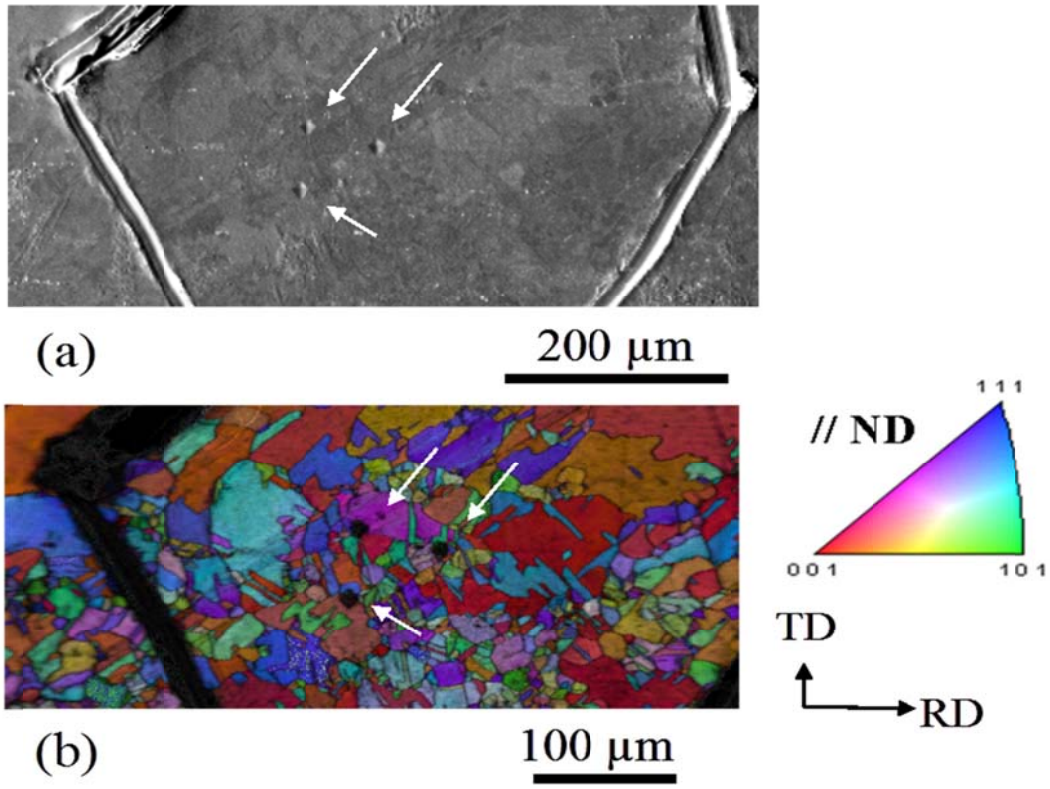

Figure 5-2: (a) Secondary electron (SE) image and (b) combined inverse pole figure (IPF)/ image quality (IQ) map of the polygonal area surrounding the 15 µm large micro-indents.

5.4 Results

5.4.1 AFM measurement on non-exposed high purity Cu

First of all, AFM measurements were conducted on the unexposed high purity copper in order to evaluate the surface characteristics before the corrosion process. These measurements showed that no significant height differences were present on the sample surface, apart from height differences that could be attributed to scratches, which had an average depth of about 2 nm. Consequently, it could be concluded that height differences detected after immersion of the high purity copper in the electrolyte could be attributed to the electrolytically induced copper corrosion.

5.4.2 RT rolled and annealed high purity Cu submerged for 210 min in 0.1 M NaCl

After submerging the RT rolled and annealed material in the corrosive environment, significant height differences were present. Indeed, these differences were already visible with the optical microscope attached to the AFM. In regions with a significant height difference an AFM measurement (Fig. 5-3) was conducted in order to quantify these height differences, as illustrated for the four grains marked on figure 5-3a and 5-3b.

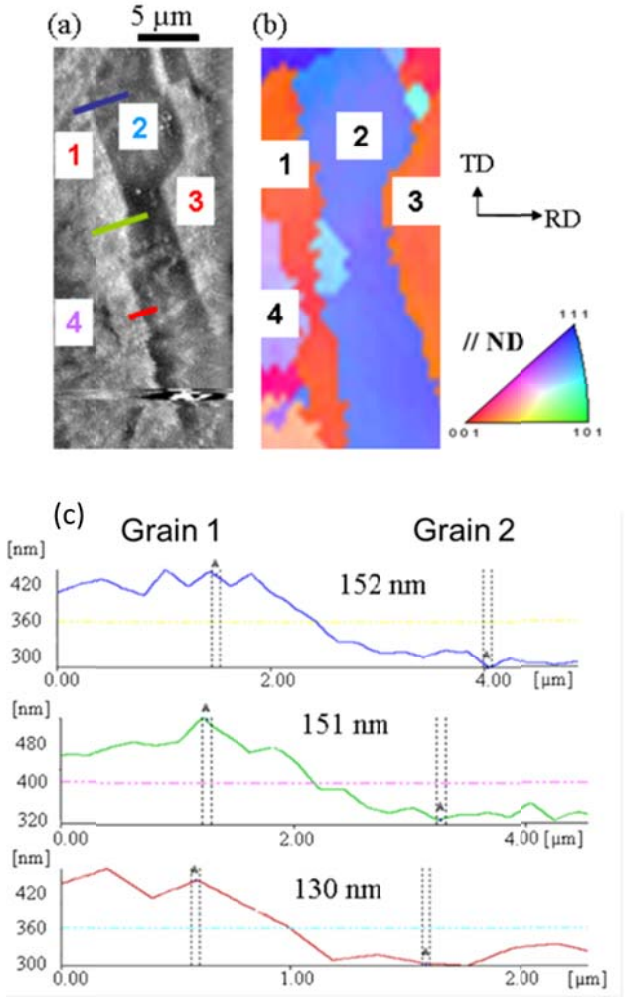

Figure 5-3: (a) Topographic map with indication of the three line scans, (b) IPF map of the rolled and annealed high purity Cu immersed for 210 min in 0.1 M NaCl. (c) Three line scans between grain 1 and 2 determine the average height difference between these grains. This average is also given on the figure.

Subsequently, EBSD was used to link the observed height differences to specific crystallographic orientations. From the IPF map (Fig. 5-3b), it was observed that grain 1 and 3 have an orientation close to <001>// ND while grain 2 is oriented close to <111>// ND and grain 4 has a

nearly <112>// ND orientation. To determine the height difference between two adjacent grains, three line scans were conducted and the average height differences of these line scans were taken as a measure for the height difference between these two adjacent grains (Fig. 5-3c). Table 5.1 displays the average height differences between the different grains observed in figure 5-3a and 5-3b.

Grain	Grain	Average height difference [nm]
1	2	144 ± 10.1
2	3	117 ± 13.0
1	3	7 ± 6.6
1	4	29 ± 3.9

Table 5.1: Average height difference and standard deviation based on three line scans between the four grains marked on figure 5-3.

It can be clearly seen that considerable differences between some specific grains are present with averages ranging from 7 to 144 nm. When AFM and EBSD results are compared, a large height difference is observed when adjacent grains have a near <111>// ND and <001>// ND orientation, respectively. For this specific case, the grain with a crystallographic orientation close to <111>// ND shows a significantly higher dissolution rate than its neighbor.

Confirmation of the presented observations was found on another location on the same sample surface. Significant height differences were observed and AFM (Fig. 5-4a) and EBSD (Fig. 5-4b) measurements were combined in order to quantify the height difference and to identify the corresponding crystallographic orientations. Two line scans were performed indicated by the red (Fig. 5-4c) and white (Fig. 5-4d) line on the topographic image. Similar observations were obtained as in the previously analyzed sample. A large height difference is observed on the topographic map when adjacent grains have near <111>// ND (grains A, B and C) and <001>// ND orientation (grains D and E), with the <111>// ND orientations showing a higher dissolution rate. This is again nicely illustrated with the line scan across grains D, B, E and C (Fig. 5-4c), which clearly shows the distinct dissolution rate between the differently oriented grains. The height difference between grains oriented close to <111>// ND and <001>// ND was again averaged over three line scans and a similar value of about 145 nm with a limited standard deviation was found.

The data presented so far suggest that a pair of adjacent grains of <111>// ND and <001>// ND orientation is an absolute prerequisite for observing a significant height difference across a grain boundary after corrosion induced by submerging the copper sample in an electrolyte. By meticulous optical microscopy investigation other severely attacked grains were searched for. However, on this particular surface, none were found which did not involve a <111>// ND oriented grain adjacent to a <100>// ND oriented grain. As an illustration, this can be deduced

from the line scan indicated in white (Fig. 5-4d) and the topographic map of figure 5-5a. Although near <111>// ND and <001>// ND grains are present in this area, no significant height difference could be retrieved because the condition that a <111>// ND grain neighbors a <001>// ND orientation was not fulfilled here, as is demonstrated by the corresponding inverse pole figure map.

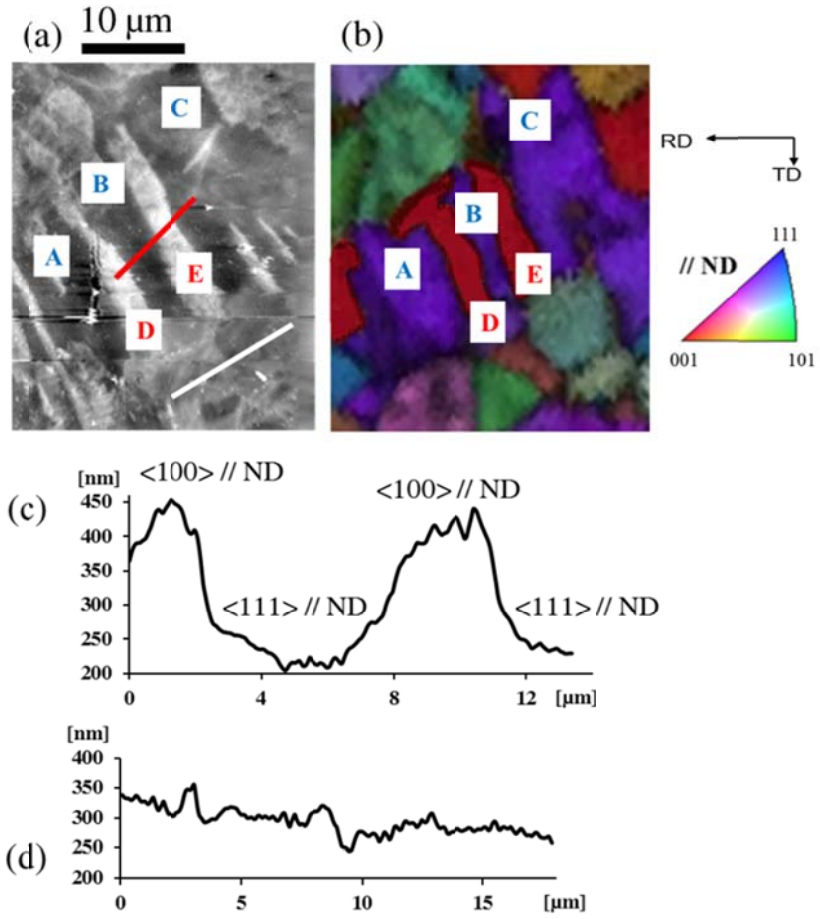

Figure 5-4: (a) Topographic map with indication of two line scans and (b) combined IPF/IQ map of the RT rolled and annealed high purity Cu immersed for 210 min in 0.1M NaCl. Line scan of the line indicated in red (c) and white (d) on the topographic map.

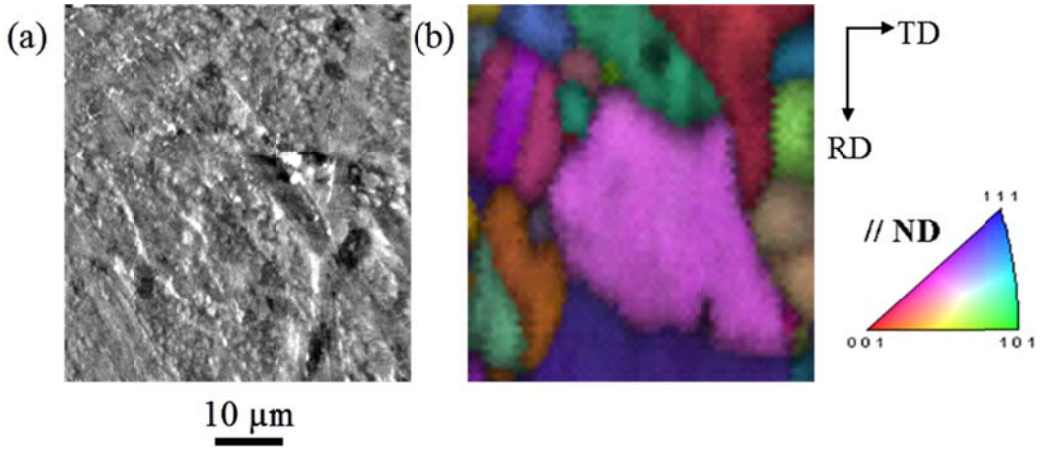

Figure 5-5: (a) Topographic map and (b) combined IPF/ IQ map of the RT rolled and annealed high purity Cu immersed for 210 min in 0.1 M NaCl.

In order to further validate the apparent tendency, another corrosion experiment was conducted. This experiment was performed on the hot rolled material and consisted of submerging it into another corrosive environment, namely Na_2SO_4.

5.4.3 Hot rolled high purity Cu submerged for 60 min in 0.5 M Na_2SO_4

As mentioned above, another set of experimental parameters combined with another electrolyte were applied on the high purity Cu samples. By using the optical microscope attached to the AFM equipment, the locations with the most significant height differences were traced and height differences were measured (Fig. 5-6a) in a similar manner as the one applied above. The combination of AFM and EBSD analysis allowed again correlating height differences with crystallographic orientations, as illustrated in figure 5-6. From the IPF/IQ map (Fig. 5-6b), it was observed that grain 1' has an orientation close to <001>// ND while grains 2' and 3' are oriented near <111>// ND and grain 4' has an orientation close to <102>//ND. The height differences of pairs (1', 2') and (1', 3') are 56 and 40 nm, respectively. Between grain 1' and 4' no significant height differences were observed. When performing AFM analysis over a larger area than the one shown in figure 5-6, no further significant height differences were observed. In addition, the corresponding IPF map indicated that no grains with an orientation near <001>// ND adjacent to a grain with an orientation close to <111>// ND were present in the area under investigation, although the different orientations were separately observed during the EBSD analysis.

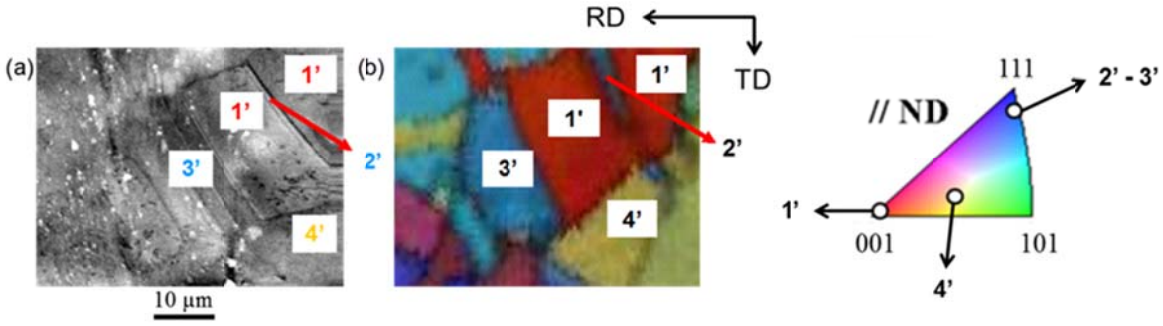

Figure 5-6: (a) Topographic map and (b) combined IPF/ IQ map of the hot rolled high purity Cu immersed for 60 min in 0.5 M Na_2SO_4.

5.5 Discussion

High purity Cu, both after hot rolling and after RT rolling and annealing, was submerged in two different corrosive environments. This caused in both cases a considerable attack of the <111>// ND orientations, on the condition that they were adjacent to a <001>// ND oriented grain. The difference in dissolution behavior in the 0.5 M Na_2SO_4 solution was less pronounced than in the 0.1 M NaCl solution, but the same trend was repeatedly observed and no indications opposite to the trend were noticed. Consequently, the results suggested that not only the grain orientation itself determines the corrosion behavior, but a specific orientation relation with the neighboring grains appears to be an additional prerequisite. The anisotropy in corrosion behavior of the differently oriented grains is likely to be attributed to the anodic/cathodic nature of the differently oriented grains. Consequently, when the differences in electrochemical potential are large enough, a larger dissolution rate is observed in the anodic grain. The above results suggest that the largest difference in electrochemical potential is between the <001>// ND and the <111>// ND oriented grains. This is in agreement with the findings of Lee et al [13] who investigated the influence of the dissolution rate on the crystallographic orientation in Al single crystals. They found out that the dissolution rate depends on the crystallographic orientation in the order: (111) > (110) > (001). This is confirmed, also in Al single crystals, by Seo et al. [16] and Treacy et al. [17], however, they did not provide any explanation for their findings.

Wang et al [18], who measured the dissolution behavior of polycrystalline Alloy 690 (fcc crystal structure) following the procedure proposed in this chapter, confirms a higher dissolution rate if the surface normal vector diverges to <111>. They suggest that Alloy 690 dissolves preferentially along the direction which has lower surface energy; since lower surface energy implies that less energy is needed to remove a one-atom thick layer of surface. So a possible assumption might be to correlate the electrochemical potential with the surface energy.

Surface energies for different low-index crystal planes of Cu have been calculated using various methods including the modified embedded-atom method [19], the modified analytical embedded-atom method (MAEAM) [20] and the empirical electron surface model [21]. For all three methods, the calculated surface energies show a strong anisotropy, with the close-packed plane (111) having the lowest surface energy. For the low index planes in the three different calculations, the ranking of surface energies was reported to be (111) < (100) < (110) < (210). From the surface energy point of view the largest difference in dissolution behavior should be observed between the (111) and (210) planes, which is not in agreement with the current observations. This corresponds, however, to our present observation that in addition to the specific grain orientations and surface energies also the misorientation between adjacent grains plays a significant role.

5.6 Conclusion

The grain dependent electrochemical behavior of polycrystalline high purity Cu is studied by immersion of the material in a solution of 0.1 M NaCl and 0.5 M Na_2SO_4. By employing AFM and EBSD it was possible to link the dissolution behavior of the polycrystalline material to specific crystallographic orientations. The largest dissolution gradient, evaluated by surface elevation differences, is observed between adjacent grains with near <001>// ND and near <111>// ND orientations, respectively. No significant height differences were observed between adjacent grains of different other orientations, nor when the <001>// ND and <111>// ND grains were separately evaluated. These results suggest that not only the grain orientation has an influence on the corrosion behavior, but that the orientation of the neighboring grains seems to play a decisive role in the dissolution rate.

In order to obtain a more detailed description of the observed correlation between the dissolution behavior and the interaction of these grains with their neighbors, other techniques have to be included. These techniques might also provide improved statistics as compared to the combination of AFM and EBSD which was presented in this chapter and where one might argue that an increased number of observations is required to strengthen our conclusions. In the next chapter, the gold nanoplating technique, developed in the frame of the collaboration between UGent and VUB will be explained and the results generated with this technique on the electrochemical activity of grains and grain boundaries will be discussed in detail.

5.7 References

1. Kunze, J., V. Maurice, L.H. Klein, H.H. Strehblow and P. Marcus, In situ STM study of the duplex passive films formed on Cu(111) and Cu(001) in 0.1 M NaOH. Corrosion Science, 2004. 46(1): p. 245-264.

2. Maurice, V., L.H. Klein, H.H. Strehblow and P. Marcus, In situ STM study of the surface structure, dissolution, and early stages of electrochemical oxidation of the Ag(111) electrode. Journal of Physical Chemistry C, 2007. 111: p. 16351-16361.

3. Seyeux, A., V. Maurice, L.H. Klein and P. Marcus, In situ scanning tunnelling microscopic study of the initial stages of growth and of the structure of the passive film on Ni(111) in 1 mM NaOH(aq). Journal of Solid State Electrochemistry, 2005. 9(5): p. 337-346.

4. Vogt, M.R., A. Lachenwitzer, O.M. Magnussen and R.J. Behm, In-situ STM study of the initial stages of corrosion of Cu(100) electrodes in sulfuric and hydrochloric acid solution. Surface Science, 1998. 399(1): p. 49-69.

5. Wiame, F., V. Maurice and P. Marcus, Initial stages of oxidation of Cu(111). Surface Science, 2007. 601(5): p. 1193-1204.

6. Davepon, B., J.W. Schultze, U. Konig and C. Rosenkranz, Crystallographic orientation of single grains of polycrystalline titanium and their influence on electrochemical processes. Surface & Coatings Technology, 2003. 169: p. 85-90.

7. Kudelka, S. and J.W. Schultze, Photoelectrochemical imaging and microscopic reactivity of oxidised Ti. Electrochimica Acta, 1997. 42(18): p. 2817-2825.

8. Park, C.J., M.M. Lohrengel, T. Hamelmann, M. Pilaski and H.S. Kwon, Grain-dependent passivation of surfaces of polycrystalline zinc. Electrochimica Acta, 2002. 47(21): p. 3395-3399.

9. Pilaski, M., T. Hamelmann, A. Moehring and M.M. Lohrengel, Impedance spectroscopy in micro systems. Electrochimica Acta, 2002. 47(13-14): p. 2127-2134.

10. Schreiber, A., J.W. Schultze, M.M. Lohrengel, F. Karman and E. Kalman, Grain dependent electrochemical investigations on pure iron in acetate buffer pH 6.0. Electrochimica Acta, 2006. 51(13): p. 2625-2630.

11. Lill, K.A., A.W. Hassel, G. Frommeyer and M. Stratmann, Scanning droplet cell investigations on single grains of a FeAlCr light weight ferritic steel. Electrochimica Acta, 2005. 51(5): p. 978-983.

12. Miyamoto, H., K. Yoshimura, T. Mimaki and M. Yamashita, Behavior of intergranular corrosion of < 011 > tilt grain boundaries of pure copper bicrystals. Corrosion Science, 2002. 44(8): p. 1835-1846.

13. Lee, S. and H.S. White, Dissolution of the native oxide film on polycrystalline and single-crystal aluminum in NaCl solutions. Journal of the Electrochemical Society, 2004. 151(8): p. B479-B483.

14. Binnig, G., C.F. Quate and C. Gerber, Atomic force microscope. Physical Review Letters, 1986. 56(9): p. 930-933.

15. Whitehouse, D.J., Surface characterization and roughness measurement in engineering. Photo-Mechanics, 2000. 77: p. 413-461.

16. Seo, J.H., J.H. Ryu, and D.N. Lee, Formation of crystallographic etch pits during AC etching of aluminum. Journal of the Electrochemical Society, 2003. 150(9): p. B433-B438.

17. Treacy, G.M. and C.B. Breslin, Electrochemical studies on single-crystal aluminium surfaces. Electrochimica Acta, 1998. 43(12-13): p. 1715-1720.

18. Wang, S.Y. and J.Q. Wang, Effect of grain orientation on the corrosion behavior of polycrystalline Alloy 690. Corrosion Science, 2014. 85: p. 183-192.

19. Zhang, J.M., M. Fei and K.W. Xu, Calculation of the surface energy of fcc metals with modified embedded-atom method. Chinese Physics, 2004. 13(7): p. 1082-1090.

20. Wen, Y.N. and H.M. Zhang, Surface energy calculation of the fcc metals by using the MAEAM. Solid State Communications, 2007. 144(3-4): p. 163-167.

21. Fu, B.Q., W. Liu and Z.L. Li, Calculation of the surface energy of fcc-metals with the empirical electron surface model. Applied Surface Science, 2010. 256(22): p. 6899-6907.

Chapter 6
Revealing the relationship between microstructure and electrochemical activity by gold-nanoplating[1]

In the previous chapter, the combination of AFM and EBSD was able to reveal some interesting features on the microstructural aspects of corrosion. It became clear that the dissolution rate of grains with specific orientations was also significantly influenced by the orientation of the neighboring grains. In this chapter, the electrochemical activity of a metal microstructure will be evaluated by an innovative concept, called gold-nanoplating. This technique is based on the electrochemical displacement of gold, where gold is deposited in the form of particles from aqueous solution on a polycrystalline metal surface of a less noble metal, which is in this work copper. With gold-nanoplating it becomes possible to demonstrate the differences in the electrochemical activity of grains and grain boundaries in polycrystalline metals on a mesoscale, i.e. with significantly improved statistics as compared to the combination of AFM and EBSD from chapter 5.

6.1 Introduction

An innovative concept is introduced to quantify the electrochemical activity of grains and grain boundaries in a polycrystalline copper sample. This method is based on the galvanic displacement of gold to the metal surface [1]. It is well known that that surface structure and surface heterogeneities have a strong influence on the adsorption process. This has been the topic of several studies in the 20th century [1-4]. In particular, various publications have been dedicated to the decoration of specific surface features and defects by the displacement deposition of gold [2, 3, 5, 6]. It has been observed that the gold atoms do not form a homogeneous film; instead they form small nuclei which accumulate preferentially at the surface defects. In the surface regions without defects or inhomogeneity's, the gold nuclei are statistically distributed [3].

[1]This chapter is based on the following publications: L. Lapeire, E. Martinez Lombardia, K. Verbeken, I. De Graeve, H. Terryn, L.A.I. Kestens, Structural dependence of gold deposition by nanoplating in polycrystalline copper, Journal of Materials Science 49 (2014) 3909-3916. **and** R. Gaggiano, E. Martinez Lombardia, I. De Graeve, L. Lapeire, K. Verbeken, L.A.I. Kestens, H. Terryn, Gold nanoplating as a new method for the quantification of the electrochemical activity of grain boundaries in polycrystalline metals, Electrochemistry Communications 24 (2012) 97-99. **and** L. Lapeire, E. Martinez Lombardia, K. Verbeken, I. De Graeve, H. Terryn, L.A.I. Kestens, Grain orientation dependent gold deposition by nanoplating of polycrystalline copper, *In preparation*.

In this chapter, high purity copper is brought into contact with a gold containing solution. The characterization of the gold-nanoplated metal substrate can provide important information on how the gold deposition is affected by the microstructural characteristics of the material, with specific focus on the grain orientations and grain boundary characteristics. The complementary use of EBSD for revealing the microstructural features, such as the crystallographic orientation, FE-SEM for imaging and EDX analysis for quantification of the deposited gold makes it possible to detect and even quantify differences in both grain and grain boundary activity.

6.2 Gold-nanoplating technique

The gold-nanoplating technique is based on the electrochemical (galvanic) displacement of gold onto the metal surface. The gold is deposited as particles from an aqueous solution on a copper substrate. The gold deposition on the copper surface is a redox process. Two reactions, as described below, take place simultaneously at the copper surface, namely the reduction of gold and the oxidation of copper:

Cu oxidation: $3Cu(s) \rightarrow 3Cu^{2+}(aq) + 6e^{-}$ ($E° = +0.337V$)

Au reduction: $2Au^{3+}(aq) + 6e^{-} \rightarrow 2Au(s)$ ($E° = +1.52V$)

Figure 6-1 provides a schematic representation of the deposition process.

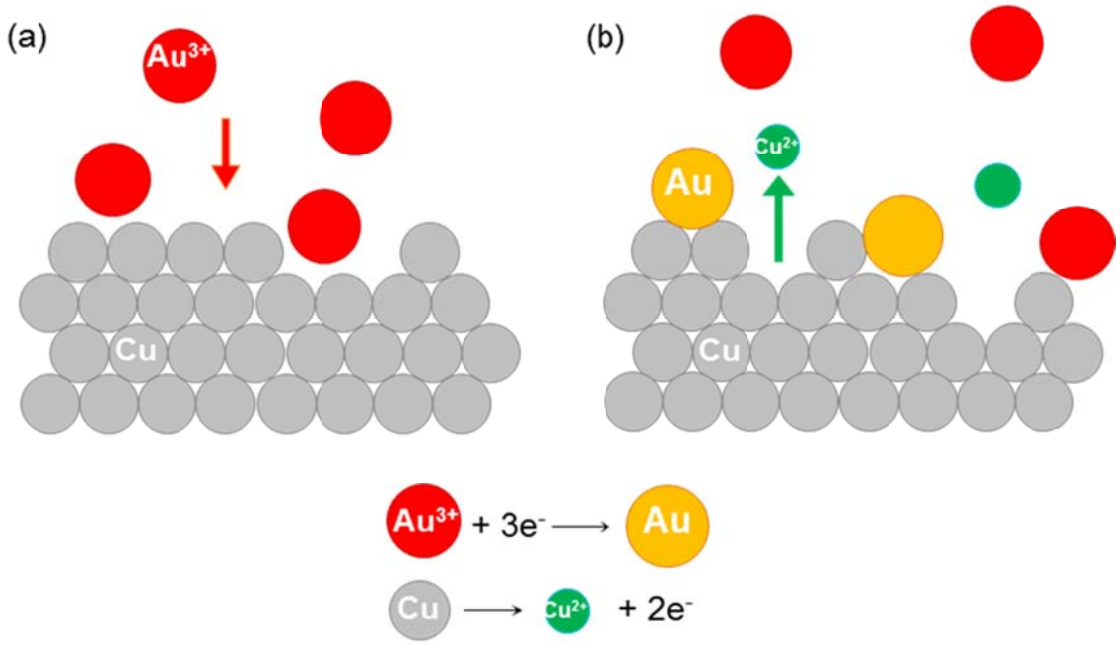

Figure 6-1: Schematic representation of the different steps of the gold-nanoplating process when depositing Au on a Cu substrate.

At first, Au^{3+} is diffusing from the bulk to the copper surface (Fig. 6-1a). At this surface, an Au^{3+}-Cu galvanic cell is formed [1]. Cu atoms oxidize, and the Au^{3+} reduces and subsequently deposits on the Cu surface (Fig. 6-1b). For every two gold atoms deposited on the metal surface three copper atoms are oxidized. It is expected that the onset of this electrochemical reaction is influenced by the various microstructural features which cause local differences in electrochemical activity and consequently in the amount of Au deposited. By optimizing the different electrochemical parameters of the gold/copper system, i.e. by changing the exposure time and concentration of the gold containing solution, it will become possible to let differences in electrochemical activity of grains and grain boundaries emerge from the material.

6.3 Determination of the grain boundary energy by gold-nanoplating

With gold-nanoplating, it becomes possible to reveal the difference in electrochemical activity between the different types of grain boundaries, i.e. between the special or CSL-type boundaries and the random boundaries. The concept of CSL boundaries was defined earlier in this work. The experimental results that are obtained on the grain boundary electrochemical activity of the different types of grain boundaries will be subsequently compared to both calculated and experimental literature predictions on grain boundary energy for the different types of grain boundaries.

6.3.1 Experimental details

6.3.1.1 Material processing

The material under investigation in this chapter is high purity cast copper that underwent a 75% hot rolling reduction in order to destroy the cast microstructure and provide a completely recrystallized microstructure, as was previously demonstrated in section 4.3.2. After annealing (800°C, 24 h) the material exhibits 50% of $\Sigma 3^n$ (n=1, 2, 3) CSL boundaries by length fraction, i.e. the fraction of $\Sigma 3^n$ boundaries with respect to the total length of high angle grain boundaries (misorientation angle above 15°), and an average grain size of 20 µm. The criterion used for classifying grain boundaries as CSL's was the more restrictive Palumbo-Aust criterion [7]. This criterion implies that the allowable angular deviation for a CSL boundary is $\Delta\theta \leq 15° \sum^{-5/6,}$ where θ is the misorientation angle. The copper samples were polished; both mechanical and electrolytic polishing was applied to reduce the substrate roughness. The average sample roughness after electropolishing was less than 1 nm.

6.3.1.2 Gold-nanoplating conditions

Gold particles were deposited on the copper surface by an immersion of 30 min in a non-stirred 1mM gold(III) chloride hydrate ($HAuCl_{4,}$ 99.999% purity) solution at room temperature. The pH of the gold solution was 4, permitting to study the bare copper surface without influence of its

native oxide layer. After the deposition, the samples were rinsed for 30 s with acetone and dried with pressurized air.

6.3.1.3 Data collection and processing

FE-SEM, EDX and EBSD were complementary used to correlate the microstructural characteristics of copper with the amount of deposited gold on the sample surface with particular attention to what happens at the grain boundaries.

Before gold nanoplating, the copper microstructure was characterized by electron backscatter diffraction (EBSD). The EBSD system is attached to an FEI® FE-SEM (Quanta) operated at 20 kV. Measurements were carried out with a step size of 2 µm and the orientation data were post-processed with the commercial orientation imaging software package OIM-TSL®. FE-SEM images of the surface after the gold deposition were used as a guide for the EDX mappings. For acquiring the gold distribution images of the Cu nanoplated surface, the Au-M lines were scanned at an acceleration voltage of 15 kV. From this gold distribution map, the amount of gold at specific grain boundaries is quantified with the Java-based image processing program ImageJ®. With this program, it becomes possible to integrate the intensity of the Au-M signal across every boundary, which gives a general idea of the grain boundary electrochemical activity for that specific boundary. In total, an area consisting of 100 grains with all corresponding 649 grain boundaries was evaluated in detail.

6.3.2 Gold-nanoplating and grain boundary energy

The gold nanoplating technique is based on a redox reaction. Local anodic/cathodic reactivity differences at the metal surface will provoke very local reduction, and provoke deposition/plating of gold metal cations on the cathodic sites, while the anodic sites show copper oxidation. The higher electrochemical activity at the grain boundaries results in an increased concentration of gold deposited at the grain boundaries, as clearly illustrated in figure 6-2a. The FE-SEM images shown in this figure indicate that a gold covered grain boundary network results from the gold-nanoplating, as the gold is clearly visible as white spots on the dark background of the copper surface. In the higher magnification images (Fig. 6-2b and 6-2c) the predetermined mechanism of the gold nanoplating is demonstrated. The gold is preferentially reduced and thus deposited at the grain boundaries. Meanwhile, the copper is oxidized at the same grain boundary. This results in a groove on the copper surface, which is then filled with the gold particles.

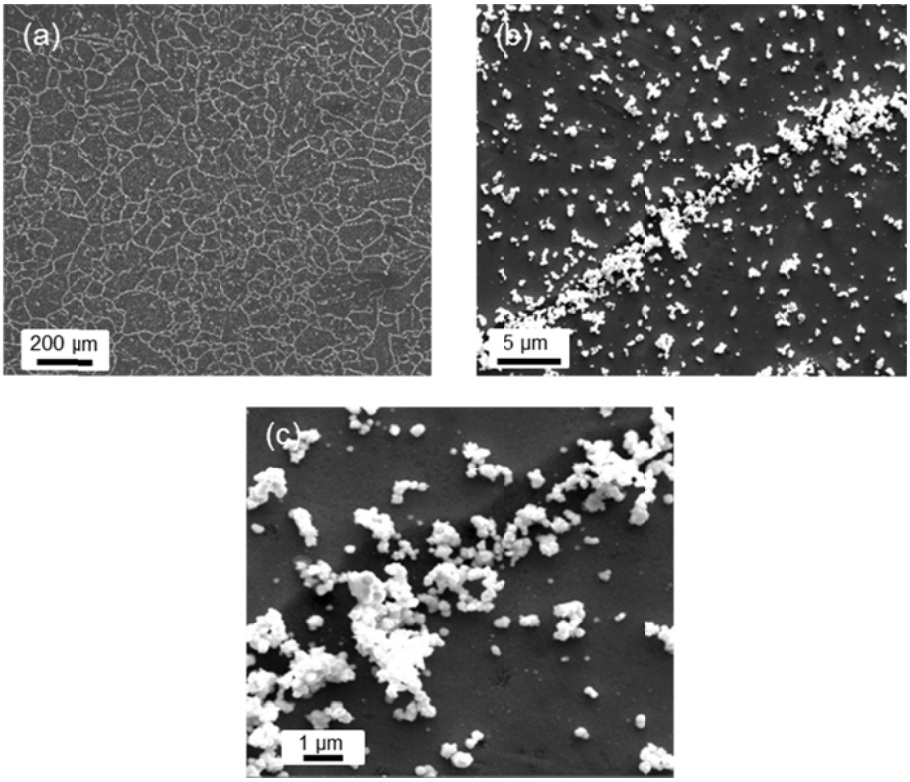

Figure 6-2: (a-c) FE-SEM view (SE) of a gold-nanoplated Cu surface at different magnifications, illustrating the increased Au concentration at the grain boundaries.

After a careful evaluation of the gold nanoplated Cu surface, clear differences in the amount of deposited gold on the different boundaries are observed. These differences in gold concentration could be attributed to the difference in electrochemical activity of these boundaries, which may be associated with their grain boundary energy. If this would be the case, copper atoms at the grain boundaries with higher energy will dissolve faster than at the ones with lower energy, resulting in different rates of gold reduction for the different types of grain boundaries. Consequently, after a specific time of immersion in the $HAuCl_4$ solution, different gold concentrations at the different grain boundaries will be obtained. Therefore, it will be evaluated here, by determining the amount of gold present on specific grain boundaries, whether a correlation can be made between the predicted literature values on grain boundary energies and the gold deposition on these grain boundaries.

6.3.3 Gold-nanoplating to evaluate differences between random and special boundaries

As already shown in figure 6-2, not all grain boundaries are covered with the same quantity of gold. In this section, this observation is evaluated in more detail in order to reveal the differences in electrochemical reactivity between CSL-type and random high angle grain boundaries.

Figure 6-3a shows the inverse pole figure map (IPF). By marking the surface with a specific scratch a unique site could be identified and investigated throughout the entire experiment. The image quality map of figure 6-3b denotes the different types of boundaries. Blue lines indicate random high angle boundaries and red lines indicate all $\Sigma 3^n$ boundaries (n = 1, 2, 3). A FE-SEM top view of the copper sample after immersion in the $HAuCl_4$ solution is depicted in figure 6-3c. The increased electrochemical activity at some grain boundaries results in an increased concentration of gold deposited at these boundaries.

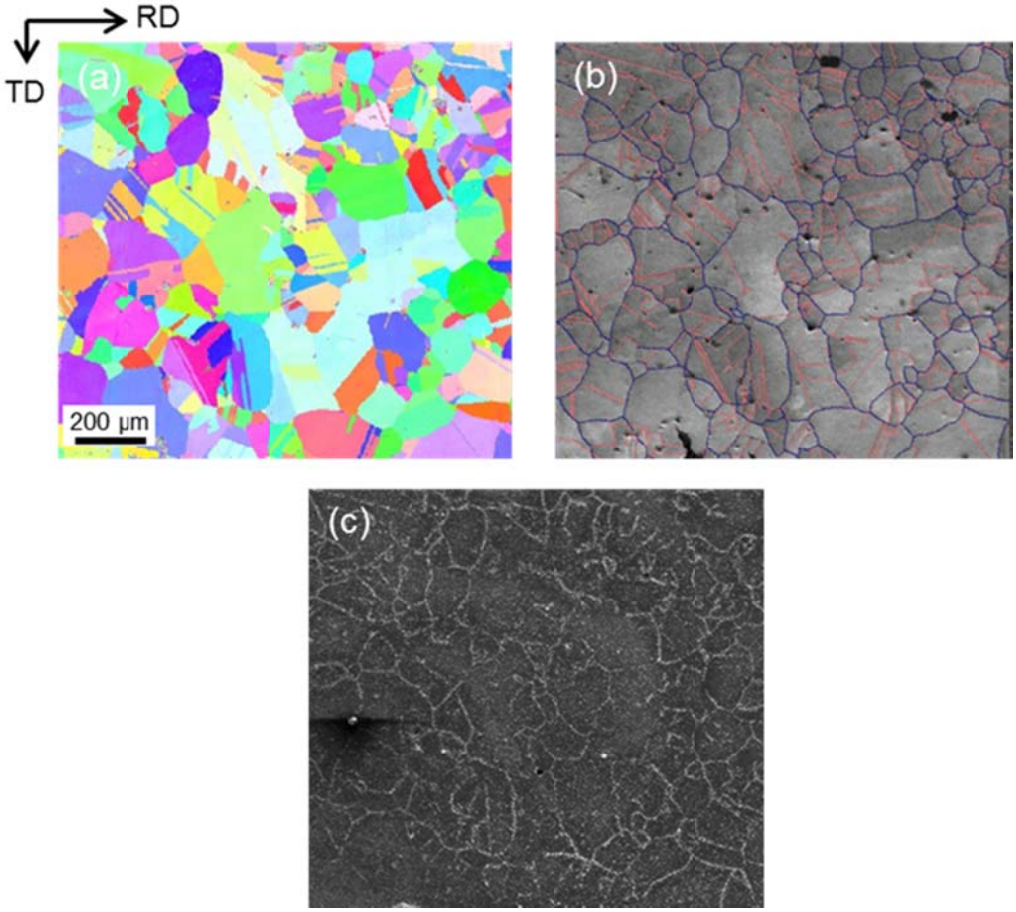

Figure 6-3: (a) Inverse pole figure (IPF) map of the Cu surface before gold-nanoplating. (b) Image quality (IQ) map with indication of different types of boundaries. Blue lines denote random high angle boundaries (>15°); red lines denote $\Sigma 3^n$ boundaries (n= 1, 2, 3). (c) FE-SEM view (SE) of the Cu sample on the same area after 30 min of immersion in $HAuCl_4$.

To analyze the results of the gold deposition at the grain boundaries in more detail, two magnified images will be discussed (Fig. 6-4 a-d). These images are representative for the entire microstructure under evaluation.

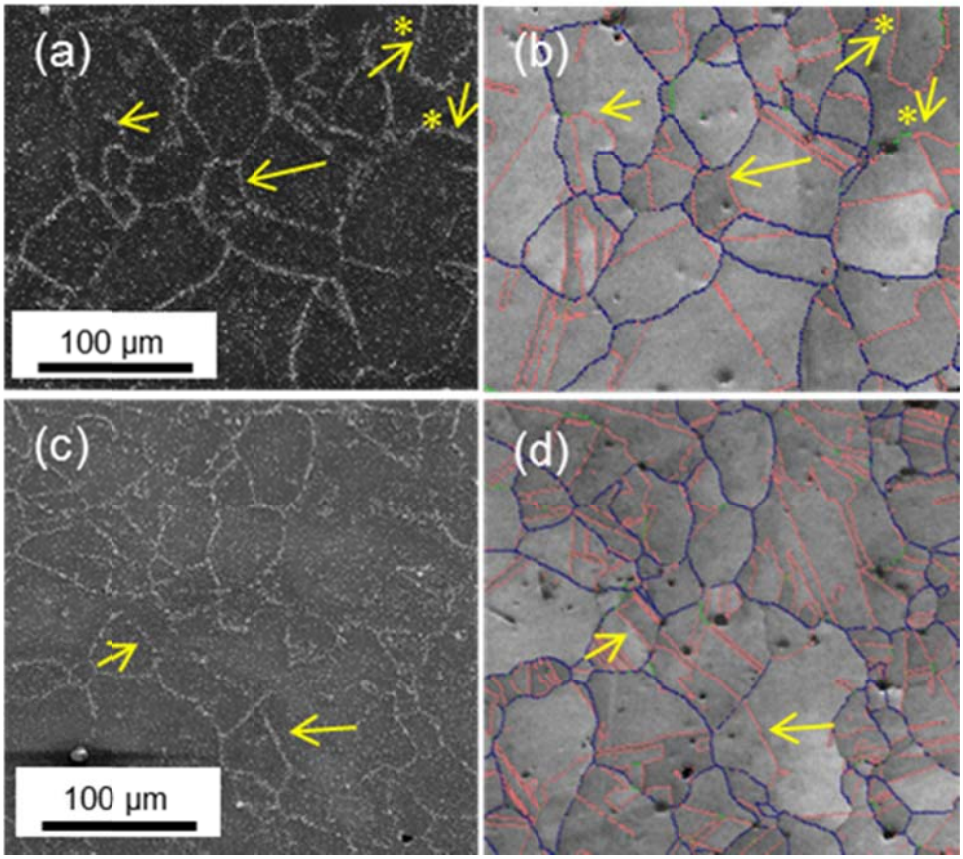

Figure 6-4: (a, c) Detailed FE-SEM view (SE) on two different areas of the Cu sample after 30 min of immersion in $HAuCl_4$. (b, d) Corresponding IQ map; random boundaries, Σ3 boundaries and the other potential special boundaries ($3 < \Sigma \leq 27$) are indicated by blue, red and green lines, respectively.

When comparing the FE-SEM view in figure 6-4a with the image quality map in figure 6-4b, which depicts the different types of boundaries, a number of observations can be made. First, the deposition of gold on the random grain boundaries (blue lines) is clearly visible. This is an indication for the higher electrochemical activity of these random grain boundaries in comparison to both the grain interior and to some of the CSL boundaries. Looking at the potentially special boundaries (Σ3-27), indicated in red and green, some remarkable features were observed. First of all, due to their low frequency in the sample, non Σ3 were no longer considered. However, with respect to the Σ3 boundaries, only on the Σ3 boundaries indicated by the yellow arrows a gold deposition was observed. The absence of gold on most Σ3 boundaries proves their specific behavior: i.e. their higher resistance to oxidation, i.e. to the gold-copper redox reaction.

A more detailed investigation of the micrographs revealed numerous long and parallel-sided Σ3 boundaries (Fig. 6-4). Most likely these are coherent twins, as they are characterized by their parallel-sided appearance [8]. It is well known that because of their low free volume, the coherent twin boundaries, with the GB plane parallel to the {111} crystal plane, will exhibit the higher corrosion resistance [9]. This specific property of a coherent twin boundary is here experimentally demonstrated by the gold-nanoplating technique. However, coherent twins are only a subset of all possible types of Σ3 boundaries. Other Σ3 boundaries are characterized by boundary planes of different inclination, which most likely exhibit different (higher) grain boundary energies. The other Σ3 boundaries in copper, ordered by increasing energy, are: asymmetrical tilt boundaries with a {112} grain boundary plane and also called the incoherent twin boundaries, twist boundaries and Σ3 boundaries with irrational grain boundary planes [10]. This literature information is in good agreement with the results obtained via the gold-nanoplating technique. In the image quality map of figure 6-4b, yellow arrows indicate some Σ3 boundaries that are covered with gold, indicating their higher electrochemical activity and their higher energy.

However, not all the designated Σ3 grain boundaries are decorated with the same amount of gold, indicating the different nature of the Σ3 boundaries. In figure 6-4b, two Σ3 boundaries are marked with an asterisk because of the substantial amount of gold deposited on them. No significant difference between the random high angle grain boundaries and these Σ3 boundaries was observed after an immersion for 30 min in the gold solution. This observation might be related to the fact that these are Σ3 boundaries with irrational boundary planes, which have a similar energy to that of a non-CSL boundary. Indeed, regardless of the periodic coincidence relationship between the lattices of the neighboring grains, there is no good fit at this type of boundary [9].

In figure 6-4c and 6-4d, all observations made so far were confirmed, and, in addition, they were also verified in other regions throughout the sample. The observations discussed so far were confirmed throughout the complete surface as again almost no gold was present on the parallel (i.e. coherent) Σ3 boundaries. The yellow arrows indicate also here Σ3 boundaries with significant gold decoration. Although these boundaries seem to have a straight appearance, the gold-nanoplating suggests a non-periodic structure of their boundary planes. This was verified and appeared to be in agreement with the data obtained by EBSD. In the TSL-OIM software, it is possible to observe the trace of the boundary and check whether or not it is co-planar with the twinning plane. In the two highlighted boundaries in figure 6-4c and 6-4d, the twinning planes were not aligned with the boundary planes, suggesting non-coherent Σ3 boundaries.

The presented results indicate the potential of the gold nanoplating technique: a qualitative assessment of the presence of gold on the grain boundaries clearly demonstrated the different

behavior between CSL boundaries and random high angle grain boundaries. Moreover, within the set of CSL boundaries, a correlation between the characteristics of the grain boundary plane and the gold deposition was demonstrated as well. The next section will elaborate this in more detail as a quantification of the amount of gold deposited will be correlated with the grain boundary energy.

6.3.4 Quantification of grain boundary electrochemical activity based on gold-nanoplating

After gold nanoplating, different EDX elemental mapping of the Au-M line are carried out on various places on the Cu surface. Figure 6-5a shows one of these mappings where the green pixels represent the Au found on the copper surface.

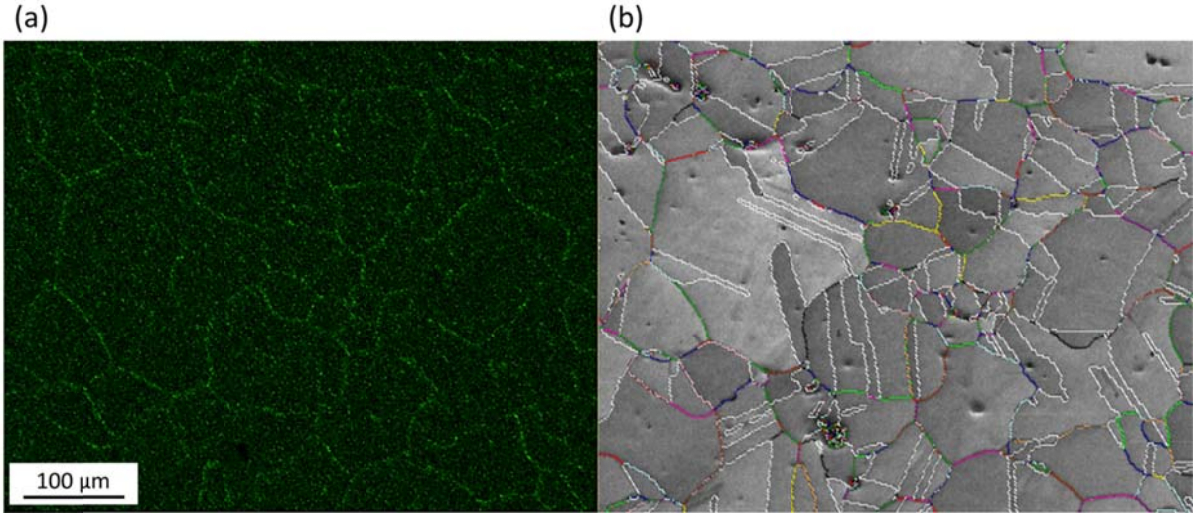

Figure 6-5: (a) EDX elemental mapping of the Au-M line (green) on the Cu sample after 30 min of immersion in $HAuCl_4$. (b) Corresponding IQ map with indication of different types of grain boundaries. Orange and pale green boundaries represent low angle grain boundaries with misorientation angles between 5°-10° and 10°-15°, respectively. All other colors represent high angle boundaries, divided into intervals of five degrees misorientation. White boundaries represent Σ3 boundaries.

With the use of the Java-based image processing program ImageJ® the intensity of the Au-M signal is integrated inside every grain and across every boundary. To identify every grain and grain boundary, the corresponding EBSD data, represented by the IQ map with indication of the different grain boundaries (Fig. 6-5b), is used. In that way, it becomes possible to assign a certain gold intensity to every grain and grain boundary, and associate this to its specific orientation or misorientation characteristics. With the present parameters used for the gold nanoplating experiment, the gold intensity inside the different grains showed a rather uniform, low and constant distribution. Therefore, the mean value of the gold intensity in the grain

interior is considered as background when evaluating the gold deposition at the grain boundaries. Consequently, the corresponding average gold signal of all grain interiors is subtracted from the integrated gold intensity values at the grain boundaries. At the grain boundaries, clear differences in gold intensities were observed for the different grain boundaries. In figure 6-6, these differences are shown for a total of 649 boundaries. In addition, the spread on the obtained data is indicated as well on the figure.

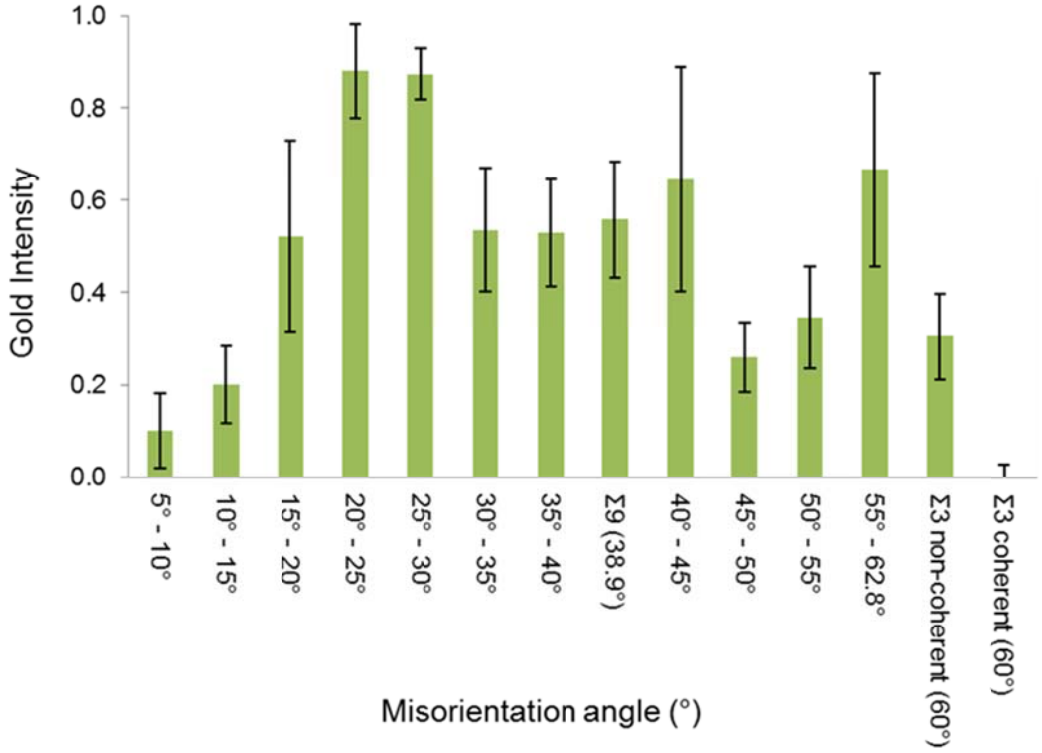

Figure 6-6: Gold intensity versus grain boundary misorientation angle. Analysis based on data for 649 grain boundaries.

In figure 6-6 the gold intensity is plotted against the grain boundary minimum misorientation angle, irrespective of the misorientation axis. The intensity of the pixels, corresponding to the local Au concentration, was rescaled between 0 and 1, representing the minimum and maximum values, respectively. Some CSL boundaries, namely coherent and non-coherent Σ3 and Σ9 boundaries are shown separately in this figure. In this way, a correlation is established between the gold deposition, which is considered to be a measure for the grain boundary activity of the different grain boundaries, and the misorientation angle of these specific boundaries. As mentioned above, the results of this measured grain boundary activity might be

considered to give an indication on the grain boundary energy and are therefore linked with literature information on the grain boundary energy. Both experimentally determined and modeling results from molecular dynamics simulations will be taken into account.

For the low angle grain boundaries, the results from the quantitative gold measurements are in good agreement with the Read-Shockley model [11]. This model is well established both experimentally and theoretically and describes the steep rise in energy from the low to high angle boundaries with increasing misorientation angle (Fig. 6-7).

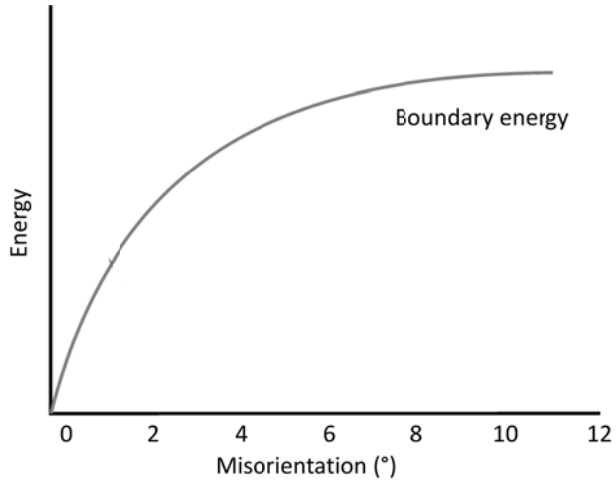

Figure 6-7: Grain boundary energy as a function of the misorientation angle for LAGBs according to the Read-Shockley model [11].

According to the conventional grain boundary theory, the transition from low to high angle grain boundaries occurs in the range of 10° to 20° misorientation. Experiments determining grain boundary energies [11, 12] suggest a transition angle from the low to the high angle domain near 15°, while evidence obtained by high resolution microscopy of distinguishable dislocations has been observed for grain boundaries with misorientation angles up to 20° misorientation [13]. In the gold nanoplating experiments on the copper surface, a steep rise in gold intensity is observed up to 20° misorientation, suggesting that the transition from low to high angle boundaries in copper occurs at a misorientation angle close to about 20°.

The evolution of the grain boundary energy in the high angle domain is still under debate in literature. Our gold nanoplating measurements show that the highest gold intensity is visible between 20° and 30°, which is followed by lower gold intensities at higher angles. This observation corresponds with the selective grain growth theory proposed by Hayakawa and Szpunar [14, 15]. In their recrystallization model, they claim that the grain boundary energy is the highest for boundaries between 20° and 30° irrespective of the misorientation axis due to the Read-Shockley equation.

For boundaries with misorientation angles between 30° and 55° a decrease in gold intensity or grain boundary activity is observed. When considering misorientations higher than 55°, an increase in gold deposition, and consequently in the grain boundary activity, became apparent. Gruber et al. [16, 17] suggested and demonstrated via Monte Carlo simulations an inverse proportionality between grain boundary energy and the frequency of this specific grain boundary in their simulated sample. Although this relationship is still under debate, a similar relationship can be seen in the nanoplated copper sample. According to Gruber et al. the increasing population of grain boundaries with misorientation angles between 30 and 50° can be matched with lower grain boundary energy. This correlates very well with the lower gold deposition in the present work.

The results on the quantification of the gold nanoplating confirm the conclusions from the previous section on the electrochemical activity of the Σ3 boundaries. Although the EBSD measurements are performed on a 2D-section and consequently not allow a complete description of the grain boundary plane, the alignment of the surface traces of the twinning planes with the trace of the boundary provides an indication of coherency for a Σ3 boundary [8]. Therefore, the numerous long and parallel-sided Σ3 boundaries are catalogued as coherent Σ3 boundaries. The integrated gold intensity across these coherent Σ3 boundaries is not significantly different from the gold intensity at the grain interiors. This indicates a similar electrochemical activity for both the grain interior and the coherent Σ3 boundaries, confirming the low grain boundary activity of the coherent Σ3 boundaries [18]. All data on the other Σ3 boundaries are summarized in figure 6-6 as 'Σ3 non-coherent'. The gold intensity of these boundaries, on the one hand, significantly higher than for the coherent twin boundaries, but, on the other hand, also significantly lower as compared to the other boundaries in the corresponding grain boundary misorientation interval 55°-62.8°. This can be explained by the fact that the non-coherent Σ3 boundaries exhibit lower grain boundary activities than random high angle grain boundaries. The large observed difference in gold deposition determined by the coherency of the Σ3 boundaries reflects the significant role that the boundary plane orientation plays in the grain boundary energy. Also, for the different Σ3 boundaries the theory of the inverse correlation between boundary energy and boundary population [16, 17] seems to remain valid. The coherent Σ3 boundaries have a boundary length fraction of 43.3% as could be expected from their very low gold intensities. For the non-coherent Σ3 boundaries, a boundary length fraction of 3% is observed, which is similar to the length fraction observed for random high angle grain boundaries with similar gold intensities.

In this copper sample, the Σ9 boundary was evaluated as a separate boundary. However, no difference was observed in gold intensity for a Σ9 boundary, as compared to random high angle grain boundaries with similar misorientation angles. Olmsted et al. [19, 20] calculated grain boundary energies for different fcc metals based on embedded-atom method interatomic

potentials and they also found grain boundary energies for different types of Σ9 boundaries that were in the same range as for random high angle boundaries with similar misorientations angles.

As a conclusion of this section, the potential of the gold-nanoplating technique for quantifying the grain boundary activity and energy was demonstrated by linking the amount of deposited gold on the polycrystalline copper surface with already established literature data on grain boundary energy and the properties of special boundaries such as ∑3 boundaries. This clearly supports the applicability and potential of the gold nanoplating technique as it provides not only a reliable measurement on the grain boundary activity as well as on the grain boundary energy.

6.4 Gold-nanoplating for different grain orientations

Whereas in the previous section a correlation was made between the grain boundary characteristics and the amount of deposited gold, the present section aims at finding a correlation between the amount of deposited gold and the grain orientation. It will be verified whether gold-nanoplating allows revealing the difference in electrochemical response for some predetermined orientations. To be able to compare the experimental results on grain orientation dependent electrochemical behavior with literature and with our previously discussed data, the following low indexed orientations are chosen: <100>// ND, <111>// ND and <110>// ND.

6.4.1 Experimental details

6.4.1.1 Material

The same material with the same thermomechanical processing as described in section 6.3.1.1 was used here.

6.4.1.2 Gold-nanoplating conditions

Gold particles were deposited on the copper surface by an immersion for 15 min in a non-stirred 2 mM gold(III) chloride hydrate ($HAuCl_4$, 99.999% purity) solution at room temperature. The pH of the gold solution was lower than 4, permitting to study the bare copper surface without influence of its native oxide layer. After the deposition, the samples were rinsed for 30 s with acetone and dried in pressurized air.

6.4.1.3 Data collection and processing

FE-SEM and EBSD were complementary used to correlate the microstructural characteristics of copper with the amount of deposited gold on the sample surface with particular attention to what happens at the grain interiors.

Before gold-nanoplating, the copper microstructure was characterized by electron backscatter diffraction (EBSD). The EBSD system is attached to an FEI® FE-SEM (Quanta) operated at 20 kV. Measurements were carried out with a step size of 2 μm and the orientation data were post-processed with the commercial orientation imaging software package OIM-TSL®. The orientation images were represented in this study as inverse pole figure (IPF) maps, i.e. the color of each grain represents the crystal orientation that is parallel to the sample surface normal, which is commonly denominated as the sample ND direction. FE-SEM images of the surface after the gold deposition were used to acquire the amount of gold at specific grains. This gold deposition, seen as white spots on a dark background, is quantified with the Java-based image processing program ImageJ®. With this program it becomes possible to integrate the intensity of the deposited gold across every grain, which is correlated with the electrochemical activity for that specific grain. In total, 113 grains were fully characterized. Several low index-planes were studied and a maximum deviation of 15 degrees was allowed from the ideal orientation in order to consider a specific grain belonging to the low-index plane under consideration.

6.4.2 Gold-nanoplating and grain dependent electrochemical activity

The concept of the gold-nanoplating technique was already described in detail above. The high electrochemical activity at the grain boundaries results in a high concentration of gold deposited at the grain boundaries, as illustrated in figure 6-8, where the gold covered grain boundary network is visualized, as the gold is clearly visible as white spots on the dark background of the copper surface. The gold is preferentially reduced and thus deposited at the grain boundaries; meanwhile the copper is oxidized at the same grain boundary. After gold-nanoplating, the grain boundary can be expected to become electrochemically inactive as it is covered with gold. After deactivation of the grain boundaries, the gold will start to deposit on the electrochemically most active grain orientations. A careful evaluation of the secondary electron (SE) image of the gold-nanoplated surface (Fig. 6-8) reveals indeed, under the present gold-nanoplating conditions, a clear difference in gold concentration on the different grain orientations. Correlation with the EBSD results will allow correlating the amount of deposited gold with the crystallographic orientations of the different grains.

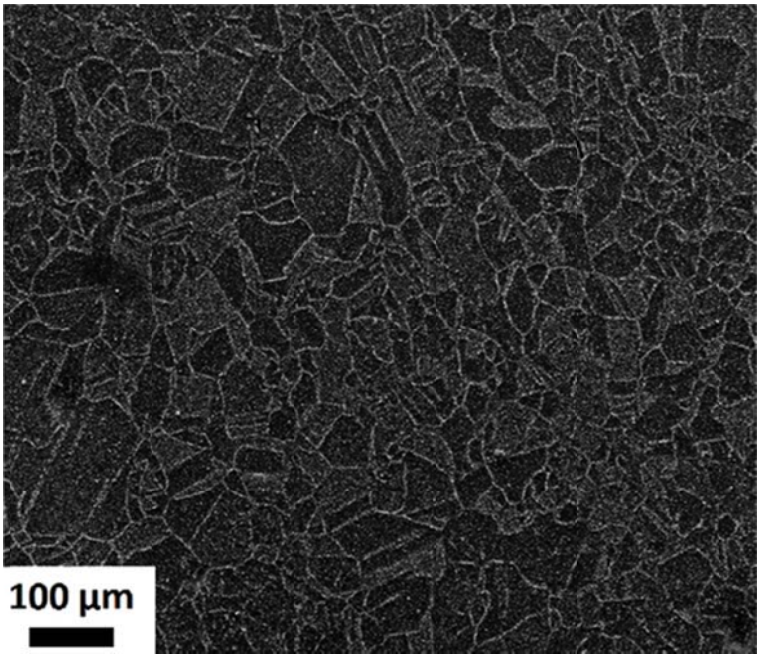

Figure 6-8: FE-SEM view (SE) of a gold-nanoplated Cu surface.

Similarly as for the grain boundaries, the difference in gold concentration can be attributed to the difference in electrochemical activity of the different grain orientations. Therefore, copper ions will go faster into solution for grains with a higher activity than for those with lower electrochemical activity, provoking different rates of gold reduction for the different grain orientations. This will result in different gold concentrations at different grains after a specific immersion time in the $HAuCl_4$ solution. By evaluating the amount of gold on a specific grain orientation, it becomes possible to assess the differences in electrochemical grain activity for the different grain orientations.

6.4.3 Quantification of the grain orientation dependent electrochemical activity by gold-nanoplating

As already demonstrated in figure 6-8, it can be seen that not all grains are covered with the same quantity of gold. If a specific gold intensity could be assigned to a specific grain and be correlated with its crystallographic orientation, it would be possible to quantify the electrochemical activity of that specific orientation.

Figure 6-9a shows the combined inverse pole figure (IPF) and image quality (IQ) map of a Cu sample before gold-nanoplating. By marking the sample, a unique site could be identified throughout the entire experiment. A FE-SEM top view at the same place of the copper sample after immersion in the $HAuCl_4$ is depicted in figure 6-9b. By combining the IPF/IQ map with the SE image, it is possible to identify the different grain orientations. Because of the higher electrochemical activity of the grain boundaries and consequently corresponding higher gold

deposition, this is relatively straightforward. With use of the Java-based picture processing program ImageJ® the intensity of the gold deposition (seen as white spots) is integrated at the interior of every grain based on the grayscale values of the SE image. The intensity of the pixels, corresponding to the local gold concentration, was rescaled between 0 and 1, representing the minimum and the maximum values, respectively. In this way a correlation is established between the gold deposition, which is considered to be a measure for the electrochemical activity of the different grains and their orientation. Since literature information on grain dependent electrochemical activity is limited, the results on this measured grain activity will be linked with literature information on orientation dependent surface energy. Both experimentally determined and modeling results from molecular dynamics simulations will be used for that purpose. The limited set of data available from literature is another reason why only grains with low indexed planes are examined. A total of 113 grains will be examined in detail. For this set of grains 38 are assigned to the <111>// ND orientation, 33 to <100>// ND and 42 are <110>// ND grains.

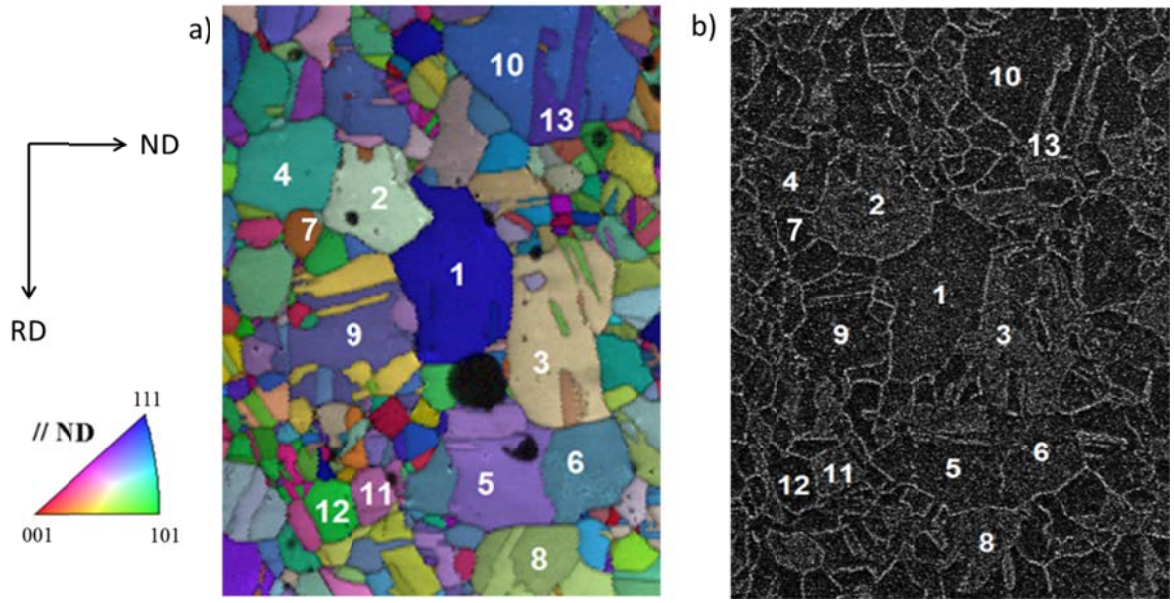

Figure 6-9: (a) Combined IPF/IQ map of the Cu surface before gold-nanoplating. (b) Corresponding FE-SEM view (SE) of the Cu sample after 15 min of immersion in 2mM $HAuCl_4$.

6.4.4 Electrochemical activity of <100>// ND, <111>// ND and <110>// ND oriented grains

In this section the experimentally determined gold intensity after gold-nanoplating of polycrystalline copper for the three previously mentioned low index orientations is discussed and compared with literature data.

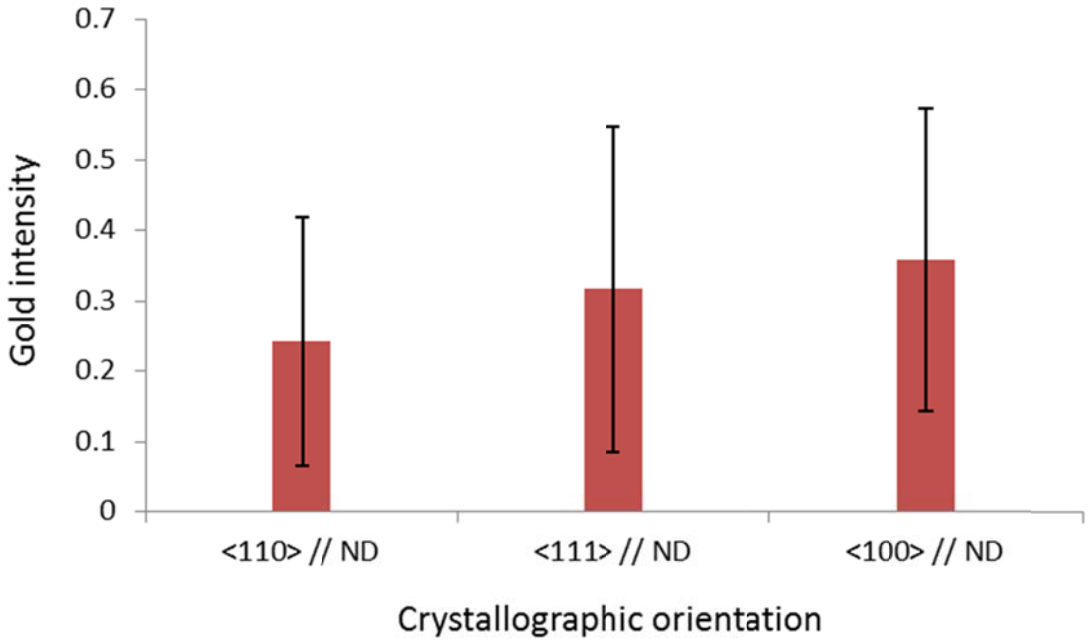

Figure 6-10: Average gold intensity for 42 <110>// ND grains, 38 <111>// ND grains and 33 <100>// ND grains after 15 min. immersion in 2 mM $HAuCl_4$.

In figure 6-10, the average gold intensity of 42 <110>// ND, 38 <111>// ND grains and 33 <100>// ND grains is plotted after gold-nanoplating. The results suggest that the electrochemical activity of the <110>// ND oriented grains (average gold intensity = 0.24) is lower compared to the electrochemical activity of the <111>// ND (average gold intensity = 0.32) and the <100>// ND (average gold intensity = 0.36) grains. However, it must also be mentioned that the scatter on the obtained results is relatively high. Therefore, the <111>// ND and the <100>// ND oriented grains are considered to have here a quite similar electrochemical activity.

As suggested in chapter 5, a possible explanation might be found by correlating the observed electrochemical activity with calculated results on the surface energy from literature. For the low-index planes the ranking of the surface energies in copper was reported to be (111) < (100) < (110) [21-23]. The low surface energy of the (111) plane suggests a higher gold deposition after gold-nanoplating [24]. This because lower surface energy implies that less energy is needed to remove a one-atom thick layer of surface. This is in reasonable agreement with the present observations. However, no clear difference in electrochemical behavior is seen between the <100>// ND and <111>// ND oriented grains. The results of the gold-nanoplating are therefore not completely in agreement with some experimental results on electrochemical behavior in fcc metals that were reported in literature. For example, Lee et al [25] investigated the dissolution rate in Al and their results indicated that this dissolution rate depends upon the

surface orientation in the order: (111) > (110) > (100). Whereas, we also observe the highest dissolution rate for <111>//ND oriented grains, the clear differences between the (111) and (100) planes as reported by Lee et al was not confirmed in our work.

A striking observation, when looking at the gold deposition on the different low-index planes, is the large variations in the average gold deposition for each type of grain orientation. A possible explanation is the suggestion that not only the grain orientation has an influence on the corrosion behavior, but that the orientation of the surrounding grains plays an important role as well. In chapter 5, the biggest difference in electrochemical behavior is seen when a <111>// ND oriented grain is next to a <100>// ND oriented grain. After the gold-nanoplating experiment in the polycrystalline copper sample, the grains with the largest difference in gold deposition surrounding each other were monitored throughout the entire sampled area.

Figure 6-11 shows the combined IPF/IQ map together with the corresponding SE map of one of the positions on the sample surface where neighboring grains show the largest difference in amount of deposited gold with respect to each other. Grain B (<111>// ND) has the highest gold deposition (gold intensity = 1), whereas grain A (<100>// ND) has the lowest gold deposition (gold intensity = 0) of the entire sample. Also on other places the same observations are done, the largest differences in gold deposition between neighboring grains are observed when a <100>// ND grain is next to a <111>// ND grain. These results are in good agreement with our previous findings in chapter 5 where the dissolution behavior of different grains was monitored by combining AFM and EBSD. The present observations after gold-nanoplating not only confirm the results of our previous research, but it also explains the large variation of the amount of deposited gold for the different low index planes. As indeed, the average gold deposition on the <100>// ND grains is 0.36, but when this grain is lying next to a <111>// ND grain the gold deposition is 0. This again nicely illustrates the electrochemical effect of the surrounding grains on the corrosion behavior of an individual grain. The fact that neighboring grains affect the electrochemical behavior of an individual grain is probably not only present in the case of neighboring <001>// ND and <111>// ND grains, and might explain the large scatter in the data. However, for other grain combinations the effect might be less outspoken and therefore, more difficult to identify.

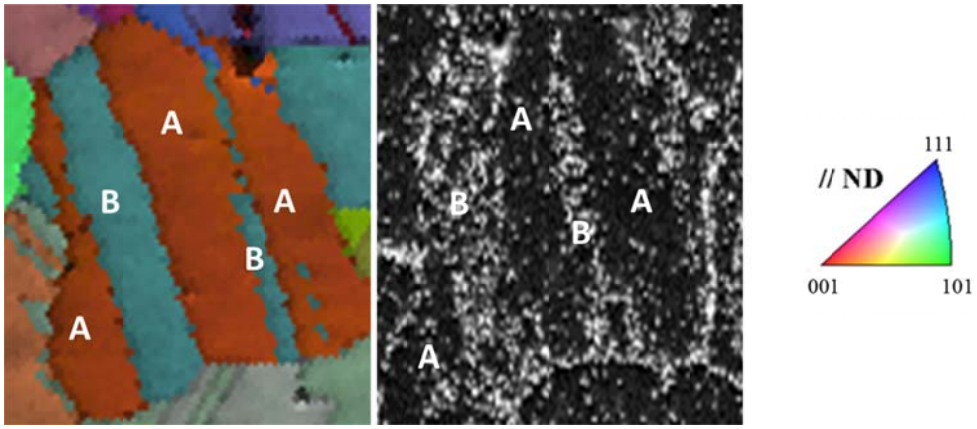

Figure 6-11: (a) Combined IPF/IQ map and (b) corresponding FE-SEM view (SE) of the neighboring grains which show the largest difference in gold deposition, with grain A having a <100>// ND orientation and grain B a <111>// ND orientation.

6.5 Conclusions

In this chapter, the applicability and potential of the gold nanoplating technique, both qualitatively and quantitatively, is demonstrated on high purity copper. This technique is based on the electrochemical displacement of gold, where the gold is deposited from an aqueous solution on the copper surface. After gold deposition, the complementary use of EBSD and FE-SEM appears to be particularly well suited to detect differences in the electrochemical activity of grains and grain boundaries during the Au-Cu redox process occurring at the Cu surface.

In the first part of this chapter, the gold-nanoplating technique is used to monitor differences in the electrochemical activity of different types of grain boundaries. It became possible to separate the so-called special or CSL-type boundaries from random high angle grain boundaries in an efficient way. With the use of EDX quantitative differences in the amount of deposited gold can be observed. As these differences in gold concentration seem to be related to the grain boundary energy, gold nanoplating provides clear experimental data on differences in grain boundary energy throughout the material. The described results for the quantified gold deposition on various types of grain boundaries in polycrystalline copper are indeed consistent with both calculated as experimental literature predictions on grain boundary energy.

Secondly, the grain orientation dependent electrochemical activity of pure copper was investigated by means of gold-nanoplating. In this study, the focus is on three low-indexed orientations, namely <001>// ND, <110>// ND and <111>// ND oriented grains. The results suggest that <111>// ND and <100>// ND oriented grains have a higher electrochemical activity compared to the <110>// ND grains. However, a large variation in the electrochemical activity is observed for similarly oriented grains. Consistent with the results obtained in chapter 5, the

gold-nanoplating technique used in this chapter confirms a clear deviating electrochemical behavior when <111>// ND oriented grains are adjacent to <100>// ND grains. This can explain the large variations in the amount of deposited gold between similarly oriented grains, as the orientation of the neighboring grains can indeed play a decisive role in the electrochemical behavior of that specific grain.

The trends observed in this chapter and in chapter 5 reveal some interesting features of the local electrochemical behavior of a material and how this is correlated to microstructural features such as grain orientation and grain boundary character. Advanced local electrochemical techniques offer an interesting next step to confirm the observations made so far. Therefore, in the next chapter, both scanning electrochemical microscopy (SECM) and in situ electrochemical scanning tunneling microscopy (EC-STM) will be used to evaluate the local electrochemical behavior on a microscopic level.

6.6 References

1. Ragoisha, G.A., Selective metal deposition on metal-semiconductor nanostructures. Vacuum, 1998. 50(1-2): p. 69-71.

2. Coutts, M.D. and A.G. Revesz, Decoration of semiconductor surfaces for electron microscopy by displacement deposition of gold. Journal of Applied Physics, 1966. 37(8): p. 3280-3288.

3. Bethge, H., Electron microscopic studies of surface structures and some relations to surface phenomena. Surface Science, 1965. 3(1): p. 33-40.

4. Rhead, G.E., Surface defects. Surface Science, 1977. 68(1): p. 20-38.

5. Sayed, S.Y., F. Wang, M. Malac, P. Li, D. Wang and J. Buriak, Preferential face deposition of gold nanoparticles on silicon nanowires by galvanic displacement. Crystengcomm, 2012. 14(16): p. 5230-5234.

6. Magagnin, L., R. Maboudian and C. Carraro, Gold deposition by galvanic displacement on semiconductor surfaces: Effect of substrate on adhesion. Journal of Physical Chemistry B, 2002. 106(2): p. 401-407.

7. Palumbo, G., K.T. Aust, E.M. Lehockey, U. Erb and P. Lin, On a more restrictive geometric criterion for "special" CSL grain boundaries. Scripta Materialia, 1998. 38(11): p. 1685-1690.

8. Kumar, M., A.J. Schwartz and W.E. King, Microstructural evolution during grain boundary engineering of low to medium stacking fault energy fcc materials. Acta Materialia, 2002. 50(10): p. 2599-2612.

9. Henrie, A.J., B.L. Adams and R.J. Larsen, Creating a model for percolation of grain boundaries in polycrystalline materials, in Textures of Materials, Pts 1 and 2, D.N. Lee, Editor. 2002, Trans Tech Publications Ltd: Zurich-Uetikon. p. 419-424.

10. Randle, V. and P. Davies, Deviation from reference planes and reference misorientation for Sigma 3 boundaries. Interface Science, 1999. 7(1): p. 5-13.

11. Read, W.T. and W. Shockley, Dislocation Models of Crystal Grain Boundaries. Physical Review, 1950. 78(3): p. 275-289.

12. Brandon, D.G., Structure of high-angle grain boundaries. Acta Metallurgica, 1966. 14(11): p. 1479-1485.

13. Randle, V., Twinning-related grain boundary engineering. Acta Materialia, 2004. 52(14): p. 4067-4081.

14. Hayakawa, Y. and J.A. Szpunar, The role of grain boundary character distribution in secondary recrystallization of electrical steels. Acta Materialia, 1997. 45(3): p. 1285-1295.

15. Hayakawa, Y. and J.A. Szpunar, A comprehensive model of recrystallization for interstitial free steel. Acta Materialia, 1997. 45(9): p. 3721-3730.

16. Gruber, J., A.D. Rollett and G.S. Rohrer, Misorientation texture development during grain growth. Part II: Theory. Acta Materialia, 2010. 58(1): p. 14-19.

17. Gruber, J., H.M. Miller, T.D. Hoffman, G.S. Rohrer and A.D. Rollet, Misorientation texture development during grain growth. Part I: Simulation and experiment. Acta Materialia, 2009. 57(20): p. 6102-6112.

18. Rohrer, G.S., Grain boundary energy anisotropy: a review. Journal of Materials Science, 2011. 46(18): p. 5881-5895.

19. Olmsted, D.L., S.M. Foiles and E.A. Holm, Survey of computed grain boundary properties in face-centered cubic metals: I. Grain boundary energy. Acta Materialia, 2009. 57(13): p. 3694-3703.

20. Holm, E.A., D.L. Olmsted and S.M. Foiles, Comparing grain boundary energies in face-centered cubic metals: Al, Au, Cu and Ni. Scripta Materialia, 2010. 63(9): p. 905-908.

21. Zhang, J.M., M. Fei and K.W. Xu, Calculation of the surface energy of fcc metals with modified embedded-atom method. Chinese Physics, 2004. 13(7): p. 1082-1090.

22. Wen, Y.N. and H.M. Zhang, Surface energy calculation of the fcc metals by using the MAEAM. Solid State Communications, 2007. 144(3-4): p. 163-167.

23. Fu, B.Q., W. Liu and Z.L. Li, Calculation of the surface energy of fcc-metals with the empirical electron surface model. Applied Surface Science, 2010. 256(22): p. 6899-6907.

24. Wang, S.Y. and J.Q. Wang, Effect of grain orientation on the corrosion behavior of polycrystalline Alloy 690. Corrosion Science, 2014. 85: p. 183-192.

25. Lee, S. and H.S. White, Dissolution of the native oxide film on polycrystalline and single-crystal aluminum in NaCl solutions. Journal of the Electrochemical Society, 2004. 151(8): p. B479-B483.

Chapter 7
Advanced local electrochemical techniques to study the microstructural aspects of corrosion[1]

The experimental results on the correlation between grain orientations and grain boundary characteristics and local corrosion phenomena as obtained in the two previous chapters will be verified in this chapter by means of two advanced local electrochemical techniques, namely scanning electrochemical microscopy (SECM) and in situ electrochemical tunneling microscopy (EC-STM). Dr. Esther Martinez Lombardia, my research partner in this joined PhD project between VUB and UGent, carried out the local electrochemical measurements discussed in this chapter, my contribution consisted in providing the materials and the input on the physical metallurgical phenomena happening in these materials. In this chapter, the main findings of the research of dr. Esther Martinez Lombardia are summarized and compared with the results found in the two previous chapters. A more detailed description of the results obtained with the local electrochemical techniques can be found in the thesis of Dr. Esther Martinez-Lombardia called 'Study of the correlation between microstructure and corrosion properties of polycrystalline copper' [1].

7.1 Local electrochemical techniques

Scanning electrochemical microscopy (SECM) [2, 3] and in situ electrochemical scanning tunneling microscopy (in situ EC-STM) [4, 5] are techniques within the broader class of the scanning probe microscopy [6, 7]. This is a subdivision of microscopy that forms images of surfaces by using a physical probe that scans the sample. The methodology of using these interactions to obtain an image is in general called a mode. At first, some information will be given on the techniques that will be used.

[1] This chapter is based on the following publications: E. Martinez Lombardia, V. Maurice, L. Lapeire, I. De Graeve, K. Verbeken, L. Kestens, P. Marcus, H. Terryn, In Situ Scanning Tunneling Microscopy Study of Grain-Dependent Corrosion on Microcrystalline Copper, The Journal of Physical Chemistry C 118 (2014) 25421-25428. **and** E. Martinez Lombardia, Y. Gonzalez-Garcia, L. Lapeire, I. De Graeve, K. Verbeken, L. Kestens, J.M.C. Mol, H. Terryn, Scanning electrochemical microscopy to study the effect of crystallographic orientation on the electrochemical activity of pure copper, Electrochimica Acta 116 (2014) 89-96.

7.1.1 Scanning electrochemical microscopy (SECM)

Scanning Electrochemical Microscopy (SECM) is a technique used to visualize differences of topography and surface reactivity by using a probe that scans the specimen at a near-field distance where interactions between the tip electrode and the sample occur.

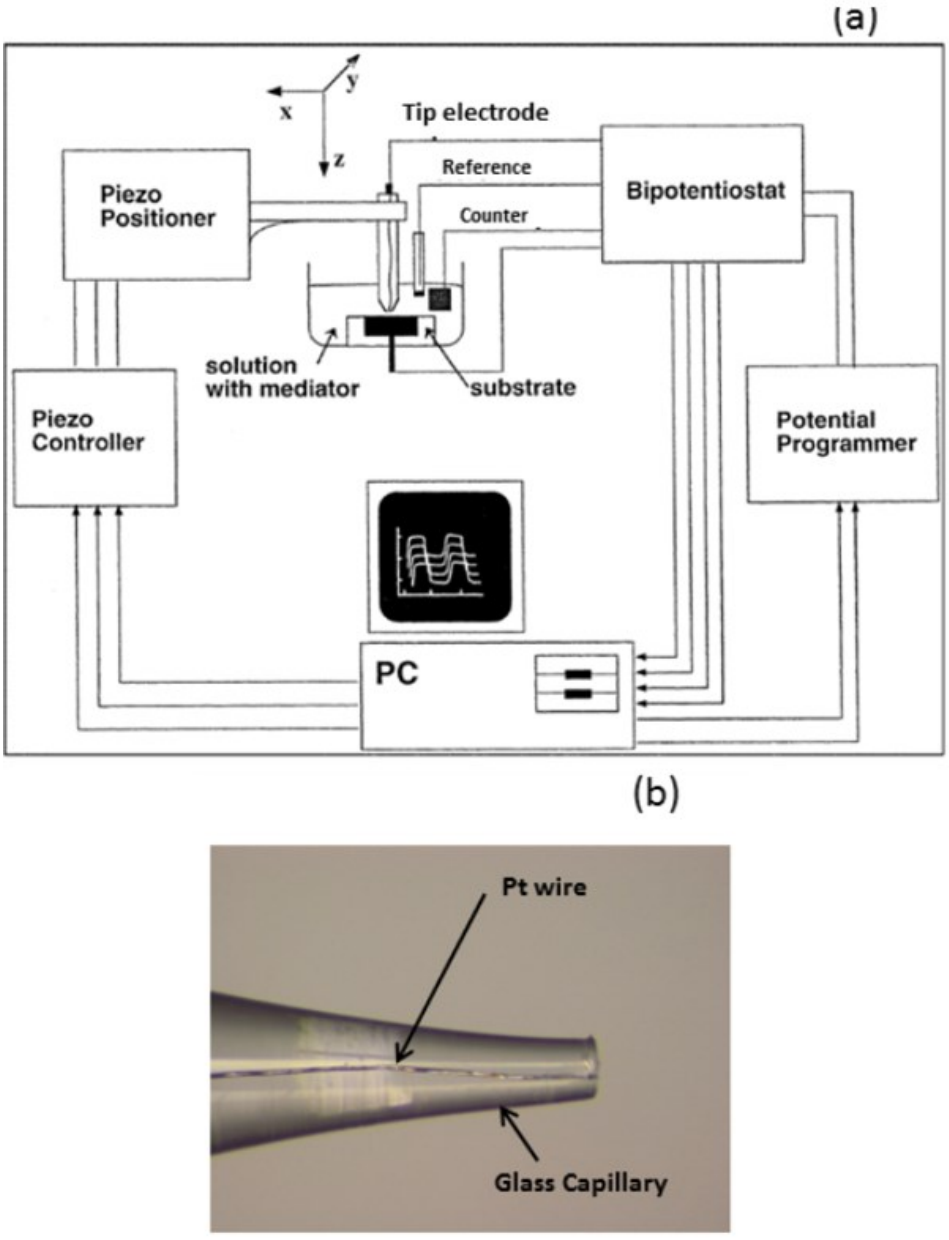

Figure 7-1: (a) Schematic representation of the SECM set-up. (b) Microelectrode with a 10 µm diameter Pt wire.

In figure 7-1a a typical SECM set-up is shown. A 4-electrode system is used with a tip electrode, a reference electrode, a counter electrode and the studied sample as the specimen electrode. The tip electrode is located just above the specimen. The potentials of both the probe and the sample electrode can be controlled by a potentiostat. By measuring the probe current, the tip can detect changes in activity of a redox reaction on the specimen surface. The distance between the tip and the sample and the scanning parameters (e.g. size and scanning step) are controlled by the controller and the piezo positioner.

7.1.1.1 Tip electrode

The tip electrode used in this chapter was a disc-shaped microelectrode composed of a platinum wire with a diameter of 10 µm sealed into a glass capillary (Fig. 7-1b). The mass transport to the electrode in solution is the most important factor to determine the behavior of an electrode in solution. When an electrode is polarized at a potential at which a certain reaction occurs, a diffusion layer is established in the vicinity of that electrode. In a disc-shaped electrode, the thickness of the diffusion layer (δ) is related to both the diffusion coefficient (D) of the species in the electrolyte and the diffusion time (t) of the species at the electrode after applying the electrical potential.

$$\delta = \sqrt{\pi D t} \tag{7.1}$$

If the diameter of the electrode is smaller than the thickness of the diffusion zone, the typical hemispherical diffusion should happen around the active surface (Fig. 7-2a).

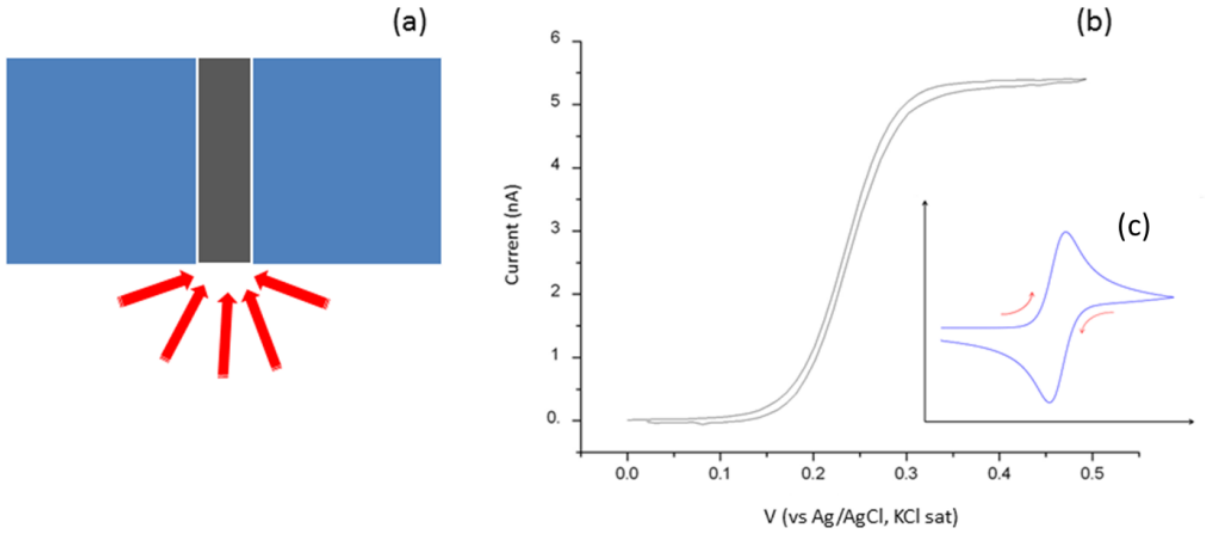

Figure 7-2: (a) Hemispherical diffusion to the microelectrode. (b) Cyclic voltammogram measured at the SECM tip in a 5mM NaCl + 0.5 mM ferrocenemethanol solution with a 10 µm Pt electrode measured with a scan rate of 0.05 V/s. (c) Typical shape of a cyclic voltammogram measured with a macro-electrode.

The cyclic voltammogram wave is shaped differently in a micro-electrode compared to a macro-electrode. While the current goes to a steady state value for the micro-electrode (Fig. 7-2b), the voltammogram is peak shaped for the macro-electrodes (Fig. 7-2c). This steady state current in the micro-electrode can be explained by the small dimensions which give a hemispherical diffusion layer, which extends into the solution. The amount of species diffusing to the electrode surface is defined by the volume of this expanding hemisphere [2].

This diffusion-limited current can be calculated by using the following equation (7.2) [8]:

$$i_{limit} = 4nFDc^{*}r \tag{7.2}$$

Where

- i_{limit}: Diffusion-limited current (A)
- n : Number of electrons in the redox reaction
- F : Faraday constant (96494 C/mol)
- D: Diffusion coefficient (m²/s)
- c^{*}: Concentration of the electroactive species in the bulk solution (mol/m³)
- r: Radius of the microelectrode (m)

The value of 4 is the geometric factor of an ideal ultra-micro disk-shaped electrode.

7.1.1.2 Working modes of SECM

In the last decades, different working modes of SECM have been developed such as the feedback mode [2], the sample generation-tip collection mode [9] and the redox competition mode [10].

In this chapter, the SECM will be operated in the feedback mode to monitor the electrochemical activity of different grain orientations for an active copper surface. Figure 7-3 gives a schematic representation of the working theory of a SECM in feedback mode.

A small faradaic current is generated when a microelectrode is polarized to a potential driving the conversion of the redox species present (Fig. 7-3a). The current observed when the tip is at relatively infinite distance away from the substrate, i.e. in bulk solution, is the i_{limit}. Under these conditions, the current is driven by the hemispherical flux of the species from the bulk solution to the tip (Fig. 7-3a). An interaction between the tip and the sample will occur once the tip is close to the sample surface. This will induce a change in the faradaic current. Dependent on the sample surface, two scenarios can occur:

1) The tip approaches an insulated substrate (Fig. 7-3b). This insulating surface blocks the diffusion of redox species towards the active area of the micro-electrode. The diffusion of the mediator to the tip of the micro-electrode is blocked and makes the diffusion rate a limiting factor. The blockage of diffusion towards the micro-electrode will lead to a depletion of species available for the conversion. Therefore, the current measured at the micro-electrode will drop. This effect is called negative feedback. The distance from the surface when the current starts to drop is called the near-field. The near-field distance is typically 3 to 5 times the diameter of the active area of the micro-electrode.

2) The tip approaches a conductive surface (Fig. 7-3c). In this case, the electroactive species reduced at the micro-electrode tip diffuses to the substrate and will be recycled as it accepts electrons from the active surface. The equilibrium disturbed by the SECM tip will be re-established by the Nernst potential of the surface to reconvert the species converted at the tip and will therefore increase the current at the tip. The increment of current in the proximity of a conductive surface is known as positive feedback.

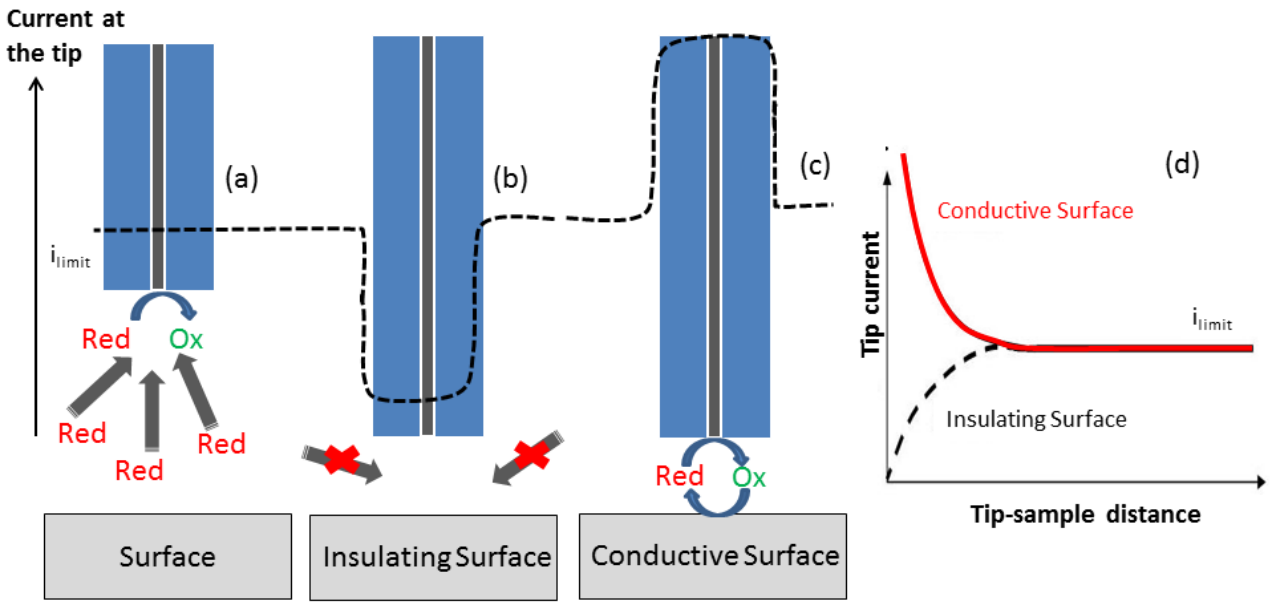

Figure 7-3: Feedback mode of a SECM where reduced species in solution are oxidized at the SECM tip: (a) in bulk, (b) negative feedback, (c) positive feedback and (d) typical curve when approaching over an insulating and a conductive surface, respectively.

Figure 7-3d shows the current changes when the SECM tip approaches both insulating surfaces (black line) and conductive (red line), this change in current is called approaching curve.

7.1.2 Electrochemical scanning tunneling microscopy (EC-STM)

A scanning tunneling microscope (STM) is an instrument used for imaging surfaces at the atomic level. STM is based on the concept of quantum tunneling. When a conductive sharp tip is brought very near to the conductive surface electrons can tunnel through the vacuum between them, producing a tunneling current.

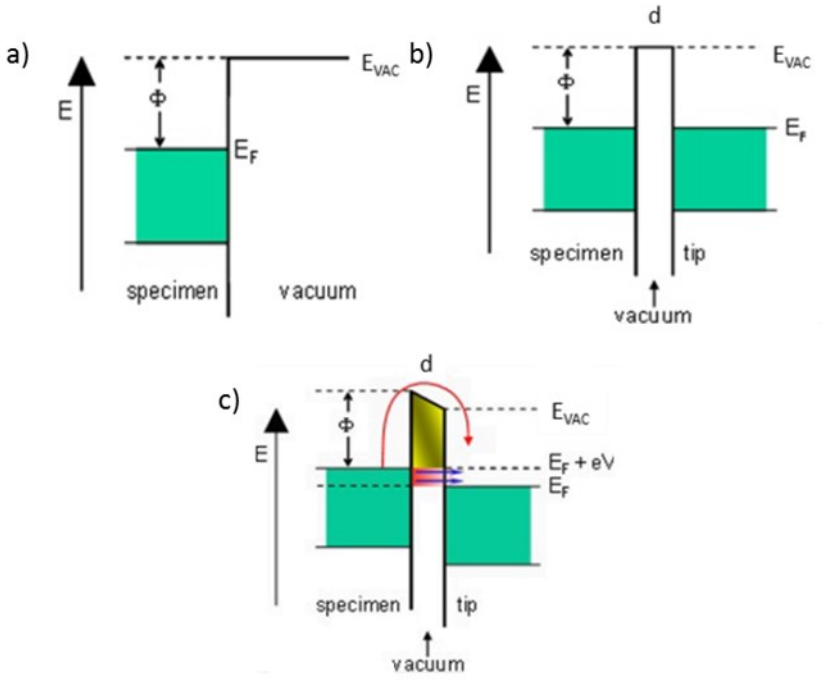

Figure 7-4: (a) Fermi energy of a metallic surface when (b) the STM tip is close to the metallic surface and (c) when a bias voltage is applied so that electrons can tunnel [11].

In a metal, the energy levels of the electrons are filled up to a particular energy, called the Fermi energy, E_F. The additional energy needed to remove an electron into free space is called the work function, Φ_w (Fig. 7-4a). If a tip is brought very close to the metal surface, there is a narrow region of empty space left between them, and on either side, electrons are present up to the Fermi energy level. In order to travel the distance between them, the electrons need to overcome the work function barrier (Fig. 7-4b). When a bias (voltage difference) is applied between the sharp tip and the metal surface electrons can tunnel through the vacuum between them. This current is called the tunneling current (Fig. 7-4c). A simple formula to calculate the tunneling current (I_t), based on quantum mechanics is (7.3):

$$I_t = kqVe^{-2d\frac{\sqrt{2m\Phi_W}}{h}} \tag{7.3}$$

Where

- k: Constant
- q: Electron charge (C)
- V: Applied voltage (V)
- m: Electron mass (meV/C^{-2})
- Φ_w: Work function (meV)
- h: Planck's constant (MeV.s)
- d: Distance between tip and sample (Å)

The tunneling current depends on the distance between the tip and the sample d, the voltage V and the height of the energy barrier Φ_w. This simplified equation shows that the tunneling current obeys Ohm's law which states that the current is proportional to the voltage V. The tunneling current is an exponential function of the distance. Changes of only 0.1 nm in the separation distance cause an order of magnitude difference in the tunneling current. This gives STM its remarkably high sensitivity.

With STM, it is possible to work in constant current mode or in constant height mode. In constant current mode, a feedback loop is used to adjust the height of the tip in order to hold the tunneling current constant. The scanner height measured at each location is then used to map the surface topography.

7.2 SECM to study relationship between microstructure and electrochemical activity

In this section scanning electrochemical microscopy (SECM) will be used to study the electrochemical activity of high purity copper as a function of the grain orientation. Copper will be studied in the active dissolution rate. Afterwards, the obtained results are compared to the results found in chapter 5 and chapter 6 of this work. In addition, a study of the grain-dependent insulation properties of the passive layer formed on copper was also performed. These results were discussed in detail in the PhD-thesis of Dr. Esther Martinez Lombardia [1].

7.2.1 Introduction

The SECM technique has been widely used to study the electrochemical activity and the local dissolution of different metals [12-18]. However, studies to investigate the correlation between the electrochemical characteristics of a metal surface and microstructural features of metals such as grain orientation and grain boundary parameters using this technique have been scarcely published. Fushimi studied the growth of an oxide film on titanium and found out that the electrochemical activity of the oxide depends on the crystallographic orientation of grains [12, 19]. However, SECM measurements were carried out without any knowledge or

information on the surface microstructure which turns out to be one of the main drawbacks of their procedure.

In this section, the grain dependent electrochemical activity of polycrystalline copper is studied, focusing on the <001>// ND and <111>// ND orientations. These orientations are chosen in order to be able to make the correlation with the results obtained in chapter 5 on the effect of neighboring grains on the corrosion behavior of a specific grain orientation. The SECM operating in feedback mode is used to monitor the electrochemical activity of the selected grain orientations for the active copper surface in an in situ manner.

By the complementary use of EBSD and SECM, the effect of specific grain orientations on the activity of copper is established and, more important, the effect of neighboring grain orientation on the local electrochemical behavior will be evaluated.

7.2.2 Experimental details

7.2.2.1 Material processing

For the experiments presented in this section, the high purity copper underwent a 75% hot rolling reduction, which allowed destroying the cast microstructure and providing a completely recrystallized microstructure, as previously discussed in section 4.3.2. This was followed by an annealing treatment for 24h at 800°C in order to realize a suitable grain size in the material (mean grain size > 40 µm). Subsequently, the material was mechanically ground and polished, finishing with 1 µm diamond paste. In order to characterize the same site of the samples, indents were made as markers and the same areas were characterized with both EBSD and SECM. To obtain a suitable surface preparation for EBSD, a final electropolishing step (10 V, 10 s) in a phosphoric acid electrolyte was necessary. EBSD measurements were carried out with a step size of 0.5 µm.

7.2.2.2 SECM experimental set-up

The selected working mode for the SECM in this investigation was the feedback mode, using ferrocenemethanol as the electrochemical mediator. In this mode, it is possible to distinguish differences in electrochemical activity of the surface. The selected reaction at the micro-electrode is the oxidation of Fe(II) to Fe(III) from the electrochemical mediator. The tip current at the proximity of the metal surface is a function of the nature of the substrate, making it possible to distinguish insulating from conductive areas. In the case of an insulating surface, the current at the tip will be lower than the limiting current measured in the bulk of the solution. If the substrate is able to regenerate Fe(II) from the reduction of Fe(III) formed at the microelectrode and hence induce a redox cycling leading to a positive feedback, the current at the tip will increase.

All SECM measurements were carried out with the scanning electrochemical workstation from Sensolytics. A platinum microelectrode of 5 µm radius was used as the working electrode. An Ag/AgCl/KCl(sat.) electrode was used as the reference electrode, and a platinum wire as the counter electrode. All potentials reported in this paper are thus relative to the Ag/AgCl/KCl(sat.) reference electrode potential. The SECM is operated in feedback mode imaging using 0.5 mM ferrocenemethanol as electrochemical mediator. The potential of the microelectrode was controlled at +0.5 V, assuring a limiting-current state for the oxidation of ferrocenemethanol to ferriceniummethanol according to the cyclic voltammogram (CV) recorded at the microelectrode (Fig. 7-5). The sample-tip distance was established by approaching curve measurements. For all experiments report in this work, the microelectrode was located at a distance corresponding to a change in the current of approximately 20% with respect to the limiting current. The chosen criteria assure that the measured current is influenced by the surface activity, but the microelectrode is still far enough from the surface to avoid the influence of the sample topography.

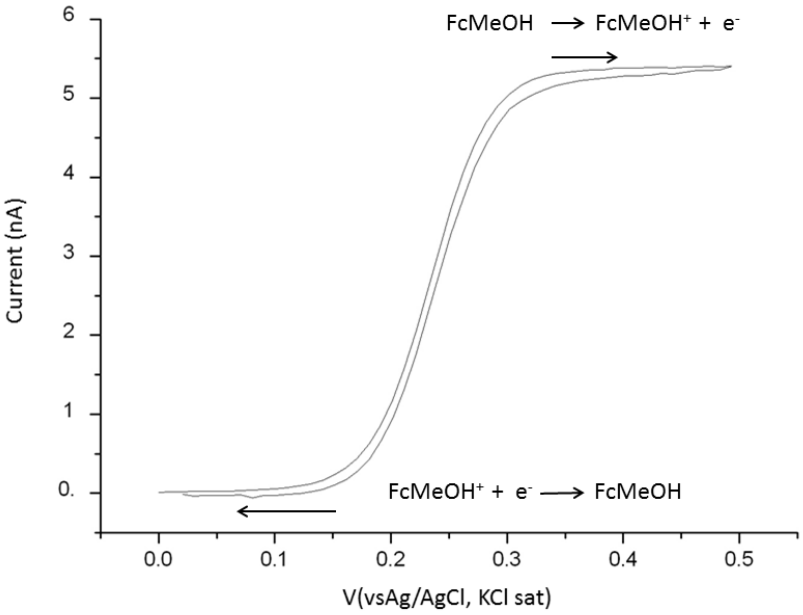

Figure 7-5: Cyclic voltammogram measured at the SECM tip in a 5 mM NaCl + 0.5 mM ferrocenemethanol solution with a 10 µm Pt electrode. Scan rate: 0.05 V/s.

SECM measurements of copper in the active state were performed in 5 mM NaCl solution which contains the electrochemical mediator. The sample was maintained at open circuit potential (OCP). The tip electrode was scanned stepwise within a distance of 400 µm in x and y direction with dx = 10 µm and dy= 20 µm.

7.2.3 Results

The variable reactivity of the copper surface, depending on the crystallographic orientation during its immersion in a chloride solution as corrosive environment, is monitored. For these experiments, areas of the polycrystalline sample with neighboring <001>// ND and <111>// ND oriented grains were selected. These orientations are chosen to confirm with a local electrochemical technique the experimental findings done in chapter 5 concerning the influence of the orientation of neighboring grains on the corrosion behavior of an individual grain with a specific orientation.

Figure 7-6a and 7-6b represent areas of the same location of the sample with, on the one hand, the presence of the desired combination of grain orientations demonstrated and, on the other hand, that same region as characterized by SECM experiments.

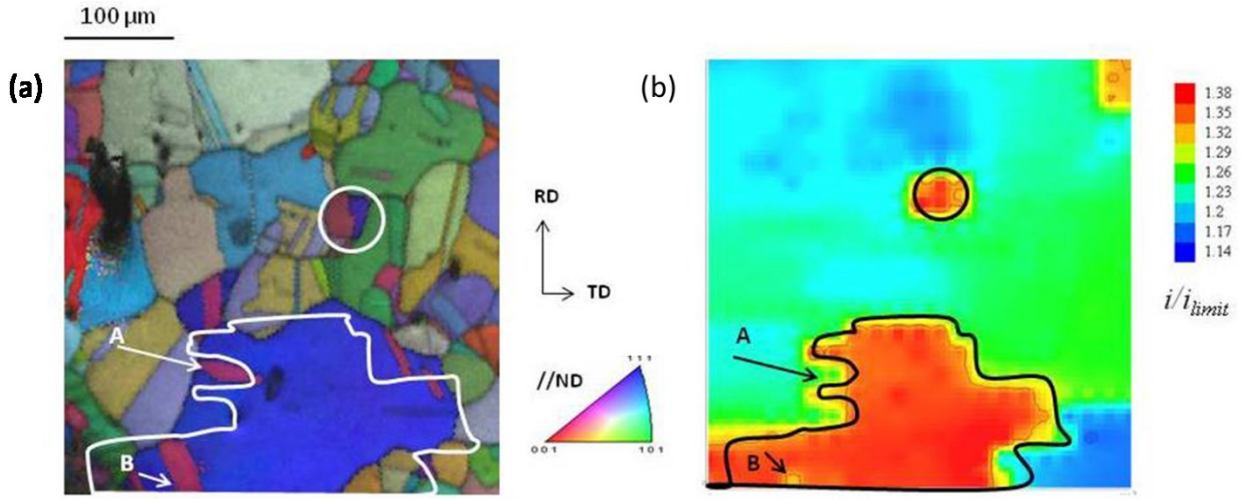

Figure 7-6: (a) Combined inverse pole figure (IPF)/ image quality (IQ) map and (b) corresponding SECM current map. Scanned area 400 µm in x and y direction with dx = 10 µm and dy= 20 µm, experiments in the active dissolution state.

From the combined inverse pole figure (IPF)/ image quality (IQ) map and corresponding SECM normalized current map in figure 7-6, it can be observed that current values in the whole area are higher than the limiting current (which is 1 for the normalized current). This indicates that the copper surface is electrochemically active which is expected since copper is easily corroded by chloride ions. Observed heterogeneities on the current distribution can be correlated to the microstructure. Comparing figure 7-6a and figure 7-6b shows that the shape of the <111>// ND oriented grain coincides with an area of higher current at the tip, indicating a higher activity compared to the other orientations present on the inverse pole figure map. This grain is observed to have small neighboring grains with orientations close to <001>// ND, marked with arrows in figure 7-6. There also is a small area that shows a higher current (marked with a circle

in figure 7-6), which corresponds to an area consisting of two small <001>// ND and <111>// ND oriented grains, respectively. A clear difference between the two grains cannot be made here which is most probably due to the limited spatial resolution provided by the size of the microelectrode as compared to grain size of these specific grains.

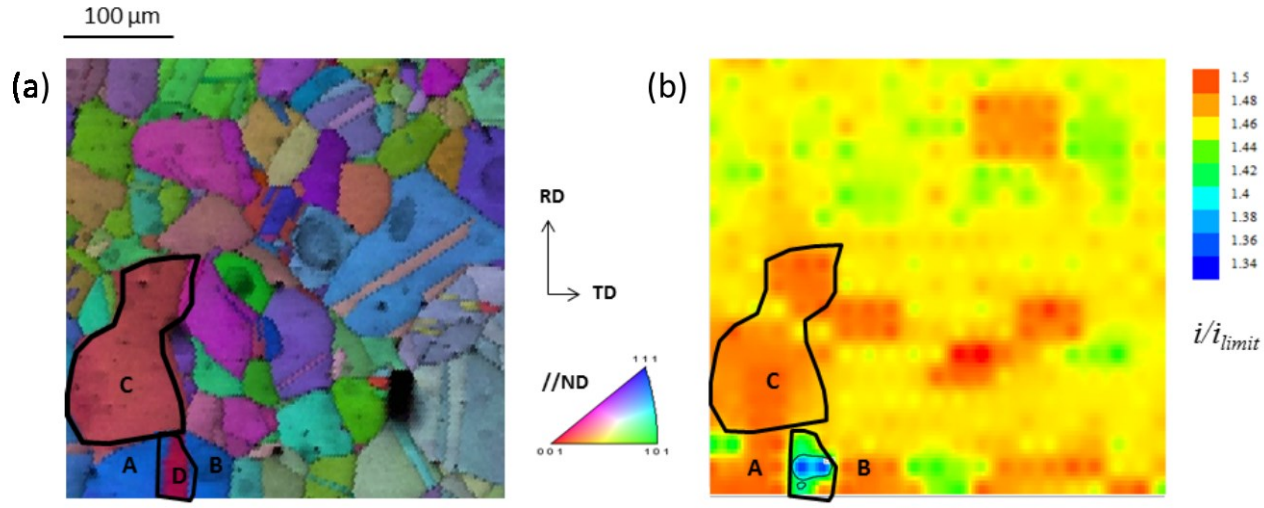

Figure 7-7: (a) Combined inverse pole figure (IPF)/ image quality (IQ) map and (b) corresponding SECM current map. Scanned area 400 µm in x and y direction with dx = 10 µm and dy= 20 µm, experiments in the active dissolution state. Area involving <111>// ND (A and B) and <001>// ND (C and D) oriented grains.

Another mapping measured under the same conditions on a different copper sample are given in figure 7-7. Current values in the whole area are higher than the limiting current, indicating that the copper surface is electrochemically active, as expected. In figure 7-7b, a higher current is measured above the grains A and B which are <111>// ND oriented grains, again these grains are adjacent to grains which have a <001>// ND orientation. It is also interesting to note that grains C and D are both <001>// ND oriented grains, but the measured current is lower for the grain D which is completely surrounded by <111>// ND oriented grains. On the other hand, the grain marked as grain C shows a higher current and, in this case, that specific grain is predominantly surrounded by grains with other than <111>// ND orientations.

7.2.4 Discussion

In the active state, two different areas with a <111>// ND oriented grain with neighboring <001>// ND oriented grains, were chosen, with the rest of the grains in the area under investigation having different orientations. The SECM in the feedback mode observed a positive feedback response from the scanned area in both cases. Higher activity was observed above the <111>// ND grain suggesting more susceptibility to dissolution than the <001>// ND oriented grains when they appear together on the microstructure.

In chapter 5 and chapter 6, where adjacent <001>// ND and <111>// ND grains were studied, the same electrochemical behavior was observed, namely a higher dissolution rate for the <111>// ND oriented grain when surrounded by <001>// ND oriented grains. In figure 7-6, the big <111>// ND grain has small adjacent <001>// ND oriented grains marked as A and B. A lower current above grain A indicating lower activity is observed, but this is not observed for grain B. Another area involving these two neighboring orientation is marked with a circle in figure 7-6. Here only the higher activity of the surface could be detected although it was an area where two different grains can be distinguished. The small size of <001>// ND grains compared to the neighboring <111>// ND grains makes detection difficult with the 10 µm microelectrode employed in this work. In figure 7.6, the two <111>// ND oriented grains show a higher current when compared with the small <001>// ND oriented grain that lies in between them. It is interesting to notice that the grain marked as C has also an orientation close to <001>// ND but in this case the current measured is as high as for the two <111>// ND oriented grains. The main difference between these two <001>// ND oriented grains is that grain D, is completely surrounded by <111>// ND oriented grains, while the grain marked as C, is surrounded by several grains which have different orientations. This suggests a partial change of the electrochemical behavior of the <001>//ND depending on the orientations of the surrounding grains.

Based on these results it was confirmed that the corrosion behavior of the copper not only depends on the activity of the individual nature of the grains. It is also affected by the cooperative effect between adjacent grains that may alter the initially expected response of the material in presence of the aggressive environment.

7.2.5 Conclusion

The grain dependent electrochemical activity of pure copper in the active state was investigated by means of EBSD and SECM. SECM scans on selected areas of the copper surface with specific grain orientations determined by EBSD were performed in order to establish the electrochemical activity in an in situ manner.

It was found that for copper in the active state the highest current is observed for the <111>// ND orientation. It was also concluded that the <100>// ND oriented grain is less active when located between <111>// ND oriented grains. This confirmed the experimental results reported in chapter 5 and chapter 6. With local electrochemical techniques it is demonstrated that besides the grain orientation, the orientation relations between the neighboring grains can play a decisive role in the corrosion process for polycrystalline copper.

7.3 In situ scanning tunneling microscopy to study relationship between microstructure and electrochemical activity

Up to now, in situ electrochemical scanning tunneling microscopy (in situ EC-STM) has been used to study the electrochemical behavior of single crystals. In this section, in situ EC-STM is proven to be a powerful tool for providing valuable topographic information to study the corrosion properties of polycrystalline material. In situ EC-STM will be used in this section to visualize the susceptibility of different types of grain boundaries to intergranular corrosion in fine grained copper. Afterwards, the obtained results are compared with the results found in chapter 6.

7.3.1 Introduction

As discussed in chapter 2, it is well known that the grain boundary type has a big influence on the intergranular corrosion behavior of a polycrystalline material [20]. In chapter 6, the gold nanoplating technique was presented as an innovative technique to demonstrate differences in the electrochemical activity of specific features of the copper microstructure such as grain orientation and grain boundary characteristics. Furthermore, by applying this technique, the lower grain boundary energy of the coherent twin grain boundaries in copper was confirmed.

Various local electrochemical techniques have been applied for the investigation of the electrochemical behavior of grain boundaries in metals [21, 22]. However, there are some limitations to their capabilities mainly due to the limited lateral resolution (around 20 µm). Ex situ scanning tunneling microscopy (STM) has already been used to study the atomic structure of a single grain boundary in graphite [23]. To date, however, electrochemical scanning tunneling microscopy (EC-STM) has never been used to observe in situ the intergranular corrosion evolution on a polycrystalline material, although application of this technique for corrosion studies of single-crystal materials is extensive [24-26].

In this section, cryogenic rolling will be used for manufacturing microcrystalline copper with a high grain boundary density and a high amount of ∑3 grain boundaries [27]. The microstructure will be quantified by EBSD and in situ EC-STM will be applied to analyze the corrosion of the different types of grain boundaries.

7.3.2 Experimental details

7.3.2.1 Material processing

In order to realize a suitable copper microstructure adapted to the requirements of the in situ EC-STM setup the cryogenic rolling technique was used. This cryogenic rolling technique is discussed in detail in section 4.4. After 91% cryogenic rolling reduction, an annealing step for 1 min at 200°C was used to ensure a fully recrystallized microstructure while maintaining a

suitable grain size for the field of view of the EC-STM scanner. The material was mechanically ground and polished, finishing with 1 µm diamond paste. To obtain a suitable surface preparation for EBSD, a final electropolishing step (10 V, 10 s) in a phosphoric acid electrolyte was necessary. The microstructure of the samples was characterized by EBSD. The EBSD system is attached to an FEI® FE-SEM (Quanta) operated at 20 kV. Measurements were carried out with a step size of 0.1 µm and the orientation data were post-processed with the commercial orientation imaging software package OIM-TSL®.

7.3.2.2 STM experimental set-up

The EC-STM experiments were performed at the 'Institut de Recherche de Chimie Paris'. All experiments were performed at room temperature with an Agilent Technologies PicoSPM system. The selected electrolyte was a 10 mM HCl aqueous solution. The sample was mounted in the in situ EC-STM cell with a working electrode area of 0.16 cm², a Pt pseudo-reference electrode and a Pt wire counter electrode. The tungsten STM tips were manually prepared before every experiment from 0.25 mm diameter wire electrochemically etched in 3 M NaOH and covered by Apiezon wax. All images were obtained in the constant current mode. All potentials reported are relative to the standard hydrogen electrode (V/SHE).

The samples were exposed to the electrolyte at -0.05 V/SHE to avoid any copper dissolution before starting the experiments (open circuit potential of 0.1 V/SHE). They were then pre-treated with a scan down to -0.45 V/SHE (corresponding to the onset of hydrogen evolution) and upwards back to -0.05 V/SHE in order to fully reduce the air-formed oxide film. The topography of the metallic surface was then measured in a selected area. Afterwards, anodic dissolution was forced by scanning the potential in the positive direction till an anodic current density not exceeding 50 µA /cm² was measured. The potential was then scanned back to the starting value of -0.05 V/SHE and new images of the same area were taken at this potential. The STM tip was withdrawn from the surface while polarizing the sample and re-engaged afterwards allowing analyzing the very same area before and after several anodic cycles. The evolution of the topography was thus followed after several anodic cycles. A statistical study of the morphology and type of grain boundaries was used to link the in situ EC-STM data on intergranular corrosion behavior with a certain type of grain boundary.

7.3.3 Results and discussion

Figure 7-8a shows the inverse pole figure (IPF) map of the microcrystalline copper sample. The average grain size is 1.1 µm. The image quality (IQ) map in figure 7-8b shows the different types of boundaries. Blue lines indicate random high angle boundaries and red lines indicate all ∑3 boundaries. The length fraction of ∑3 boundaries is 51%. More detailed analysis reveals several long and parallel-sided ∑3 boundaries (pointed by black arrows). Most likely these are coherent twins since they are characterized by their parallel-sided arrangement [28].

In order to confirm this assumption, an area of 5050 µm² was studied. Of the 227 grain boundaries under evaluation, only one straight grain boundary was found to be a random high angle boundary. All other straight boundaries were identified as ∑3 boundaries. On the other hand, when looking at the ∑3 boundaries, it was found that around 50% of them are straight and 50% are curved. It can be then concluded that a straight grain boundary has a very high probability to be a coherent twin boundary and that a curved grain boundary can be cataloged either as random high angle grain boundary or a non-coherent ∑3 boundary.

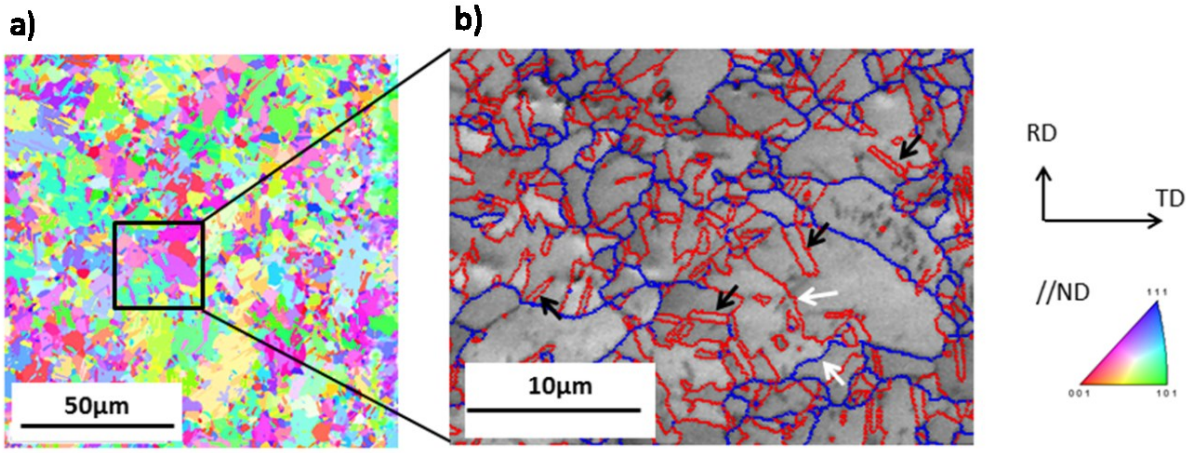

Figure 7-8: (a) Inverse pole figure (IPF) map and (b) image quality (IQ) map of microcrystalline copper. Blue lines denote random high angle boundaries (> 15°) and red lines denote ∑3 boundaries. Coherent twins are marked with black arrows and random and non-coherent ∑3 boundaries are marked with white arrows.

Figure 7-9a shows the cyclic voltammogram for the cathodic pre-treatment in the EC-STM cell. The reduction peak is observed at -0.20 V/SHE. The thickness (δ) of the cathodically reduced oxide layer was calculated from the charge density (q) of the reduction peak according to equation 7.4:

$$\delta = \frac{qV}{zF} \tag{7.4}$$

where V is the molar volume of the reduced oxide, F is Faraday's constant and z the number of exchanged electrons.

The measured reduction charge density is around 1000 µC/cm². Assuming that the oxide layer consists of Cu_2O (V = 23.9 cm³ /mol), the calculated thickness of the Cu_2O oxide layer is 2.5 nm. This is in agreement with the reported thickness of the air-formed oxide on copper of around 2.4 to 3 nm [29].

After cathodic reduction, an anodic potentiodynamic polarization was performed (Fig. 7-9b) in order to induce dissolution of the copper metal and to produce intergranular corrosion. The STM tip was withdrawn from the surface while polarizing the sample and re-engaged afterwards allowing analyzing the very same area before and after several anodic cycles. From the anodic charge density transfer (129 µC/cm²), an equivalent thickness of ~0.1 nm of dissolved Cu(I) can be calculated using equation 7.1, which amounts to less than one equivalent monolayer. The cathodic peak measured at 0.1V/SHE after dissolution most likely corresponds to deposition of dissolved copper. This process does not annihilate the local dissolution-induced modifications as shown below.

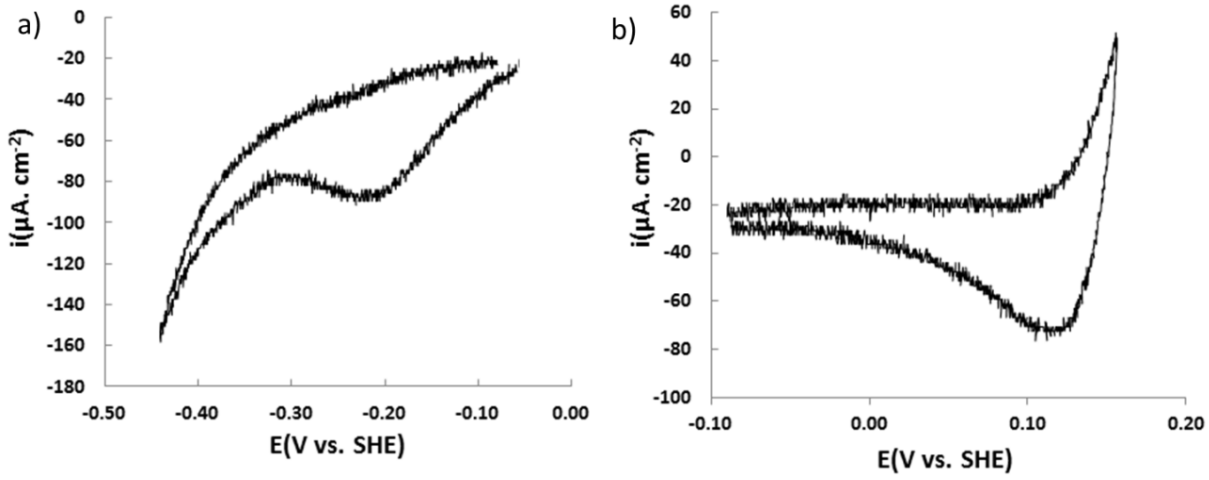

Figure 7-9: (a) Cyclic voltammograms for the cathodic pre-treatment and (b) anodic dissolution of microcrystalline copper in 10 mM HCl, as recorded in the EC-STM cell. Scan rate= 10 mV/s.

Figure 7-10 shows the sample topography prior to (Fig. 7-10a) and after (Fig. 7-10b) four anodic scans. Two straight grain boundaries (marked by green arrows) can be seen together with several curved grain boundaries. The evolution of the different grain boundaries can be followed by cross section analysis. A considerable attack is observed for the curved grain boundary (height profile 2, Fig. 7-10d). The magnitude of intergranular corrosion is determined by both the penetration at the grain boundary and the dissolution at the surface of the grains that form the grain boundary. In this case, a significant depth penetration of 2 nm, equivalent to ~10 monolayers, and much higher than measured electrochemically, is measured showing that dissolution proceeds essentially at grain boundaries in these conditions. Figure 7-10c shows a height profile across the two straight grain boundaries. There is no indication of intergranular corrosion, since both profiles (obtained before and after anodic dissolution) are similar. As already mentioned, the straight grain boundary is assigned to the category of coherent twin grain boundaries. On the other hand, the curved grain boundary is either a random high angle grain boundary or a non-coherent ∑3 boundary.

The data presented so far thus show that the coherent twin grain boundaries show special properties with respect to their corrosion resistance.

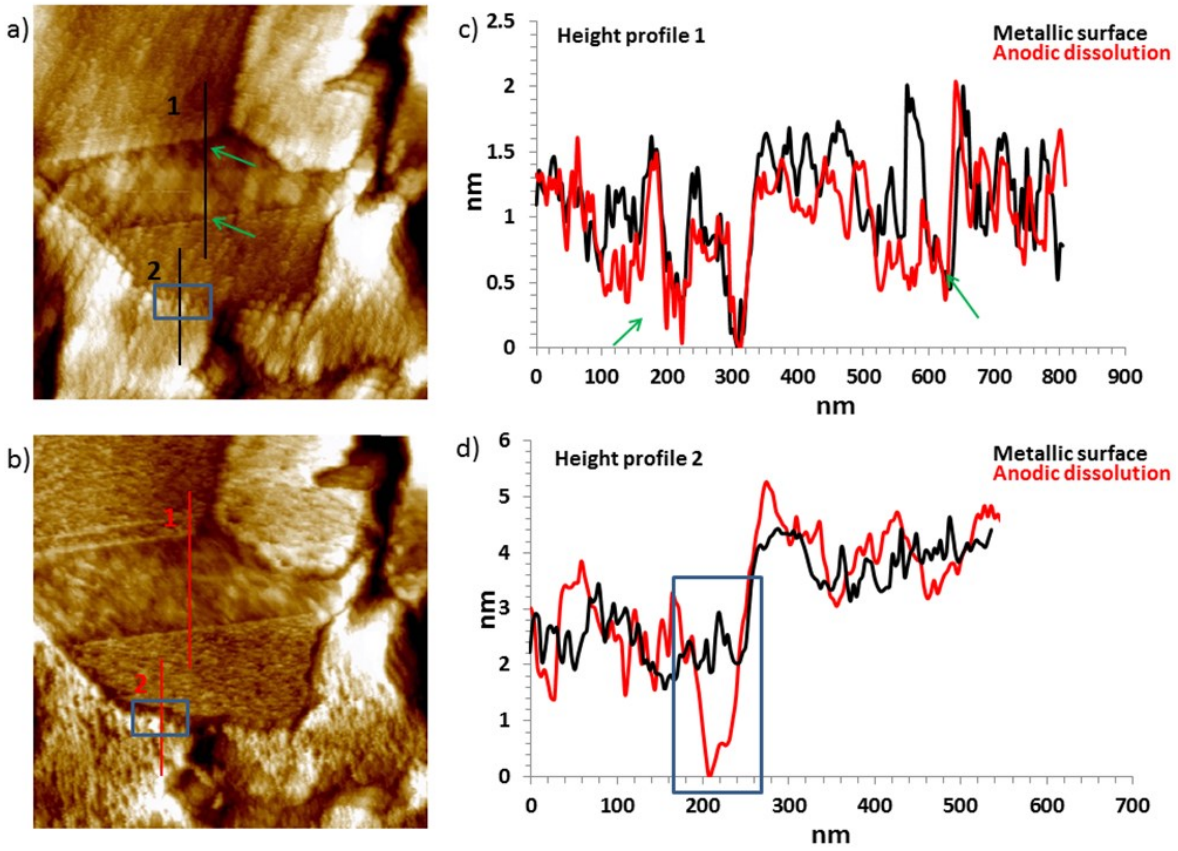

Figure 7-10: Topographic EC-STM images of the polycrystalline copper surface after (a) cathodic reduction of air-formed oxide film and (b) four anodic dissolution cycles (X = Y = 2000 nm, ΔZ = 6 nm, E_{Cu}= -0.05 V, E_{tip} = -0.25 V, I_{tip} = 4 nA) and height profiles along (c) line 1: green arrow mark coherent twin boundaries and (d) line 2: blue rectangle marks random grain boundary.

In order to confirm this observation, two straight parallel grain boundaries and two curved grain boundaries were selected on a different sample and figure 7-11 shows their evolution after one and four anodic dissolution treatments. The height profile across the two straight grain boundaries (Fig. 7-11c) shows no evolution. In contrast, the height profile across the two curved grain boundaries (Fig. 7-11d) evidences intergranular corrosion. The depth penetration is of the order of 1 nm and the grain boundary width also increases. It is thus again demonstrated that coherent twin boundaries have better properties regarding intergranular corrosion resistance.

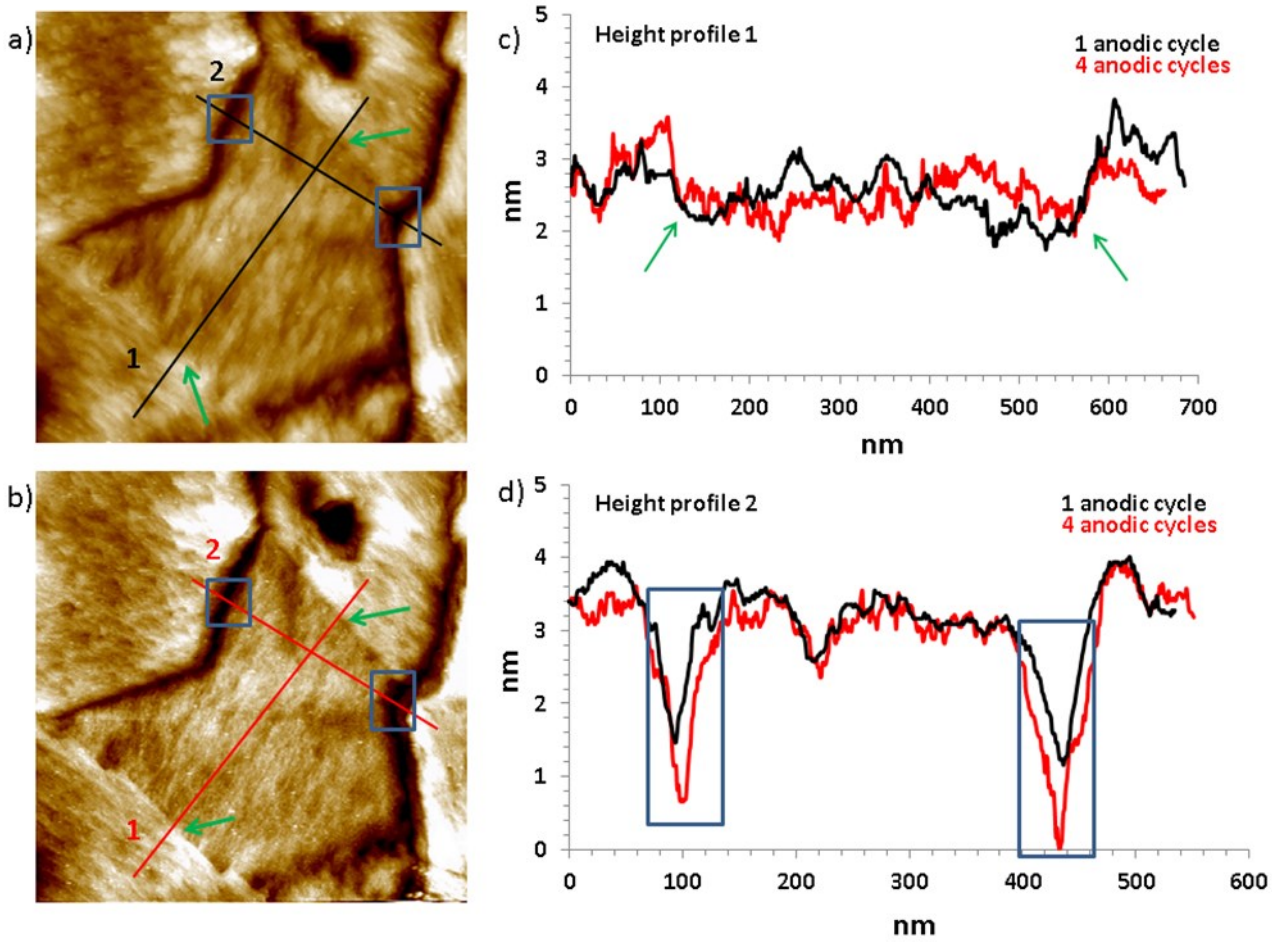

Figure 7-11: Topographic EC-STM images of metallic surface of polycrystalline copper after (a) one and (b) four anodic cycles (X = Y = 700 nm, ΔZ = 4 nm, E_{Cu}= -0.05 V, E_{tip} = -0.35 V, I_{tip} = 2 nA) and height profiles along (c) line 1: green arrows mark coherent twin grain boundaries and (d) line 2: blue rectangles mark random grain boundary.

7.3.4 Conclusion

By combining EBSD and in situ EC-STM it was possible to link grain boundary type with susceptibility to intergranular corrosion on a microcrystalline copper surface. The data provide direct evidence that the coherent twin grain boundaries are resistant against corrosion, these results nicely complement our previously reported observations in chapter 6. In this study, the potential of in situ EC-STM to visualize in situ the intergranular corrosion on a polycrystalline material is clearly demonstrated, providing important complementary information to the electrochemical description, which was obtained by the gold-nanoplating method.

7.4 Conclusion

In this chapter, two local electrochemical techniques, namely scanning electrochemical microscopy (SECM) and in situ electrochemical tunneling microscopy (in situ EC-STM) are used to verify the experimental results obtained in chapter 5 and chapter 6.

With in situ EC-STM, the grain dependent electrochemical of pure copper in the active state was investigated. In accordance to the results obtained in chapter 5 with AFM, it was found that when a <100> //ND grain is located adjacent to a <111>// ND grain, this grain is less active compared to a <100> // ND grain with random oriented neighbors. This shows again that besides the grain orientation, also the orientation relationship between the neighboring grains plays a decisive role in the corrosion process.

By means of in situ EC-STM the susceptibility to intergranular corrosion is visualized. From these experiments the conclusion can be made that coherent twin boundaries are resistant against corrosion, which is in line with results obtained by gold-nanoplating.

Consequently, this chapter provides a nice example of how local electrochemical techniques can offer complementary information to the electrochemical description presented by AFM and the gold-nanoplating technique on the copper corrosion behavior and as such demonstrates to be a very valuable addition to these results.

7.5 References

1. Martinez Lombardia, E., Study of the relation between microstructure and corrosion properties of polycrystalline copper, in Department of Materials and Chemistry. 2014-2015, Vrije Universiteit Brussel: Brussels.

2. Bard, A.J., F.R.F. Fan, J. Kwak and O. Lev, Scanning electrochemical microscopy - introduction and principles. Analytical Chemistry, 1989. 61(2): p. 132-138.

3. Engstrom, R.C. and C.M. Pharr, Scanning electrochemical microscopY. Analytical Chemistry, 1989. 61(19): p. A1099-&.

4. Itaya, K., K. Higaki and S. Sugawara, Insitu scanning tunneling microscopy of platinum-electrode in sulfuric-acid. Chemistry Letters, 1988(3): p. 421-424.

5. Gentz, K. and K. Wandelt, Electrochemical Scanning Tunneling Microscopy. Chimia, 2012. 66(1-2): p. 44-51.

6. Friedbacher, G. and H. Fuchs, Classification of scanning probe microscopies - (Technical report). Pure and Applied Chemistry, 1999. 71(7): p. 1337-1357.

7. Poggi, M.A., E.D. Gadsby, L.A. Bottomley, W.P. King, E. Oroudjev and H. Hansma, Scanning probe microscopy. Analytical Chemistry, 2004. 76(12): p. 3429-3443.

8. Arca, M., A.J. Bard, B.R. Horrocks, T.C. Richards and D.A. Treichel , Advances in scanning electrochemical microscopy - plenary lecture. Analyst, 1994. 119(5): p. 719-726.

9. Dantas, L.M.F., A.P.R. De Souza, P.S. Castro, T. Paixao and M. Bertotti, SECM Studies on the Electrocatalytic Oxidation of Glycerol at Copper Electrodes in Alkaline Medium. Electroanalysis, 2012. 24(8): p. 1778-1782.

10. Eckhard, K., X. Chen, F. Turcu and W. Schuhmann, Redox competition mode of scanning electrochemical microscopy (RC-SECM) for visualisation of local catalytic activity. Physical Chemistry Chemical Physics, 2006. 8(45): p. 5359-5365.

11. Hipps, K.W., Scanning tunneling spectroscopy (STS), in Handbook of Applied Solid State Spectroscopy, D.R. Vij, Editor. 2006, Springer US. p. 305-350.

12. Fushimi, K., K.A. Lill, and H. Habazaki, Heterogeneous hydrogen evolution on corroding Fe-3 at.% Si surface observed by scanning electrochemical microscopy. Electrochimica Acta, 2007. 52(12): p. 4246-4253.

13. Davoodi, A., J. Pan, C. Leygraf and S. Norgren, Probing of local dissolution of Al-alloys in chloride solutions by AFM and SECM. Applied Surface Science, 2006. 252(15): p. 5499-5503.

14. Gabrielli, C., S. Joiret, M. Keddam, H. Perrot, N. Portail, P. Rousseau and V. Vivier, A SECM assisted EQCM study of iron pitting. Electrochimica Acta, 2007. 52(27): p. 7706-7714.

15. Fushimi, K. and M. Seo, An SECM observation of dissolution distribution of ferrous or ferric ion from a polycrystalline iron electrode. Electrochimica Acta, 2001. 47(1-2): p. 121-127.

16. Zhu, R.K. and J.L. Luo, Investigation of stress-enhanced surface reactivity on Alloy 800 using scanning electrochemical microscopy. Electrochemistry Communications, 2010. 12(12): p. 1752-1755.

17. Yin, Y., L. Niu, M. Lu, W. Guo and S. Chen, In situ characterization of localized corrosion of stainless steel by scanning electrochemical microscope. Applied Surface Science, 2009. 255(22): p. 9193-9199.

18. Gabrielli, C., E. Ostermann, H. Perrot, V. Vivier, L. Beitone and C. Mace, Concentration mapping around copper microelectrodes studied by scanning electrochemical microscopy. Electrochemistry Communications, 2005. 7(9): p. 962-968.

19. Fushimi, K., T. Okawa, K. Azumi and M. Seo, Heterogeneous growth of anodic oxide film on a polycrystalline titanium electrode observed with a scanning electrochemical microscope. Journal of the Electrochemical Society, 2000. 147(2): p. 524-529.

20. Kim, S.H., U. Erb, K.T. Aust and G. Palumbo, Grain boundary character distribution and intergranular corrosion behavior in high purity aluminum. Scripta Materialia, 2001. 44(5): p. 835-839.

21. Liu, Z.Y., X.G. Li and Y.F. Cheng, In-situ characterization of the electrochemistry of grain and grain boundary of an X70 steel in a near-neutral pH solution. Electrochemistry Communications, 2010. 12(7): p. 936-938.

22. Zhu, R., Z. Qin, J.J. Noel and D.W. Shoesmith, Z. Ding, Analyzing the influence of alloying elements and impurities on the localized reactivity of titanium grade-7 by scanning electrochemical microscopy. Analytical Chemistry, 2008. 80(5): p. 1437-1447.

23. Simonis, P., C. Goffaux, P.A. Thiry, L.P. Biro, P. Lambin and V. Meunier, STM study of a grain boundary in graphite. Surface Science, 2002. 511(1-3): p. 319-322.

24. Kunze, J., V. Maurice, L.H. Klein, H.H. Strehblow and P. Marcus, In situ STM study of the duplex passive films formed on Cu(111) and Cu(001) in 0.1 M NaOH. Corrosion Science, 2004. 46(1): p. 245-264.

25. Vogt, M.R., A. Lachenwitzer, O.M. Magnussen and R.J. Behm , In-situ STM study of the initial stages of corrosion of Cu(100) electrodes in sulfuric and hydrochloric acid solution. Surface Science, 1998. 399(1): p. 49-69.

26. Kruft, M., B. Wohlmann, C. Stuhlmann and K. Wandelt, Chloride adsorption on Cu(111) electrodes in dilute HCl solutions. Surface Science, 1997. 377(1-3): p. 601-604.

27. Konkova, T., S. Mironov, A. Korznikov and S.L. Semiatin, Microstructural response of pure copper to cryogenic rolling. Acta Materialia, 2010. 58(16): p. 5262-5273.

28. Kumar, M., A.J. Schwartz and W.E. King, Microstructural evolution during grain boundary engineering of low to medium stacking fault energy fcc materials. Acta Materialia, 2002. 50(10): p. 2599-2612.

29. Chawla, S.K., B.I. Rickett, N. Sankarraman and J.H. Payer, An x-ray photo-electron spectroscopic investigation of the air-formed film on copper. Corrosion Science, 1992. 33(10): p. 1617-1631.

Chapter 8
General conclusions and suggestions for further research

8.1 Introduction

In order to increase the sustainability of metals, a more detailed understanding of the corrosion phenomenon is of crucial importance. In current literature, corrosion is often considered as a purely chemical interaction with nearly exclusive dependence of compositional effects, whilst ignoring the microstructural features of the metal surface. In the present doctoral thesis, results have been presented which illustrate both the role of the grain orientation and the grain boundary characteristics on the corrosion process of high purity copper. This has been done by systematically linking the quantified microstructural state variables to the resulting quantified electrochemical behavior.

The microstructural variables and the texture of the carefully engineered copper samples were determined with electron backscatter diffraction microscopy (EBSD). To quantify the electrochemical behavior several complementary techniques were used. An innovative concept was developed, called gold-nanoplating, to visualize the electrochemical activity of grains and grain boundaries on a mesoscale level. With atomic force microscopy (AFM) the topology of the copper surface was monitored after exposure to different electrolytes. In this way, the relation between the grain orientation and the dissolution rate was monitored. Also in situ scanning electrochemical microscopy (SECM) was used to investigate the grain dependent electrochemical activity of pure copper in the active state. Finally, in situ electrochemical scanning tunneling microscopy (EC-STM) was applied for the first time to study the corrosion behavior of a polycrystalline metal.

8.2 Controlled variation of the microstructure

Since microstructural features as grain orientation, grain size and grain boundary characteristics are controlled via thermomechanical processing (TMP), a detailed study of the different TMP steps on high purity copper was conducted. Not only the standard TMP steps were presented, which included hot rolling, room temperature (RT) rolling and annealing, but also the less conventional cryogenic rolling technique has been introduced. Different from the RT rolled copper which produces a pure metal texture, the cryogenically rolled copper exhibited a brass type texture. In the cryogenically rolled copper, deformation twins and shear bands were observed, in contrast to the RT rolling microstructure. After annealing, the RT rolled material

gave rise to a strong cube texture, in contrast to the cryogenically rolled material, which exhibited a very weak texture.

Starting from all these different microstructures, the electrochemical behavior of copper was studied in order to better understand how the different grain orientations and grain boundary orientations can affect the electrochemical behavior.

8.3 Relationship between grain boundaries and electrochemical activity

Many properties of polycrystalline materials are controlled by their grain boundaries. The grain boundary energy is a function of the grain boundary characteristics and therefore varies for the different grain boundaries throughout the sample. Variations in grain boundary energy can influence the local reactivity of the metal in a specific environment and consequently the extent of the different corrosion processes. Measuring this grain boundary energy is very complex. The main limitation with the techniques currently used (scanning kelvin probe, scanning droplet cell and scanning vibrating electrode technique) is their lateral resolution (around 20 µm). In this doctoral dissertation two different techniques were used for the first time to visualize differences in energy and corrosion behavior of the different types of grain boundaries.

At first, the applicability and potential of the gold-nanoplating technique was demonstrated on high purity copper. This technique is based on the electrochemical displacement of gold, where the gold is deposited form an aqueous solution on the copper surface. After gold deposition, the complementary use of EBSD and FE-SEM was particularly suited to detect differences in the electrochemical activity of the grain boundaries during the Au-Cu redox process occurring at the Cu surface. With the gold-nanoplating technique it became possible to separate the so-called special or CSL-type boundaries from random boundaries in an efficient way. It was proven that the coherent twin boundary had an extremely low amount of deposited gold and as a consequence this grain boundary should be very resistant to corrosion. With the use of EDX quantitative differences in the amount of gold deposit could be observed. As those differences in gold concentration seemed to be related to the grain boundary energy, gold-nanoplating gave experimentally obtained values of the grain boundary energy. The determined results for the quantified gold deposition on various grain boundaries in polycrystalline copper were consistent with both calculated as experimental literature predictions on grain boundary energy.

Secondly, for the first time to our knowledge in situ EC-STM was used to study the corrosion behavior of a polycrystalline metal. With the combined use of EBSD and in situ EC-STM, it was possible to link the grain boundary type with susceptibility to intergranular corrosion on microcrystalline copper. The data provided direct evidence that the coherent twin grain boundaries are resistant against corrosion, these results nicely complement the experimental results found with the gold-nanoplating technique.

8.4 Relationship between grain orientation and electrochemical activity

Different electrochemical techniques in combination with EBSD were used to study the electrochemical behavior of specific grain orientations in polycrystalline copper. All techniques reveal that the electrochemical activity of a grain not only depends on its specific crystallographic orientation, but also on the orientation of its neighboring grains.

By employing AFM in combination with EBSD it was possible to link the dissolution behavior of the polycrystalline copper to some specific crystallographic orientations. The largest dissolution gradient, evaluated by surface elevation differences, was observed between adjacent grains with near <001>// ND and near <111>// ND orientations, respectively. No significant height differences were observed between adjacent grains of different other orientations, nor when the <001>// ND and <111>// ND grains were separately evaluated. These results suggested for the first time that not only the grain orientation has an influence on the corrosion behavior, but that the orientation of the neighboring grains seems to play a decisive role in the dissolution rate.

The grain dependent electrochemical activity of pure copper was also investigated by means of gold-nanoplating. The focus was on three low-indexed orientations, namely <001>// ND, <110>// ND and <111>// ND. The results suggested that <111> // ND and <100>// ND oriented grains had a higher electrochemical activity compared to the <110>// ND grains. However, a large variation in the electrochemical activity was observed between similarly oriented grains. Consistent with the results obtained with AFM, also with the gold-nanoplating technique, deviating electrochemical behavior was observed when <111>// ND oriented grains were adjacent to <100>// ND grains. This could explain the large variations in electrochemical activity between similarly oriented grains, since the orientation of the neighboring grains could play a decisive role in the electrochemical behavior of that specific grain.

At last, the grain dependent electrochemical activity of pure copper in the active state was investigated by means a local electrochemical technique, namely in situ SECM. It was found that for the copper in the active state the highest current is observed for the <111>// ND orientation. It was also concluded that the <100>// ND oriented grain was less active when located between <111>// ND oriented grains. Also with SECM it was shown that besides the grain orientation, the orientation relations between the neighboring grains can play a decisive role in the corrosion kinetics of polycrystalline copper.

8.5 Microstructural characteristics of the corrosion process

Apart from uniform corrosion processes, corrosion and its initiation is often a locally induced phenomenon. The present work aimed evaluating whether, apart from the well documented compositional parameters that affect the corrosion process, also other microstructural characteristics would play a role. It was clearly proven here, by using a material in which we excluded compositional effects in the best possible way, that the microstructure is indeed affecting the corrosion behavior of a metal. Corrosive attack is demonstrated to be affected by the crystallographic orientation of a grain and, more specifically, of the neighboring grain orientation, while the gold-nanoplating technique also showed a clear relation between grain boundary characteristics, such as grain boundary misorientation and the amount of gold deposited. Although the present work is elaborated for one metal, namely high purity copper, it is assumed that the results represent a trend that will also be observed in other materials. However, the specific features of the microstructural aspects of corrosion and oxidation processes in other materials need to be verified and for other metals, which can have a different crystal structure, or consist of different phases, a different relationship between the microstructural features and the corrosion behavior might exist. Whereas microstructural control of materials has so far been mainly correlated to adjusting the mechanical properties of materials, the presented observations indicate the possibility of designing a metal with improved corrosion resistance compared to the conventional metals by fine-tuning its microstructure.

8.6 Suggestions for further research

Although we clearly demonstrated in this doctoral thesis that there is a correlation between the microstructural features of metals and their corresponding electrochemical behavior, some open questions remain.

8.6.1 Clarify the effect of the neighboring grains on the electrochemical behavior of an individual grain

AFM, gold-nanoplating and SECM measurements revealed that the electrochemical activity of a grain is not only depended on its specific crystallographic orientation, but also on the orientation of its neighboring grains. However, a real physical explanation of this phenomenon is still lacking and the question whether other “grain pairs” show a similar behavior is unanswered as well.

A possible way to tackle this issue is by creating a microstructure with a texture as random as possible. In this way, all relevant grain orientations and grain combinations will be sampled. With the gold-nanoplating technique the electrochemical activity of every grain could be

monitored and by means of statistical approaches, the influence of neighboring grains on the activity of one specific grain would be investigated. The strength of the gold-nanoplating technique would be optimally employed as this technique allows scanning larger areas and a lot of grains and grain boundaries in a reasonable time frame. Once a trend appears, local electrochemical techniques could be used to verify this phenomenon.

8.6.2 Study of the grain-specific parameters

The macroscopic electrochemical behavior of a polycrystalline metal is in principle the sum of the contributions of the different grains and grain boundaries, multiplied by their individual degree of coverage. Since some grain orientations are more electrochemically active than others, the ones with higher activity will act as anodic sites, while the less active ones will be considered cathodic. It is of crucial importance to determine to which extent the grain area affects the kinetics of the local electrochemical processes, also in relation to the surface area of the neighboring orientations. However, the information found in literature on the effect of the grain size on the overall electrochemical behavior is contradictory. Probably because the thermomechanical treatments that alter the grain size also affect other microstructural features like preferred grain orientation, i.e. crystallographic texture, and impurity segregation. A fundamental insight in how the grain size influences the local and overall electrochemical behavior would be a breakthrough in corrosion research.

To study the effect of grain size on the corrosion behavior it is important not to focus on individual grains, but on the mutual interaction between these grains and how the grain size can influence these interactions. As a first indication on how grain size influences electrochemical behavior, copper microstructures could be created with similar texture, but with markedly different grain sizes. In this way, the macro electrochemical behavior could be recorded. In a later stage, gold-nanoplating could be used to monitor the electrochemical activity of similarly oriented grains with different grain sizes in the same sample. All these macro- and mesoscale findings should need to be verified with carefully selected local electrochemical techniques.

8.6.3 Investigate the role of the grain boundary plane on the grain boundary electrochemical activity

Since corrosion is closely related to the presence of grain boundaries, a full characterization of the grain boundary geometry and its relation to the grain boundary activity is needed. The parameters involved in expressing grain boundary geometry are most easily visualized by considering the boundary crystallography in terms of degrees of freedom (DOF). Five DOF are required to specify the boundary, and these are most familiarly approached from the angle/axis of misorientation viewpoint (3 DOF) including the boundary plane (2 DOF). Little is known on the influence of the grain boundary plane on the corrosion behavior. It would be interesting to

find out, if in addition to the grain boundary misorientation, also the grain boundary inclination plays a role in the electrochemical behavior of the grain boundary.

To do this, at first gold-nanoplating experiments could be conducted to determine the electrochemical activity of different grain boundaries. Afterwards, the grain boundary plane of every grain boundary could be determined by a manual serial sectioning technique combined with orientation measurement in the scanning electron microscope, also called 3D EBSD. After determining the grain boundary plane of every boundary, it will be possible to link this information with the corresponding electrochemical activity, determined by both gold-nanoplating and local electrochemical techniques. This would allow a better understanding of the influence of the grain boundary plane on the electrochemical activity of a specific grain boundary.